

Studies of the performance of an IACT system for the TAIGA array

Dissertation

zur Erlangung des Doktorgrades
an der Fakultät für Mathematik, Informatik und
Naturwissenschaften
Fachbereich Physik
der Universität Hamburg

vorgelegt von

Diplom-Physikerin Maike Helena Kunnas
aus Lüneburg

Hamburg
2017

Gutachter der Dissertation Prof. Dr. Dieter Horns
Prof. Dr. Jamie Holder

Datum der Disputation 16. Februar 2018

Mitglieder der Prüfungskommission Prof. Dr. Caren Hagner
(Vorsitzende)
Prof. Dr. Dieter Horns
Prof. Dr. Erika Garutti
Prof. Dr. Günther Sigl
Prof. Dr. Thomas Bretz

Abstract

The gamma rays emitted by cosmic accelerators are the most important messenger for astrophysics at the highest energies, and the Cherenkov radiation from the cascades they cause in Earth's atmosphere is a reliable way to detect them. One of the newest experiments for such earth-bound observation is the TAIGA experiment.

This thesis investigates the performance of a possible air Cherenkov telescope system for the TAIGA experiment. The main principle of the TAIGA experiment is a combination between imaging air Cherenkov telescopes and Cherenkov shower front sampling stations. The point spread function of the intended telescope design has been determined with the Monte Carlo (MC) method and compared to a semi-analytic prediction. The mirror tiles to be installed into the prototype telescope at the TAIGA site have been characterized and an estimate of mirror alignment precision is given.

The effective area of a single telescope, as well as of a 3-by-3 telescope array, were calculated and a method to reconstruct the shower energy from the image size is presented.

In addition, the gamma hadron separation power of the telescopes in this setup via the "scaled image width" method has been determined using numerical simulations. It has been noticed that for core distances above 300 m the perceived image width stays constant. This effect is subsequently called the "Tur Tur" effect and been found to be a consequence of an increase of the average off-axis distance of the Cherenkov photon emission point for larger observation core distance. As an additional parameter, the possible influence of the earth's magnetic field on the image width has been studied.

The impact of the pixel size of the camera on the image width has been studied using Monte Carlo simulations and a method of time-saving simulations for larger pixels exploiting the results for smaller has been developed. It has to be noted, however, that this method has been deemed deficient as the rejection of incomplete pixels lead to partial rejection of the actual shower image, which in turn distorted the image width.

The influence of the pixel size on the gamma-hadron separation factor

and image width has been investigated using a semi-analytical 3D model of the shower which was originally developed for the HESS experiment. The study showed that the image width is almost independent of pixel size, while the quality factor favouring large pixels with a field of view larger than 0.5° per pixel. The limitations of the underlying 3D model have been examined, it has been shown that the model overestimates the image width at small (< 50 m) core distances and strongly underestimates it at distances larger than 150 m. Further investigation of this issue leads to the conclusion that this behaviour is due to the model not incorporating the Tur Tur effect.

Finally, the 3D model was used at a core distance of 100 m to show that, in principle, it should be possible to detect PeV showers with commercially available 50 mm CMOS cameras as the shower can produce a sufficient signal-to-noise ratio.

Zusammenfassung

Die Gammastrahlung, die von kosmischen Beschleunigern ausgesendet wird, ist der wichtigste Bote in der Astrophysik der höchsten Energien. Die Gamma-Photonen, aber auch der hadronische Hintergrund, verursachen Kaskaden, wenn sie auf die Atmosphäre der Erde treffen, und die Cherenkov-Strahlung, die in den Kaskaden entsteht, ist ein zuverlässiger Weg, diese ursprünglichen Teilchen zu detektieren. Eines der neuesten solcher Cherenkov-Experimente ist das TAIGA-Experiment.

In dieser Arbeit wird die Leistungsfähigkeit eines geplanten abbildenden Luftschauger-Cherenkov-Teleskopsystems als Teil des TAIGA-Experimentes untersucht. Das Hauptprinzip des TAIGA-Experimentes beruht auf der Kombination von abbildenden Luftschauger-Cherenkov-Teleskopen mit einem Array aus Stationen, die das Cherenkov-Schaugerfront-Zeitprofil aufzeichnen. Die Punktabbildungsfunktion des geplanten Teleskopdesigns wurde mit der Monte-Carlo-Methode bestimmt und mit einer semi-analytischen Vorhersage verglichen. Die Spiegelfacetten, die in den Prototypen auf dem TAIGA-Gelände eingebaut werden, wurden auf ihre Eigenschaften hin vermessen und eine Abschätzung der Spiegel-Ausrichtungs-Genauigkeit wird gegeben.

Die effektive Fläche sowohl eines Einzelteleskopes als auch eines drei-mal-drei Teleskop-Arrays wurden berechnet und eine Methode, die Schauerenergie aus der Gesamtamplitude des Schauerbildes zu rekonstruieren, wird präsentiert.

Außerdem wird die Fähigkeit des Teleskopes untersucht, mithilfe der Methode der skalierten Breite Gamma-induzierte Schauer vom Proton-induzierten Hintergrund zu unterscheiden. Hierbei wurde festgestellt, dass die gemessene Bildbreite bei Kernortabständen von über 300 m konstant bleibt. Dieser Effekt wird im Folgenden als "Tur Tur Effekt" bezeichnet und hat seinen Ursprung in einem Anstieg des durchschnittlichen Abstandes zwischen Schauerachse und Emissionspunkt der Cherenkovphotonen bei Erhöhung des Kernortabstandes.

Zusätzlich wurde auch noch die Abhängigkeit der Schauerbildbreite von der Ausrichtung zum Erdmagnetfeld untersucht.

Mit Hilfe der Monte-Carlo-Simulationen sollte der Einfluss der Pixelgröße auf die Bildbreite begutachtet werden. Hierzu wurde ein Zeit sparendes Verfahren entwickelt, das die Ergebnisse der feinpixeligen Simulationen aufsummiert, um Aussagen über große Pixel zu gewinnen. Allerdings wurde festgestellt, dass diese Methode mangelhaft ist, da die Verwerfung von unvollständigen Pixeln zu einer teilweisen Verwerfung des tatsächlichen Schauerbildes geführt hat, was wiederum die Bildbreite verzerrt hat.

Um dennoch den Einfluss der Pixelgröße auf Bildbreite und Gamma-Hadron-Separations-Faktor zu untersuchen, wurde ein semi-analytisches Modell verwendet, das ursprünglich zur Rekonstruktion von Schauerbildern des HESS-Experimentes entwickelt wurde. Die Studie zeigt, dass die Bildbreite nahezu unabhängig von der Pixelgröße ist und der Separationsfaktor bei Pixeldurchmessern von über 0.5° am besten ist. Die Grenzen des 3D-Modells wurden ebenfalls untersucht, es wurde gezeigt, dass das Modell bei kleinen Kernortabständen (< 50 m) die Bildbreite überschätzt, während bei größeren Kernortabständen (> 150 m) die Bildbreite drastisch unterschätzt wird. Diese Unterschätzung ist auf das Fehlen einer Modellierung des Tur-Tur-Effektes zurückzuführen.

Schlussendlich wurde das 3D-Modell mit einem Kernortabstand von 100 m dafür verwendet, zu zeigen, dass es prinzipiell möglich ist, mit einer handelsüblichen CMOS Kamera Luftschauer im Energiebereich der PeV nachzuweisen. Die Schauer sind hell genug, um ein hinreichend großes Signal-zu-Rausch-Verhältnis zu erzeugen.

Dedication

For all the people who believed in me whenever I couldn't.

Contents

1	Introduction	1
2	Gamma ray astronomy	5
2.1	Introduction	5
2.2	Current understanding of Ultra-High energy (UHE) astrophysics	6
2.2.1	The cosmic ray spectrum	6
2.2.2	Gamma Ray Radiation mechanisms	8
2.2.3	Pevatrons	9
2.3	Detection of cosmic gamma rays	9
3	The TAIGA project	15
3.1	HiSCORE Timing array	15
3.2	TAIGA IACTs	19
3.2.1	The telescopes	19
3.3	Air shower and detector simulation for TAIGA	22
4	Simulations for TAIGA	25
4.1	Hybrid technique	25
4.2	Methods and Results	27
4.2.1	About telescope design	27
4.2.2	Energy reconstruction	43
4.2.3	Combination	48
4.3	Optimisation of pixel size 1	67
5	Semi-analytical study	75
5.1	The model	75
5.2	General behaviour of image width and quality factor	80
5.3	Large core distances: The limitations of the 3D model	84
5.4	CMOS Cherenkov detection	87

CONTENTS

6 Conclusion and Outlook	89
6.1 MC simulation	89
6.2 Analytical Study	91
A Measured mirror parameters	93

Chapter 1

Introduction

”Wenn einer von Ihnen jetzt aufstünde und wegginge, würde er doch immer kleiner und kleiner werden, bis er am Horizont schließlich nur noch wie ein Punkt aussähe. Wenn er dann wieder zurück käme, würde er langsam immer größer werden, bis er zuletzt in seiner wirklichen Größe vor uns stünde. Sie werden aber zugeben, daß der Betreffende dabei in Wirklichkeit immer gleich groß bleibt. Es scheint nur so, als ob er erst immer kleiner und dann wieder größer würde [...] bei mir ist das einfach umgekehrt.”

- Tur Tur der Scheinriese, *Jim Knopf und Lukas der Lokomotivführer* [1]

“If one of you were to get up and leave, he would become smaller and smaller, until at last he would look like a point at the horizon. If he then came back, he would slowly become larger, until he finally stood in front of us in his true size. But you will admit that in reality, the person in question always stays the same size. It just seems, as if he became smaller and then larger again [...] for me, it’s simply reversed.”

- Tur Tur the illusory giant, *Jim Button and Luke the Engine Driver* [1],
translation by the author of this paper

As things get farther away, they seem to become smaller. Any person who knows a bit about geometry understands that it is not the actual item itself, but rather the viewing angle that shrinks - making sun and moon look the same size when viewed from Earth, and vast objects like other star systems,

supernova remnants and even other galaxies only seem to be tiny points in the sky; it is all a matter of distance.

And any astronomer knows that these tiny dots in the sky are well worth investigating, as they provide us with insight about the inner workings of our universe. While our own sun helped us realise that Earth is indeed round, the death of faraway stars allowed us to find the origin of all atoms heavier than iron, and the ripples in spacetime caused by black holes orbiting each other before merging improved our understanding of gravity.

But for all these insights, observation is always the first step, and someone who wants to observe always needs the right tools for the job. The first astronomers started their observation in the visible spectrum, by eye or with simple optical telescopes, but in recent times, many more messengers have been found to arrive from space. Today, not only visible photons, but the complete electromagnetic spectrum from radio to the highest energy gamma rays is available for observation, as well as atom cores and all elementary particles that can reach the earthbound observer. The most important messenger for this thesis is the gamma radiation, as charged particles are deflected by cosmic magnetic fields and therefore lose their direction information along the way. Gamma photons are not subject to this effect.

Earth's atmosphere however intercepts everything except neutrinos and the visible spectrum of light, so to observe the other particles and other bands of electromagnetic radiation, one has to move his detector into space. But not only the nature, but also the energy of the messenger determines which tool is ideal for observation. The energy spectrum of photons and particles arriving on Earth drops steeply over many decades of energy, so while photons of a few hundred GeV can be detected very well with satellite-bound experiments, the detection area a satellite can provide can never be enough to detect TeV photons with a sufficient rate as it can not compensate for the loss of flux, even if the detector was perfect.

Thus, to observe the highest energies the sky has to offer, the astronomer finds himself back on the ground for a sufficiently large experiment. Luckily, the atmosphere does not just absorb the photons and particles of high energy, but instead the photons and particles cause cascades of secondary particles in the atmosphere, the so-called Extensive Air Showers (EAS). In these showers, Bremsstrahlung and pair production alternate, increasing the number of secondary particles in the shower exponentially and distributing the primary energy among them until the mean particle energy becomes smaller than the critical energy. At this point, the mean energy loss by absorption becomes larger than the energy loss by pair production, and the number of particles in the shower decreases. If the primary particle is a hadron, the showers exhibit a larger transversal momentum as a result of the hadronic interactions

with the core fields of the atmosphere. The resulting shower becomes wider and more irregular as the hadronic interactions produce pions, which, when they decay, cause electromagnetic sub-cascades. All along the cascade, the particles emit Cherenkov light, as their velocity is larger than the speed of light in air. Also, the shower particles are deflected by the magnetic field of Earth, emitting synchrotron radiation in the radio band.

The many processes in a shower make it possible to detect them in several ways. The instrument chosen for this thesis the combination of imaging air Cherenkov telescopes (IACTs) with the non-imaging Cherenkov light-front sampling timing array called HiSCORE in the scope of the Tunka Advanced Instrument for Gamma-ray and Cosmic ray Astrophysics (TAIGA) project. Timing arrays are very good in directional reconstruction of a shower and are cost-efficient to build over large areas, but a discrimination between gamma-induced and proton-induced showers is difficult. IACTs on the other hand are very good at gamma-hadron separation as they take an image of the shower, but to properly reconstruct the incidence direction, the showers need to be detected by at least two telescopes. This limits the telescope spacing to about 300 m (most IACT systems operate at half this distance) and therefore makes it costly to cover large areas in telescopes. The TAIGA approach of combining a timing array with IACTs intends to reconstruct the incidence direction from the timing array while obtaining the separation parameters from the IACTs, removing the need for IACT stereoscopy and drastically increasing the amount of area that can be covered with a fixed number of telescopes. A more thorough description of this concept and the individual design specifications of its members are found in Chapter 3.

To study the performance of the intended telescope design, Monte Carlo simulations of the telescope have been performed (Chapter 4). The design was analysed concerning optical properties like point spread function (PSF) and effective area (Section 4.2.1), energy reconstruction from size (Section 4.2.2) and the gamma-hadron-separation power of a combined system (Section 4.2.3). Special attention is drawn to showers observed at large core distances, as it was noticed that the Cherenkov image of a shower indeed does not shrink with increasing distance, but rather stays constant. Therefore, the emitting region - the observed item, so to speak - becomes larger the farther the observer is away. This effect has been named the Tur Tur effect, after the illusory giant from the initial quote above.

Also, a first attempt to find a time-efficient possibility to study the impact of pixel size on the measured image width has been made in Section 4.3. A small-pixel camera has been simulated and adjacent pixels were summed up to emulate the effect of larger pixels, but the method used has been deemed inadequate since the rejection of incomplete pixels quickly lead to a partial

rejection of the shower image itself, which in turn distorted the image width.

As an alternative approach to Monte Carlo simulation, a semi-analytical approach was used to model the Cherenkov light output of an air shower (Chapter 5). The model, originally used to reconstruct images taken with the HESS IACT array, is described in Section 5.1 and was used to determine the change of the perceived image width and the gamma-hadron separation quality with pixel size (Section 5.2). The limitations of this model are described in Section 5.3, as the Tur Tur effect is not included in the assumptions of the model. Lastly, in Section 5.4 the model is used to show that, in principle, an off-the-shelf CMOS camera could be able to actually detect a shower of sufficient energy.

Chapter 2

Gamma ray astronomy

2.1 Introduction

For a long time, mankind's observation of space was restricted to the visible optical spectrum, by photons of only a very few eV. Messengers of higher energy were discovered only as late as 1912, in the balloon experiments of Victor Hess [2]. Hess sent manned balloons up to 5 km altitude to measure the ionisation of the atmosphere by observing the discharge rate of electrometers. The ionisation, after reaching a local minimum, started to rise strongly with altitude to a level that could not be explained by Earth's natural radioactivity. Hess proved that the source of the ionisation must come from space, the radiation was later given the name "cosmic rays" (CR) by Robert Andrews Millikan in 1925 [3].

Until the development of powerful particle accelerators in the 1950s, the cosmic radiation was the primary source of insight for particle physicists. Balloon-borne experiments brought the discovery of several new particles including the positron, confirming Dirac's prediction of the electron's antiparticle [4], even though the CR flux is extremely low compared to the output of an accelerator, especially towards higher energies.

In 1939, Pierre Auger discovered that high-energy cosmic rays cause showers of charged particles in the atmosphere [5], so called extensive air showers (EAS). His first systematic studies already showed that the extraterrestrial particles could have energies in the PeV range, an energy that no man-made particle accelerator can reach yet, but these particles are so rare that less than 100 have been detected at an energy above 10^{20} eV.

Today, there are many different experiments observing the universe over almost 20 orders of magnitude in energy, with both charged particles and photons as messengers. This large span of energy necessitates many different

observation techniques.

2.2 Current understanding of Ultra-High energy (UHE) astrophysics

2.2.1 The cosmic ray spectrum

The cosmic ray energy spectrum from 10 GeV onwards is shown in figure 2.1. The flux follows a power law $\Phi \propto E^\gamma$ with a spectral index γ of about -2.7 until the spectrum reaches its first feature at approximately 4 PeV, the so-called *first knee*, where the spectrum steepens to $\gamma \approx -3$.

The origin of these cosmic rays is generally believed to be galactic up to the knee. Enrico Fermi first proposed that extreme events like supernovae accelerate charged particles in their shock fronts [7]. The extreme magnetic field of the supernova traps the particle so that it drifts in and out of the shock front, gaining energy from the electric field with every turn. With each cycle the particle has a chance to escape from the shock front, so while the energy increases with each cycle, fewer and fewer particles reach this number of cycles, and the energy spectrum drops.

Beyond the knee energies, it is widely assumed that a transition between galactic and extragalactic CR component takes place, though the exact mechanisms are unclear. An overview and discussion of the different scenarios can be found in [8].

At around 10^{18} eV, the cosmic ray spectrum flattens out again to its former spectral index of -2.7. This flattening is called the *ankle* and is presumed to be the transition of dominance between the galactic and the extragalactic particle flux component [9, 10]. This is where the Ultra-High Energy (UHE) regime begins.

The upper end of the all-particle spectrum lies at about 10^{20} eV. An explanation of this upper limit of possible energy, the so-called *GZK-cutoff*, is named after Greisen [11], Zatsepin and Kuz'min [12], who published papers with the same theory simultaneously but independently. Protons of an energy of more than $5 \cdot 10^{19}$ eV carry enough energy to react with the cosmic microwave background (CMB) to create pions. Due to the ubiquitousness and homogeneousness of the CMB, this restricts the maximum travel distance of a proton to approximately 50 Mpc. Any proton with an energy higher than $5 \cdot 10^{19}$ eV must thus have originated closer than this distance from the viewer.

Any heavier CR components of this energy may have a smaller cross section for photopion production with the CMB, but they get destroyed by

2.2. CURRENT UNDERSTANDING OF ULTRA-HIGH ENERGY (UHE) ASTROPHYSICS

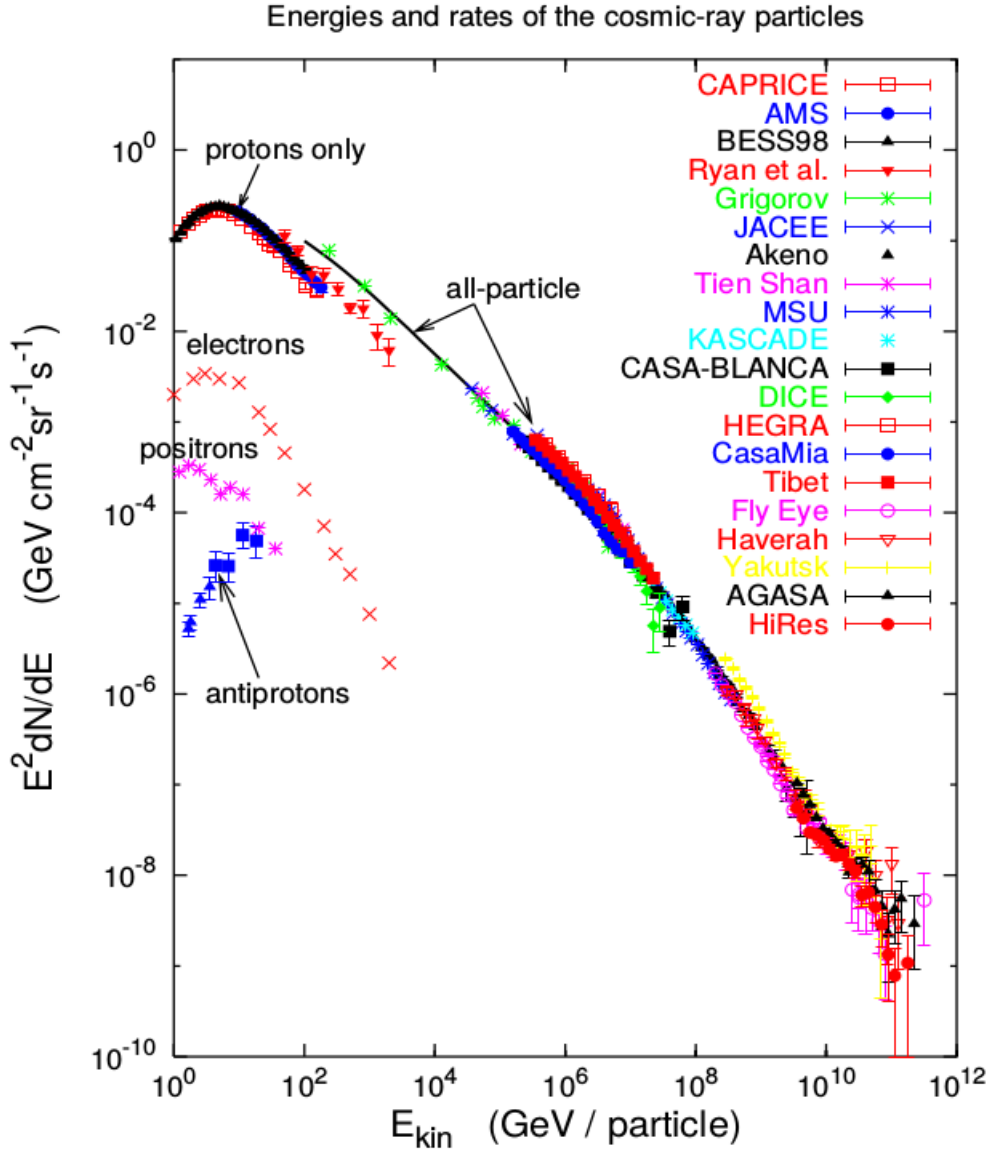


Figure 2.1: All-particle differential spectrum of the cosmic rays. The spectrum follows a power law with a spectral index of -2.7 up to the knee at 10^6 GeV, where it steepens to $\gamma = -3$, with a further steepening to -3.1 at the second knee at 10^8 GeV. It flattens back out to $\gamma = -2.7$ at the ankle before reaching a cutoff at 10^{11} GeV. Figure taken from [6].

2.2. CURRENT UNDERSTANDING OF ULTRA-HIGH ENERGY (UHE) ASTROPHYSICS

spallation with other CR particles or photodisintegration from ambient light, where the CR cores are excited by the light and then decay. These processes yield a mean free path smaller than 30 Mpc, and thus the heavier components do not contribute to the flux at cutoff energy.

2.2.2 Gamma Ray Radiation mechanisms

The gamma rays produced in sources like supernovae, binaries, pulsars and AGN are far too energetic to be a result of black body radiation. There are several non-thermal mechanisms from which the gamma rays originate:

If a particle is slowed down by the Coulomb field of a core, it emits *Bremsstrahlung*. The photons emitted are mostly of smaller energy, as the cross section is roughly inverse to the energy of the photon emitted.

A particle being deflected in a magnetic field, for example that of a pulsar, emits *synchrotron radiation*. The synchrotron radiation is highly polarised and an indicator of strong magnetic fields, which is why this fact is especially interesting for observing extended sources like the inner structure of pulsar wind nebulae.

Another source of UHE gamma rays is *inverse Compton scattering* (ICS). A relativistic electron scatters on an ambient photon (for example from the CMB), transferring energy to the photon in the process. This process is especially effective in conjunction with strong magnetic fields; an electron moving through the magnetic field of a source emits synchrotron radiation, which inverse Compton scatters on the very same electron population and thus gains more energy [13]. The source's spectrum accordingly shows two peaks, one of the original synchrotron photons, and the other of the photons that experienced inverse Compton scattering [14].

The inverse Compton process however possesses an energy limit, the so-called Klein-Nishina regime, where the interaction cross section between lepton and photon drops steeply at a photon energy of about 100 TeV.

The last relevant channel of photon production is the *neutral pion decay*. Hadronic collisions produce uncharged pions, which decay into two gamma photons with a typical resulting energy of about 1/10th of the energy of the primary proton [15]. For protons of sufficient energy this may result in TeV photons. The pion decay channel is of special interest because it is the only way of obtaining information of the spatial and energetic makeup of the proton emission of a source, as protons get deflected along their way to Earth.

2.2.3 Pevatrons

So far, all gamma ray astronomy has taken place up to a few tens of TeV. The production mechanism of these TeV photons is ambiguous, however, as both the inverse Compton process as well as the pion decay can produce gamma photons of this energy. The identification of the origin of the TeV photons is therefore challenging.

For energies above 100 TeV on the other hand, the inverse Compton process is suppressed. Any gamma photons detected at this energy and beyond would therefore definitely be of hadronic origin, which in turn serves as a direct evidence of the existence of a special kind of source, the so-called Pevatrons [16]. Pevatrons are thought to accelerate particles up to PeV energies, and since the photons resulting from pion decay carry about one tenth of the energy of the original proton, gamma photons of more than 100 TeV are direct evidence of protons with PeV energy, and would therefore prove that PeV accelerators exist in our galaxy.

While some candidates have theoretically been proposed [16], no Pevatrons have been detected yet, but the experiment described in this thesis aims to prove whether or not they exist.

2.3 Detection of cosmic gamma rays

Cosmic accelerators produce particles and light over broad bands of energy. However, all charged particles are deflected by interstellar magnetic fields, resulting in an isotropic charged particle flux on Earth. The direction of origin of a charged particle is impossible to determine from the incidence direction on a detector. The charged particles and their composition only contain vague information on possible acceleration processes, as their energy spectrum can still be measured, but it is impossible to attribute a certain spectrum to a specific source.

Neutral particles like neutrinos can be observed, but their low interaction rate makes them laborious to detect with sufficient significance.

Photons are the messengers that contain the most information about a source. Because they are not deflected by anything except gravitational lensing, their incidence direction points back directly to their source of origin for all wavelengths from radio to hard gamma radiation. The gamma rays in the Ultra High Energy (UHE) regime ($E > 10^{18}$ TeV) are of special interest for the search of cosmic accelerators due to their high energy. However, Earth's atmosphere is opaque to gamma rays. This only leaves two choices: Either move the detector to space to observe the gamma rays directly, or use the

2.3. DETECTION OF COSMIC GAMMA RAYS

effects caused by the gammas in the atmosphere for indirect measurements.

Up to about 200 GeV, the cosmic rays can be measured directly through satellite-borne detectors like, for example, the Fermi LAT satellite [17]. The flux of particles is high enough in this energy range to achieve sufficiently high rates for sensitive observation. However, the energy spectrum of cosmic gamma rays drops steeply, from one particle per second per cm^2 at 300 GeV down to one particle per year per km^2 at 30 EeV, losing 2.7 and more orders of magnitude in flux for every order of magnitude in energy. For observation at rising energies, the effective area of a detector needs to increase to compensate for the lower fluxes. The dimensions of the detectors need to scale with energy until they are too big to be carried by satellites, giving an upper limit to direct detection techniques in favour of ground-based experiments.

Luckily, our planet provides us with a huge natural calorimeter: Earth's atmosphere.

Extensive Air Showers (EAS)

UHE particles and gammas hitting the atmosphere interact with the core fields of air nuclei and cause extensive air showers. These air showers allow us to observe UHE particles, and can be described with several parameters as shown in figure 2.2:

The *shower energy* E_s is the kinetic energy of the primary initiating the shower.

Zenith angle θ and *azimuth angle* ϕ describe the shower's direction of arrival. The prolongation of the primary's movement direction before the first interaction is called the *shower axis*, the intersection point between shower axis and observation level is fittingly called the *core impact position* ($x_{\text{core}}, y_{\text{core}}$) and the distance between observer (here: telescopes) and the core position is the *core distance*.

The showers themselves are particle cascades caused by the initial interaction between the shower primary and the air nuclei. Two kinds of cascades can be found in air showers:

Electromagnetic cascade

The main bulk of interactions takes place in the electromagnetic (EM) cascade, shown in figure 2.3, left. Incoming gammas with $E_\gamma > 2m_e = 2 \cdot 511 \text{ keV}$ can produce electron-positron pairs (e^\pm) in the Coulomb field of surrounding air atom cores. For the initial energies, other electromagnetic effects like Compton scattering or photoelectric effect are suppressed due to the high photon energies.

2.3. DETECTION OF COSMIC GAMMA RAYS

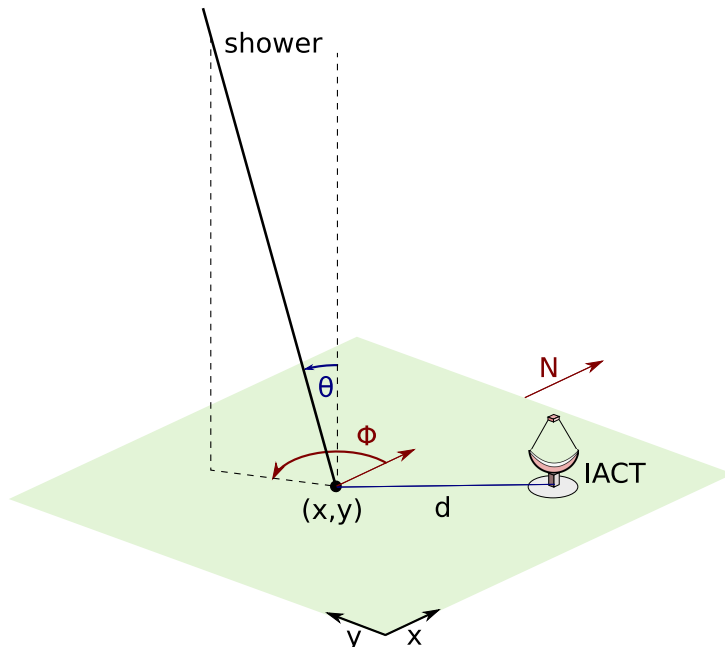


Figure 2.2: Overview over the shower parameters: impact position, core distance, θ , ϕ

The e^\pm produced (or a primary e^\pm) emit gamma photons as Bremsstrahlung when interacting with air core fields, losing about half of their energy over one radiation length. These gamma photons in turn produce another e^\pm in the next core field, and so on. The two processes alternate until the particle energy becomes so low that the ionisation loss exceeds the energy loss through Bremsstrahlung at the *critical energy*. For gaseous media of atomic number Z , the critical energy follows the relation

$$E_{\text{crit}} \approx \frac{710}{Z + 0.92} [\text{MeV}] \quad (2.1)$$

In air, the critical energy is about 84 MeV.

Up to the shower maximum, the shower contains about 2^n particles, with n being the number of traversed radiation lengths. The total number of particles at the shower maximum is proportional to the energy of the primary particle [18]:

$$N(E) = 2^{n_{\text{max}}} \propto \frac{E}{E_{\text{crit}}} \quad (2.2)$$

The *shower depth* X_{max} is the position of the shower maximum in the atmosphere. The typical unit is $[\text{g}/\text{cm}^2]$ and gives the thickness of the air

2.3. DETECTION OF COSMIC GAMMA RAYS

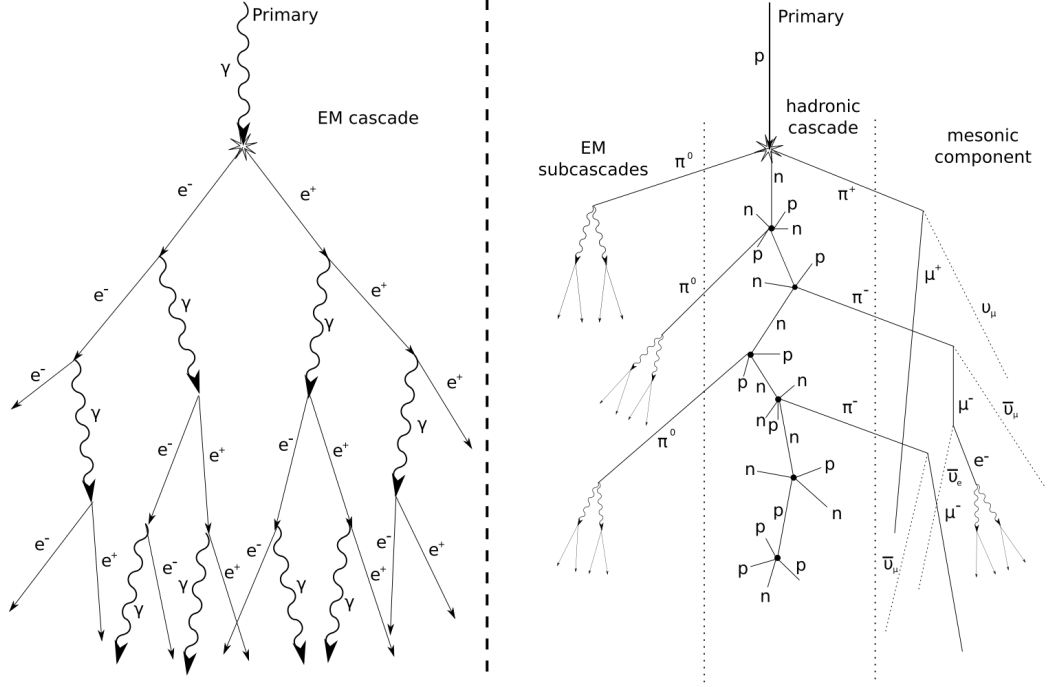


Figure 2.3: Overview over the development of air showers: a gamma shower (left) and a proton shower (right) with the respective contributing processes.

column that the shower needs to traverse to reach its maximum. The *shower height* h_{\max} is the corresponding distance between shower maximum and sea level and usually given in [m]. These observables are strongly dependent on the depth of the first interaction, which in turn depends on the primary energy [19]:

$$X_{max} = 335 + 27 \cdot \log_{10}(E) \quad (2.3)$$

After reaching the maximum, the cascade dies out since fewer and fewer e^{\pm} pairs are produced while ionisation, Compton scattering and photoelectric effect drain the energy from the cascade. In the end, the e^{\pm} are absorbed in the atmosphere with almost no particles reaching sea level for showers below 1 TeV primary energy.

Hadronic cascade

The first interaction of an incoming hadron or core is typically a strong interaction with an air nucleus. These collisions produce core fragments as well as pions and kaons, starting the hadronic cascade driven by further core collisions until the mean energy of the fragments falls below the critical

2.3. DETECTION OF COSMIC GAMMA RAYS

energy for multi pion production of approximately 1 GeV. The cascade is then followed by weak decays as seen in figure 2.3, right.

Charged pions decay into muons and anti muon neutrinos. The muons are the only particles that can be detected at ground level since they do not lose much energy to ionisation and due to their highly relativistic nature, not all of them decay into electrons and anti-neutrinos before reaching the ground.

Hadron-induced showers get an electromagnetic component from neutral pions decaying into gammas or muons reacting with the atmosphere, which in turn start electromagnetic sub-cascades. In this work, the term "hadronic shower" refers to the whole of the shower including both the hadronic cascade and the electromagnetic component, as long as the primary was a hadron.

In the hadronic interactions, the particles can pick up stronger transversal moments than in the electromagnetic cascade before starting electromagnetic subshowers. This leads to showers that are broader, but also more irregular and radially asymmetric relative to the shower axis.

Cherenkov light

The relativistic particles of an air shower have enough energy to be moving faster than light speed in the surrounding air, $v_0 > v > c_0/n_{\text{air}}$, with n_{air} being the refractive index of air. Under the condition of

$$E_{\text{min}} = \frac{mc^2}{\sqrt{1 - n^{-2}}} \quad (2.4)$$

the particles emit Cherenkov light [20] in a cone behind them. Analogous to a Mach pressure cone in supersonic movement, the opening angle θ_{cher} of the Cherenkov light cone is

$$\cos(\theta_{\text{cher}}) = \frac{1}{n \cdot \beta} \quad (2.5)$$

with β being the ratio between the velocity of the electron and the speed of light in vacuum. While the amount of light emitted only depends on the energy of the particle, but not the local density, the emission angle changes with emission height as the refractive index is dependent on the pressure in the medium. As the pressure rises with falling altitude, the Cherenkov angle increases. This change in Cherenkov angle causes a focusing effect that manifests itself in an increased brightness at approximately 120 m distance from the shower impact position, where the Cherenkov cones of the particles close to the shower axis of all altitudes overlap [21].

2.3. DETECTION OF COSMIC GAMMA RAYS

The Cherenkov light is emitted due to polarisation of the surrounding medium becoming constructively interferent. The spectrum emitted is proportional to $1/\lambda^2$, but as ozone absorbs UV light, the peak of the spectrum arriving at ground level lies at the visible blue wavelengths of about 340 nm [22]. The different light cones from the particles in the shower add up to become a continuous light front of about 1 m thickness (about 3 ns duration on the ground) and about 300 m diameter at sea level, with the proportionality between primary energy and total amount of emitted light allowing to use the atmosphere as a calorimeter.

Detection methods

EAS can be detected by several channels due to the multitude of interactions happening in the shower:

The non-muon charged particles in a shower can only be measured directly if the detector is high enough in the atmosphere. One example for such an experiment is HAWK [23], which consists of water tank arrays in which the particles produce Cherenkov light by which they are detected.

The muons that are produced in the pion decay of hadronic showers can be recorded by surface-based detectors even at sea level, for example with the scintillation counter array KASKADE-Grande [24].

The charged particles of the electromagnetic (sub-)cascade emit synchrotron radiation in the Earth's magnetic field. The frequency of the emitted radiation lies in the radio band and can be picked up by radio antennae (e.g. Tunka-REX [25]) if the shower energy is high enough ($E > 10$ PeV).

While the electromagnetic cascade components are fully absorbed in the atmosphere below a certain altitude, they excite the air molecules to emit UV fluorescence light which can be picked up by mirror telescopes (e.g. Auger fluorescence telescopes [26]).

The final EAS component in this list and the most important one for this work is the Cherenkov light emitted by the particles as described above. The two most common approaches to detect it are shower light front sampling timing arrays (e.g. AEROBICC [27], Tunka [28], HiSCORE [29]), and the imaging telescopes (e.g. HEGRA [30], HESS [31]). This work will focus only on the Cherenkov light and these two experimental approaches, which are described in detail in the following sections.

Chapter 3

The TAIGA project

The TAIGA project aims to observe the gamma ray spectrum from 50 TeV to several PeV of energy. Its speciality is the combination of multiple approaches to UHE gamma ray observation into one array with every technique complementing the others. TAIGA is being built at Tunka valley, Russia (51° 48' 35" N, 103° 04' 02" E, 675 m a.s.l.) at the site of the Tunka-133 [32] experiment.

The core component of the TAIGA experiment is the Cherenkov-sampling HiSCORE [29] timing array. Core distance and impact direction will be measured by it.

The timing array will be complemented by imaging telescopes [32] taking lateral images of the Cherenkov light. Imaging telescopes are especially suited for determination of a shower's primary particle.

Another participant are muon detectors as another way to discriminate primaries consisting of reused KASCADE-Grande [24] parts. Also at the site is the Tunka-REX [25] radio detection array, which is not part of TAIGA yet, but currently uses the HiSCORE stations as trigger. These two methods are not the topic of this thesis, however, and will not be discussed in further detail.

3.1 HiSCORE Timing array

Timing arrays like HiSCORE (High Surface Cosmic ORigin Explorer, formerly Hundred *i Square-km Cosmic Origin Explorer, [33]) are large-area wide-angle instruments that sample the lateral Cherenkov photon distribution, the so-called *light density function* (LDF) of an EAS by recording both amplitude and timing data. HiSCORE stations each consist of four 8 inch photomultiplier tubes (PMTs) looking into the sky through Winston cone

3.1. HISCORE TIMING ARRAY

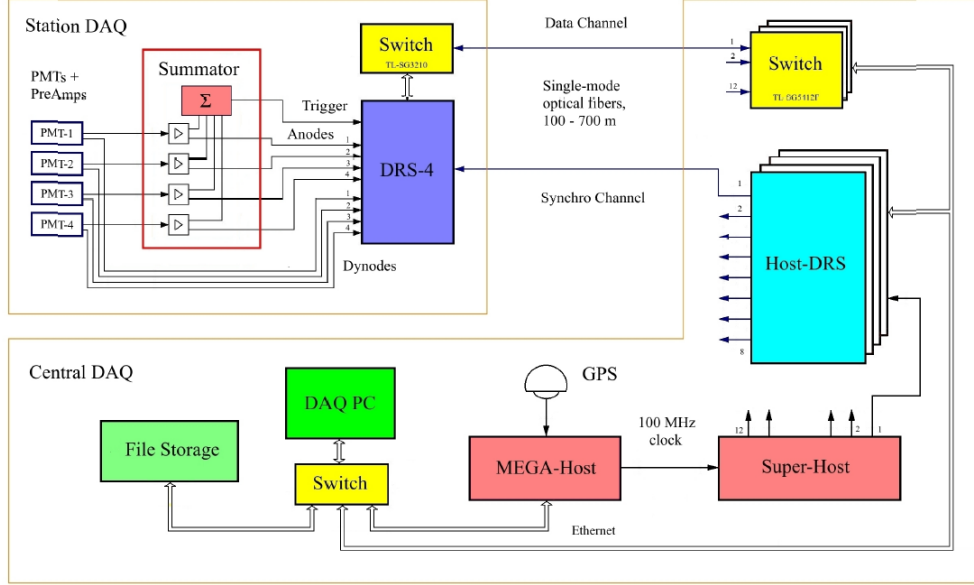


Figure 3.1: Data processing of the HiSCORE array. Inside a HiSCORE detector station, the PMT signals are split, one signal flow is processed by a custom-built DRS4 chipset [34], while the other signal flow feeds the trigger, which in turn enables the readout. The inter-station time synchronisation is provided by a dedicated channel from the central DAQ unit via optical fibre. If a trigger signal is given, the sampled data is sent by optical cable to the central DAQ, transferred to the DAQ PC and subsequently stored on a hard drive. Image taken from [35].

light collectors, resulting in a sensitive area of about 0.5 m^2 per station. By 2017, 58 stations have so far been erected, covering about 0.6 km^2 .

In each of the HiSCORE detector stations, the four PMT anode signals are split and analogously processed in two ways as shown in figure 3.1. The first set of PMT signals are sampled with 2 Gs/s inside the individual station using a custom-built DRS4 [34] chip based system, with a timing signal provided from the central data acquisition (DAQ) setup by optical fibre. This setup provides a 0.2 ns time synchronisation accuracy. Timestamp and analog amplitudes are sent to the central DAQ by optical fibre once the trigger signal is given, then transferred internally to the central DAQ PC and subsequently stored on hard drives. For further details, please refer to [35].

The readout cue is provided by the second set of anode signals. The four PMT anode signals are summed up and compared to a trigger threshold which, if exceeded, allows the trigger signal to be expressed. The design of the analog summator board, including the option of clipping the trigger

PMT signals before summation for better noise rejection, were developed in the framework of the diploma thesis of M. Kunnas [36], please refer there for a more thorough description.

The HiSCORE stations sample the LDF in the shower front at their respective positions. All particles in the shower emit Cherenkov light and most of the photons that were emitted in the optical spectrum reach ground level regardless whether the emitting particle has been absorbed in the atmosphere or not. So while particle detectors only see the latest step in shower development, the Cherenkov light contains information about all phases of the shower development.

The reconstruction algorithms of the HiSCORE array were developed in the framework of the PhD thesis of D. Hampf [37]. The parameters used for this geometric reconstruction are arrival time, signal intensity and signal width. As a first step, a preliminary *core position* is derived as the center of gravity of the station signal intensities. For small showers, the accuracy of this method is good enough, but if enough data is available (>4 stations triggered), a fit to the shower's LDF is performed later on to improve the result.

The arrival delay between the different stations enables the observer to calculate the shower direction as illustrated in figure 3.2. To receive a preliminary direction, we assume the Cherenkov light front of the shower to be a plane, and the time-of-flight differences follow this distribution [37]:

$$t(x, y) = \frac{\tan(\theta)\cos(\phi)x - \tan(\theta)\sin(\phi)y}{c_{\text{air}}} + t_0 \quad (3.1)$$

The *shower direction* (θ, ϕ) can be determined by a fit to the distribution. These values are accepted for small showers, but for showers with a multiplicity of > 4 triggered stations, the reconstruction can be further refined by considering the curvature of the light front. For details on the calculations, please refer to [37] or [38].

The shower *energy* can be reconstructed reliably from the station amplitudes at a distance of about 200 m from the shower core. At this distance, the LDF is primarily and linearly dependent on the shower energy, with some influences of the nature of the shower's primary. Hadronic showers contain less Cherenkov light than EM showers due to the smaller number of electrons in the cascade. This leads to a systematic underestimation of particle energy in hadronic showers, which is uncritical as hadron showers are considered background.

The *nature of the primary* is especially important to know since source

3.1. HISCORE TIMING ARRAY

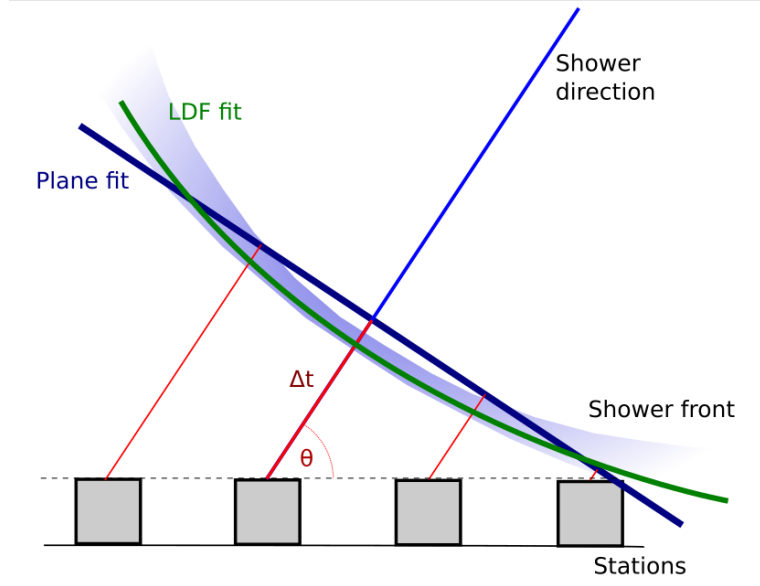


Figure 3.2: Principle of direction reconstruction from the shower front arrival times. The arrival delay between the stations is used to determine the angle of incidence.

regions and sources emit gammas against the mostly hadronic background. However, it is complicated to determine the primary with ground-based experiments in general and timing arrays in particular due to the large event-to-event fluctuations in the shower development. Hadronic showers show a longer development below the shower maximum due to the higher fraction of hadrons as well as a larger spread in transversal momentum of the secondary particles. These features, however, are hard to measure due to the shortness of the flashes and are partly lost in event-to-event fluctuations.

HiSCORE makes use of the difference in longitudinal shower development. Since the shower particles travel through the medium faster than light does, the Cherenkov photons arrive in time-reversed order. The first photons to arrive are the ones last emitted. Thus, the signal rise time shows the development of the shower after its maximum, and a longer rise time hints at a hadronic shower as hadronic showers die out slower than their EM counterparts. The difference between hadronic and EM showers is small however (2.5 ns for hadronic vs. ~ 2 ns EM for $E > 100$ TeV) and is only sufficiently expressed at the very center of the shower and at a sufficient energy. Studies in [37] show that below 100 TeV, no efficient separation can be achieved with the HiSCORE array.

In order to improve the gamma-hadron separation at low energies, a combination of the HiSCORE array with the well-established imaging air Cherenkov telescope technique (IACT) was chosen, as the IACT technique is especially powerful with regards of gamma-hadron separation.

3.2 TAIGA IACTs

Imaging air Cherenkov telescopes (IACTs) are the method of choice concerning gamma hadron separation at lower energies. Experiments like HEGRA [30] and H.E.S.S. [31] operate IACTs very successfully for observation, but for a highly accurate reconstruction of shower direction and core impact position, more than one image of a shower is needed.

The drawback of stereoscopy lies in the telescope spacing: In order to take more than one image of a shower, more than one telescope must be inside the Cherenkov light pool of the shower. On sea level, the diameter of this light pool is about 300 m, which determines directly the upper limit to the distance between the IACTs. The high number of channels in an IACT camera in combination to the limited spacing make for relatively high instrumentation cost per km², so while stereoscopy may be the observation method of choice for high to very high energy (100 GeV-5 TeV), it is not favourable to cover the large areas needed for UHE observation.

To profit from the IACT's separation power while keeping the costs of the array down, TAIGA will add small IACTs with large inter-telescope spacing to the HiSCORE array. The HiSCORE array will provide core position and shower direction, removing the need for IACT stereoscopy, while the IACTs will provide the gamma hadron separation.

The details of this combination will be discussed more thoroughly later in this work. The first IACT was deployed in 2015/2016 and was in commissioning during the last observational season. A second IACT is currently (end of 2017) under construction.

3.2.1 The telescopes

The goal of the IACT design was to build a telescope that can observe showers of 20 TeV (HiSCORE's energy threshold) and above, with as little channels per km² as possible while keeping the resolution needed to properly reconstruct the primary of a shower. Since the EAS Cherenkov light at these energies is so bright, the resulting telescopes are *small*, with a *large field of view* (FoV) to keep up with HiSCORE's wide-field observations.

3.2. TAIGA IACTS

Overall focal length	4.95 m	Segment focal length	4.95 m
Mirror dish diameter	4.75 m	Mirror segment diameter	60 cm
Number of mirrors	34	Number of pixels in cam	547
Camera diameter	80 cm	Pixel diameter	3 cm
Camera FoV	10°	Pixel FoV	0.36°

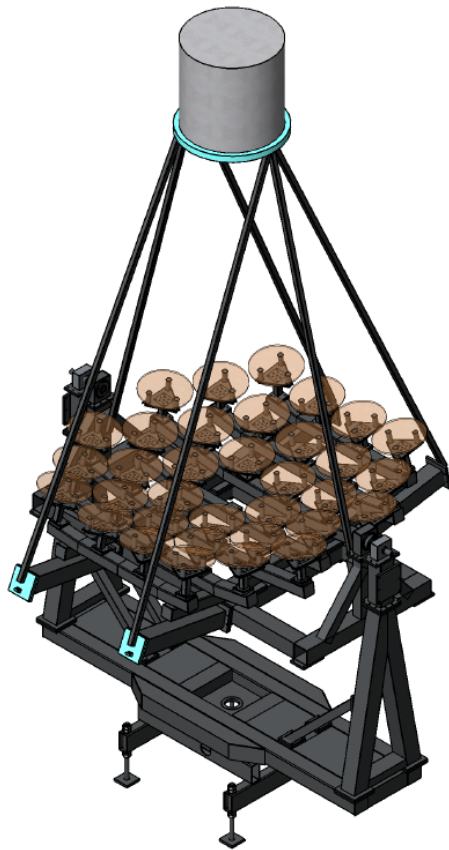
Table 3.1: Table of telescope parameters as used in the simulation.

For the TAIGA telescopes, the Davies-Cotton design [39] was chosen as it is the go-to setup for imaging telescopes. On a Davies-Cotton telescope, spherical mirrors are mounted on a main dish frame with half the radius of curvature of the tiles, which provides a good balance between imaging quality and production cost. The construction concept of the TAIGA IACTs can be viewed in figure 3.3a. The individual mirror tiles are mounted on triangular holding plates with one ball joint and two servo motors for alignment.

The camera as seen in figure 3.4 consists of 560 PMT pixels with a diameter of 3 cm per pixel. Seven pixels are connected onto one trigger board, with four of these clusters combined into a trigger sector, as seen in figure 3.3b. While the PMT model for mass production and use in additional telescopes is not determined yet, the first three telescopes will be equipped with XP1911 PMTs [40] originally used in the ZEUS accelerator experiment [41].

As the simulations were begun a long time before the final design choices have been made, the camera layout used in the simulations was of a simpler nature, with 547 pixels arrayed into a large hexagon and the trigger clusters engrossing overlapping sectors of this hexagon.

A pixel diameter of 3 cm yields a camera diameter of 80 cm, which corresponds to a single pixel FoV of 0.38° per pixel and 10° FoV for the overall telescopes. While this is a large FoV for an IACT, it is limited compared to the 60° FoV of the HiSCORE array. Therefore, while whole sky observations are difficult with these IACTs, the sensitivity and discrimination will be improved in the overlapping fields of view compared to HiSCORE alone, especially for pointed observations.



(a) The telescope



(b) A pixel drawer

Figure 3.3: Left: CAD drawing of the final telescope design. Right: Photograph of a pixel drawer with their cluster supply plates and the readout board. Each supply controls seven PMTs, while the readout board supplies and reads out the pixels of four clusters. Images by courtesy of the TAIGA collaboration.

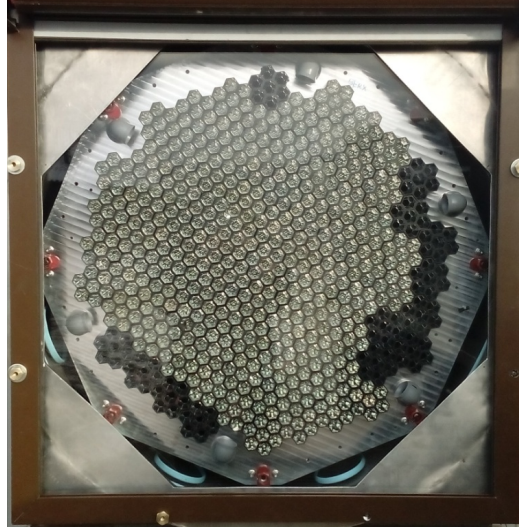


Figure 3.4: Photograph of the front view of the TAIGA IACT camera of the prototype telescope, from the construction phase. The pixel layout can be seen, with a few drawers missing as they were still under assembly. Image by courtesy of the TAIGA collaboration.

3.3 Air shower and detector simulation for TAIGA

To evaluate a telescope design and to later on properly interpret measured showers, one must conduct simulations to predict the expected results. Complex setups like IACTs are best explored by the *Monte Carlo* (MC) method, using computational algorithms and ray tracing to generate large amounts of numerical samples. Samples generated by MC observe all processes through the course of an experiment or phenomenon, with randomised decisions performed whenever necessary to determine the outcome of statistical processes like reflection, emission, absorption or decay. The data obtained reflects the actual behaviour of events and particles as closely as possible.

For TAIGA, the development of the particle cascade and the Cherenkov light were studied with the CORSIKA code, and the IACT results were generated with `sim_telarray`.

CORSIKA

The development of the particle cascade and the Cherenkov light were studied by an MC code package called CORSIKA [42] (version 6990), a powerful tool to simulate particle interactions widely used among accelerator, particle

and astroparticle collaborations. Originally developed for the KASKADE-Grande experiment, CORSIKA uses the newest knowledge about particle interactions to simulate a particle's propagation through the atmosphere. As particle physics develops and since the amount of different possible interactions is large, CORSIKA supports several modules for different models of high energy hadronic, low energy hadronic, and electromagnetic interactions. The models used for this thesis are QGSJET [43] and Gheisha [44] (high and low energy hadronic interactions) and the EGS4 model of electromagnetic interactions. Additionally, the IACT option for generation of Cherenkov light was used.

As typical for a MC simulation, CORSIKA follows each particle through the atmosphere while covering all interactions along the way. All secondaries are traced, as well as the Cherenkov light the secondaries emit. To keep the amount of data at a reasonable level, CORSIKA combines a user-set number of Cherenkov photons into photon bunches. Each bunch is subsequently processed as one photon with a weight equal to the number of photons in the bunch. Only those bunches are saved to the output file that pass through the detector, which is simplified to a sphere of user-specified radius and position.

To save computing time for high numbers of events, the individual showers can be scattered over the considered area multiple times without recalculation. This increases the total number of events with minimal addition to the computing time. For further options and more detailed descriptions, please refer to [42] and [45].

The CORSIKA output is given in the binary EVENTIO format and then further processed for the IACT response.

sim_telarray

IACTs are complex setups with many details contributing to the final camera image. To reflect this, the *sim_telarray* software package by Konrad Bernlöhner was used for this thesis.

sim_telarray is a raytracing MC software that includes telescope electronics and performs an image reconstruction. It reads in the binary CORSIKA output containing number, position and direction of the emitted Cherenkov photons. As the first calculation step, the influence of the atmospheric conditions is applied. While CORSIKA considers atmospheric composition in the particle cascade, Cherenkov photon emission probability and Cherenkov angle, no further absorption or scattering is applied to the photons. Also, no wavelength is defined by CORSIKA, which is subsequently introduced by *sim_telarray* to account for the wavelength-dependent scattering and absorption coefficients. *sim_telarray* comes with a set of atmospheric profiles usable

3.3. AIR SHOWER AND DETECTOR SIMULATION FOR TAIGA

for most known IACT experiments, for example the Namibian desert for the HESS experiment, but own atmospheric profiles can be used if available.

A raytracing routine then follows the photons' path through the mirror optics defined by the user. Here, not only the basic telescope geometry is regarded, but also deviations from the ideal setup like reflection probability, variation of mirror shape or inaccuracies in mirror alignment. These randomised deviations reflect the inaccuracies real parts would have due to production processes, assembly or use. The raytracing also enables the user to determine the *point spread function* (PSF) of a telescope design. Light concentrators in front of the camera pixels are also simulated via ray tracing.

After determining how many photons arrive on the PMT pixel including their distribution over time, an electronics response simulation is performed. The PMT conversion factors, electronic delays, baseline and baseline noise can be specified individually for every channel. The global settings include, but are not limited to, discriminator details like readout window length, trigger logics like trigger threshold, trigger multiplicity and trigger style (p.e. next neighbour trigger or drawer trigger), and NSB noise. The multitude of possible options allows to flexibly adjust a simulation to changes in the experimental setup. The electronics simulation generates a signal like one would measure in a real telescope, including the addition of noise generated by electronics and afterpulsing of the PMTs.

Following all MC processes, the signal is then processed like a real experimental signal. The analog signal is integrated into a total pixel amplitude. If a telescope is counted as triggered, a Hillas-type image analysis ([46], details in chapter 4.2.3) is performed. Also, the amplitudes of the pixels are stored in an EVENTIO output file for possible reprocessing.

At this step a time analysis of the MC data is possible as well, but is not performed for TAIGA because the intended design of the real telescope does not foresee taking time information for every camera pixel.

As the last step, all results can be expressed in ASCII format, the `sim_telarray-custom` hdata format and a file of camera images.

read_hess

`read_hess` is a software tool that comes with the `sim_telarray` package. It reads in the amplitude data saved from `sim_telarray` and redoes image cleaning, Hillas analysis and plotting. The purpose of `read_hess` is to allow changes in tailcut thresholds or other reconstruction steps without the need to repeat `sim_telarray`'s time-consuming MC raytracing.

Chapter 4

Simulations for TAIGA

This chapter presents the simulation studies conducted to evaluate the performance of the assumed TAIGA IACT design. An assessment of the telescopes' point spread function (PSF) is given. The effective area of a nine telescope array is presented, the dependencies needed to reconstruct the shower energy from the image size are determined and an estimate of the gamma-hadron separation quality is given.

4.1 Hybrid technique

TAIGA aims at gamma ray observation in the highest regions of the energy spectrum. The low fluxes of gamma rays require to maximise the effective area of any detector while retaining the possibility of discriminating between the essentially isotropic hadron background and the gamma ray signals of the sought after sources.

As mentioned in Chapter 3, no known detection method can so far sensibly provide for these aspects at the same time at energies beyond 10 TeV. Timing arrays can cover large areas, but lack in gamma hadron separation power near their energy threshold. Telescope systems, both fluorescence and Cherenkov, can provide a better distinction between the primaries, but they require a high number of hardware readout channels per km² and are thus costly to cover large areas with.

Combining different measurement methods to compensate for individual weaknesses of the methods is obvious. Some combination experiments already exist or are in commission, such as particle array + fluorescence telescopes (p.e. Pierre Auger Observatory [26]), muon + radio (KASKADE [48]), Cherenkov timing + radio (Tunka-133 [28] + TunkaREX [25]) or particle + muon + Cherenkov IACT (LHAASO [49], in commission).

4.1. HYBRID TECHNIQUE

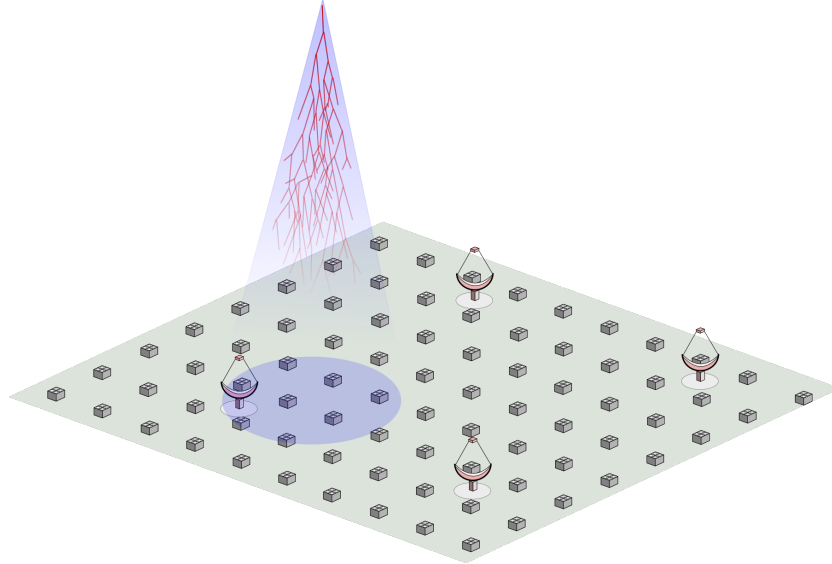


Figure 4.1: Concept of the combination between Cherenkov telescopes and Cherenkov sampling (not to scale). Showers most often hit both an IACT and a few HiSCORE stations, but never two IACTs at the same time, and rarely only HiSCORE stations but no IACT.

TAIGA’s hybrid technique will be the first to combine two approaches that use the same information: the air shower’s Cherenkov light. In a combination of the HiSCORE Cherenkov timing array and the TAIGA IACTs, HiSCORE’s weakness in the gamma hadron separation near the energy threshold will be more than compensated by the IACT’s image information, while keeping the number of channels per km² reasonably small.

The IACT images of TAIGA do not need a stereoscopic view of a shower to be reconstructed. The sampling of the shower light front, performed by HiSCORE, will yield a preliminary core position and incidence angle, which is then in turn used for analysis of the shower image, as illustrated by figure 4.1.

The parameter of discrimination between the different primaries will be the *Hybrid Scaled Width* (HSCW). Analogous to the scaled width in other IACT experiments, MC expectancy values of the IACT image width for different image sizes, zenith angles and core distances are written into a lookup table. The lookup table is then used to scale the experimentally measured widths to their expectancy value. Details about this method are found in Section 4.2.3.

The big difference to classic image scaling is the fact that the information used to pick the right lookup table entry is not calculated from the same image that is being scaled, but rather from the reconstruction of the shower

front sampling HiSCORE data.

Of course all the other information contained in the IACT images will not be ignored. The preliminary core position from HiSCORE helps resolving the directional ambiguity in the monoscopic camera image, the direction information received will then in turn be weighted into the final core position reconstruction. Also, while no single-pixel time stamps are taken for the telescope, the image size plus the time stamp of the telescope event practically double as a HiSCORE station data set. This might lower the energy threshold of the combined array since it lowers the amount of HiSCORE stations that need to have triggered for reconstruction. The theoretical limit might even be one station plus one telescope since one station is enough to cancel the ambiguity in the camera image.

Since a stereo view of the shower is not needed, the spacing between the telescopes can be increased. To fully cover an area, 600 m between telescopes is a feasible distance because only one telescope needs to be inside the EAS light pool. This reduces the amount of telescopes, and therefore channels, needed by the factor of four compared to an IACT-only system, with only 9 telescopes needed to cover an area of more than 1.2 km x 1.2 km. Compared to the CTA small size telescopes [50], for example, the reduction of channels lies at more than a factor of eight as the TAIGA telescopes also have less than half the amount of pixels per camera.

Whenever a 9 station array is mentioned in this thesis, a 3 x 3 square array with 1200 m edge length and 600 m between the individual telescopes is considered, at an observation level that corresponds to the Tunka-133 site.

4.2 Methods and Results

The following section contains the results of the `sim_telarray` studies about the point spread function of the IACTs, the effective area of single telescopes and the nine telescope array, energy reconstruction from image size and the gamma hadron separation power of a combined HiSCORE-IACT system.

4.2.1 About telescope design

One of the aspects that need to be evaluated before building a telescope are the imaging properties of the estimated design. It was known that the general idea of a 4 m IACT is a good EAS detector design since the HEGRA [30] experiment has used it to great success, but as details vary, proper MC studies need to be made to get details on the TAIGA IACT performance.

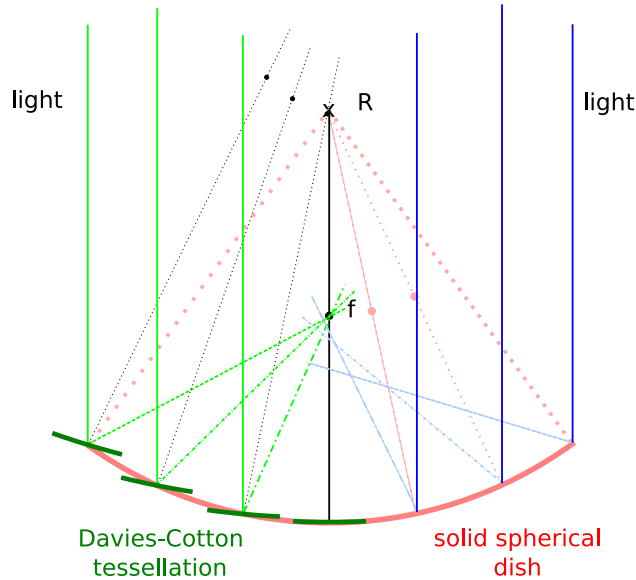


Figure 4.2: Comparison of ray paths after reflection on a solid spherical mirror (right) and on a Davies-Cotton tessellated mirror dish (left). D-C mirror tiles are tilted outwards so that the resulting images overlap in the focus.

Point Spread Function

The light coming from an air shower is weak compared to other natural light sources. This causes the need to use mirrors to collect enough light to make a shower detectable. The mirrors, however, have a blurring influence on the resulting image, given by two unerasable influences: their geometry and hardware inaccuracies. The measure of these influences is the angular size of the image of an infinitely far away point source, and is called the *Point Spread Function* (PSF).

Influence of geometry: The simplest approach to a light-collecting mirror is a concave spherical mirror of radius R as shown on the right half of figure 4.2. The focal point of a spherical mirror lies at half the radius of curvature. It can be seen that the focus of a spherical mirror is not perfect, rays coming in at large off-axis impact parameters are not reflected directly into the focal point, but rather cross the telescope axis between mirror and focus. This will cause any image to always be smeared out by the mirror.

A perfect focus is obtained by a hyperbolic mirror. In a hyperbolic reflector, all the paths of the light are equal in length so that the reflection angles match and all light passes through the focal point. However, a single hyperbolic mirror can not be built in the necessary size for an IACT, which

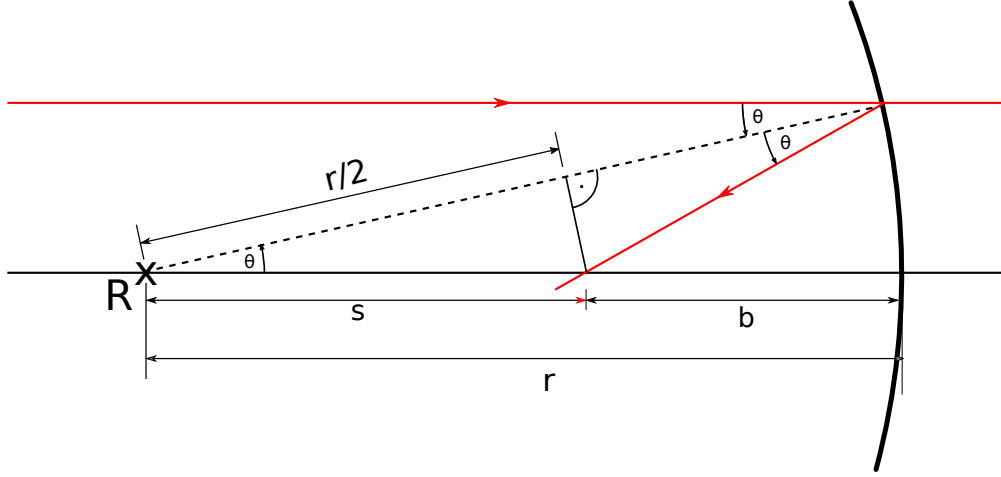


Figure 4.3: Ray diagram for a beam of light reflecting on a spherical mirror, with r as the radius of curvature of the mirror, b the image length, θ the incoming ray's off-axis angle. These labels are as used in equation 4.1.

is why the main mirror dishes of large telescopes are typically tessellated.

The Davies-Cotton design of the TAIGA IACTs' mirror dish foresees the mounting of spherical mirror tiles on a spherical frame with half the curvature radius of the tiles and can be seen in figure 4.2, left half. The perfectness of the hyperbolic mirror is traded for a cheap and fast manufacturing process since all mirror tiles are similar, while the spherical aberrations can be compensated by slightly tilting the mirror tiles outward, mapping the image distances of the individual mirror tiles onto each other. A more accurate imaging than the Davies-Cotton design is not necessary for our purposes since the TAIGA pixels are large and would not be able to resolve the difference of the image.

The image distance b of a spherical mirror with radius r in relation to the angle of incidence θ follows the equation

$$\begin{aligned}
 b &= r - s = r - \frac{\frac{r}{2}}{\cos(\theta)} \\
 &= r \cdot \left(1 - \frac{1}{2 \cdot \cos(\theta)} \right)
 \end{aligned}
 \tag{4.1}$$

with the labels as shown in figure 4.3.

Tilting the tiles outward reduces the incidence angle on the tiles so that the individual reflections are sharper focused. The individual tiles are not in an equal distance to the focal point of the main spherical dish, however, and

4.2. METHODS AND RESULTS

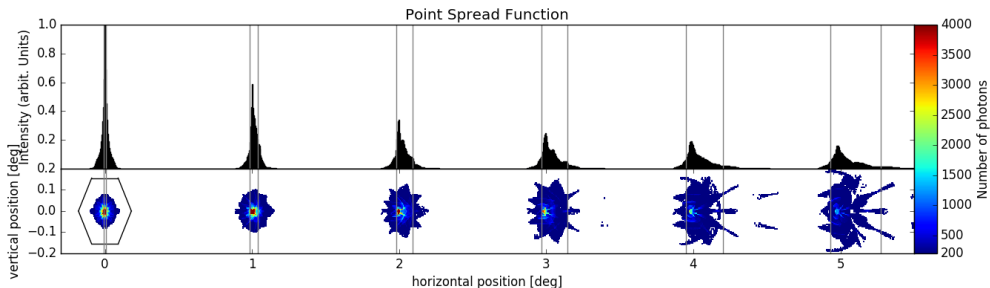


Figure 4.4: PSF for perfect TAIGA IACT mirror optics, with a minimum of 200 photons per bin to be plotted. Each spot represents a different off-axis angle, ranging from 0 to 5 degrees respectively. The vertical lines indicate the d_{68} containment radius, the hexagon represents the size and shape of a TAIGA pixel. The finger-like features are effects of the outermost mirror facets. For the perfect alignment, all spots are symmetrical in the direction perpendicular to the off-axis angle.

thus the size of the point spread function (PSF) of a Davies-Cotton setup is directly dependent on the *tessellation ratio*:

$$\alpha = \frac{r_{\text{tile}}}{R_{\text{dish}}} \quad (4.2)$$

with r_{tile} being the radius of an individual mirror facet and R_{dish} the radius of the overall mirror dish.

The geometrical contribution of the mirror optics to the PSF can be determined analytically, but all statistical elements have either to be estimated or directly be measured on built parts. Another way to determine the PSF is by MC ray-tracing of parallel light through the mirror optics.

The geometrically minimal PSF for the TAIGA IACTs has been determined with `sim_telarray` under the presumption of perfectly shaped, perfectly aligned mirrors.

Figure 4.4 shows the distribution of arriving photons for point sources at off-axis angles of 0°-5° in 1° steps for the perfect mirror alignment. While the 0° image is symmetrical and small, the spot size increases with increasing off-axis angles. Already at 2° one can see a secondary structure to the spot, made up by a superposition of the reflected spots of the individual mirror facets.

Figure 4.6a shows the photon distribution of the 5° off-axis spot in detail. The secondary structure of the spot can best be seen here, where the arrangement of the mirrors is the least optimised. While the transversal projection rises more slowly and therefore has a wider PSF, the d_{68} containment radius stays smaller than the size of a TAIGA pixel. This is valid for all smaller off-axis angles as well.

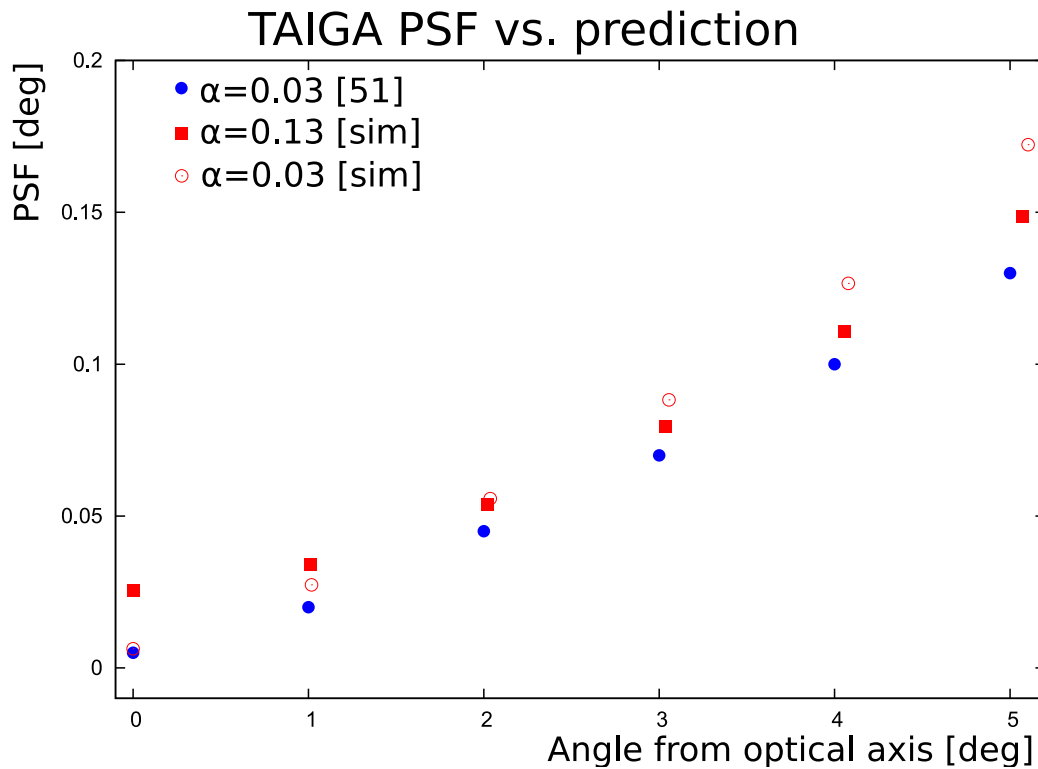


Figure 4.5: Comparison between the MC-determined TAIGA PSF (red solid points) and the semi-analytical prediction by Schliesser, Mirzoyan [51] (blue) for a $f/D = 1/1.4$ telescope. The empty red dots mark a MC simulation of a TAIGA-like telescope with $\alpha = 0.03$. The difference in slope is a direct consequence of the difference in tessellation ratio (0.13 (TAIGA) vs. 0.03 (prediction))

4.2. METHODS AND RESULTS

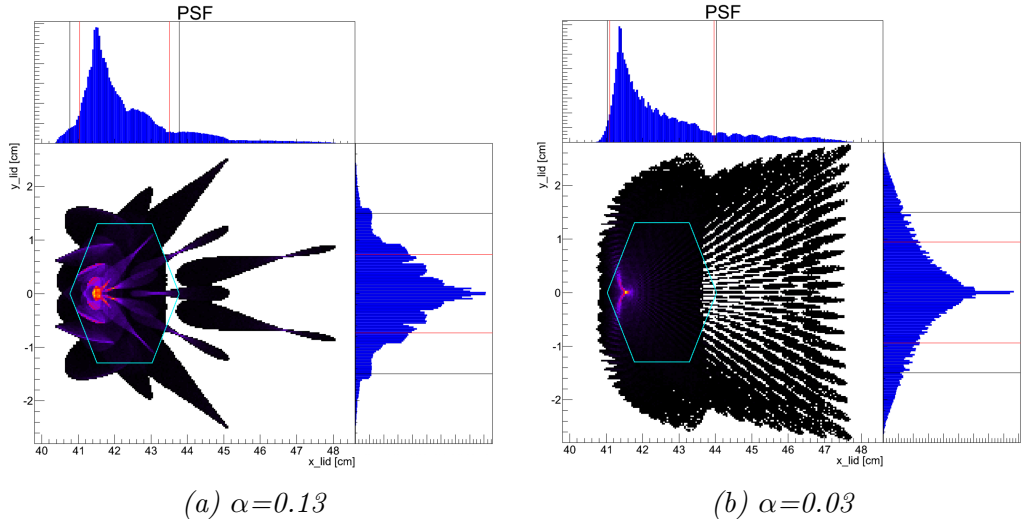


Figure 4.6: Comparison of the resulting image of a 5° off-axis star for TAIGA ($\alpha = 0.13$) and an otherwise TAIGA-like telescope with $\alpha = 0.03$.

The behaviour of the PSF with the off-axis angle is shown in figure 4.5. In this figure, the MC-determined TAIGA PSF is juxtaposed to a semi-analytical prediction made by A. Schliesser and R. Mirzoyan [51]. The order of magnitude for the PSF is about the same for the two data lines, but at first glance, the two models do not seem to match. At the very center, the semi-analytical model predicts a PSF of almost zero, while the TAIGA design retains a minimum PSF of 0.03° . For larger off-axis angles, the behaviour inverts: the analytical approach predicts a larger PSF value than the one for the TAIGA dish.

This difference in behaviour stems from the difference in tessellation ratio. The TAIGA IACT's tessellation ratio is $0.6/4.75 \approx 0.13$, and thus has relatively large mirror segments. The analytic solution assumes $\alpha = 0.03$, as was valid for the MAGIC telescopes. Scaled down to a TAIGA IACT main dish size, the corresponding mirror tiles are much smaller for the analytic solution. That this really is the effect of the difference in tessellation ratio is emphasised by the third data line in figure 4.5. This data line is the resulting PSF from a simulation performed for a TAIGA telescope with $\alpha = 0.03$, changing the number of mirror segments and their diameter while keeping all other parameters as before. The results match the shape of the analytical prediction well.

Larger mirror tiles mean stronger aberrations in the images of the individual mirror tiles, softening up the edges of the individual spots and widening the PSF in the center. On the other hand, not all mirrors are the same

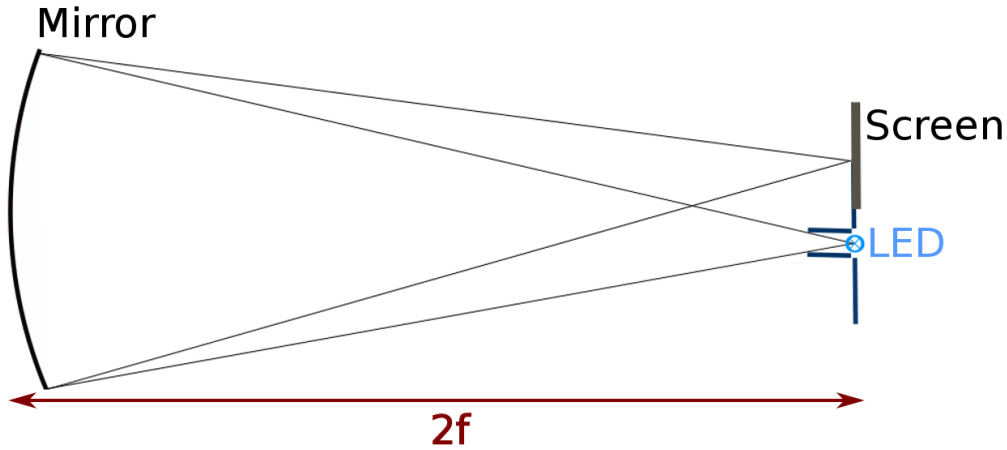


Figure 4.7: Mirror test setup for the $2f$ -method, schematic view.

distance from the focal point, so the reflections do not map perfectly onto each other for larger off-axis angles. The impact of this imperfect mapping is illustrated in figure 4.6, which compares a classical TAIGA image ($\alpha = 0.13$, left) of a 4° off-axis star with the same image by a TAIGA-like telescope with $\alpha = 0.03$ (from simulation, right). It can be seen that while the individual mirror spots may be smaller for smaller mirrors, they are spread out more, and thus the PSF gets larger.

Not only does the analytical prediction confirm the correctness of our simulation, it proves that a larger tessellation ratio is the right choice for an IACT with a large field of view. The slower increase of the PSF with off-axis angle of the TAIGA IACTs is preferable to the perfect center-imaging of a finely tessellated system. In the 10° of the TAIGA IACT's FoV, most showers will be seen at relatively large off-axis angles, while the center of the mirror dish is mostly shadowed by the camera body.

Other contributions to the PSF: The PSF shown thus far is only the minimal PSF without any hardware influences. The true amount of deviations that will influence the final PSF can only be estimated and depends strongly on the details of the design, like the mirror holding mechanism, the method of alignment or the production accuracy.

First of all, real mirrors need to be built. This by itself brings challenges that, while diminishable, cannot be fully eliminated. No item built will ever be without any manufacturing imperfections, which alone already reduces the

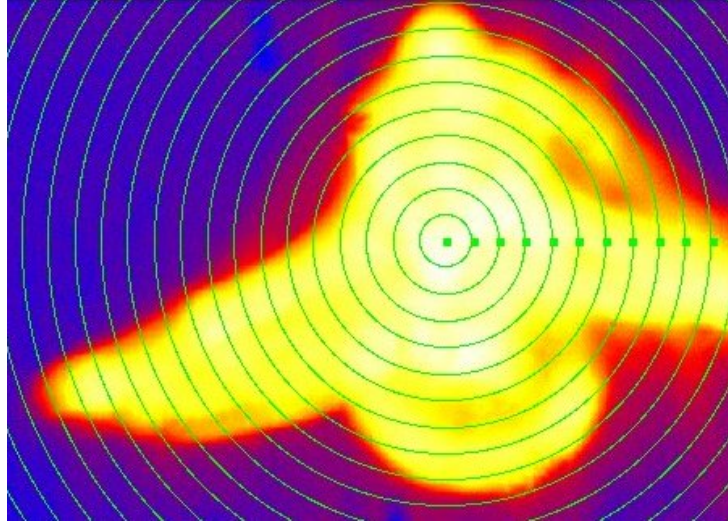


Figure 4.8: Example of an image taken with the setup shown in figure 4.7 in logarithmic colour scale. The green rings are the annuli used for analysis of the radial profile.

perfectness of a mirror’s imaging. This deviation is unknown by default and depends on the production facility and method. The TAIGA IACT mirrors are aluminised ground-glass mirrors. These mirrors start off as a thick layer of glass which is ground into spherical shape and then coated with a reflective layer of aluminium.

To get a good measure of the geometric imperfections of the mirror tiles, the 28 mirrors for the IACT prototype have been tested with the setup seen in figure 4.7. The mirror tile is mounted on a metal frame to hold it in place, a point light source is placed at the distance of its curvature radius. While parallel light is collected into the focal point, a source placed on the radius of curvature of a spherical mirror gets inversely reproduced back onto itself. If the source is point-like, the extension of the image is the PSF.

To get as close to a point source as possible, a blue high-luminosity LED with its plastic dome filed off to a minimum was glued to a 0.3 mm pinhole, with as little distance between the glowing semiconductor and hole as possible. This source was attached to a 20 cm collimator to restrict the emerging light to the viewing angle of the mirror to reduce the surplus light scattering on the surrounding hallway.

A screen was then used to find the reflected image next to the point source, which was placed a little off-axis at the radius of curvature (5-10 cm laterally from the main axis, $\approx 1\text{-}2^\circ$) so that the image does not reflect directly onto the source. Once the spot was found, a CCD camera mounted on an optical

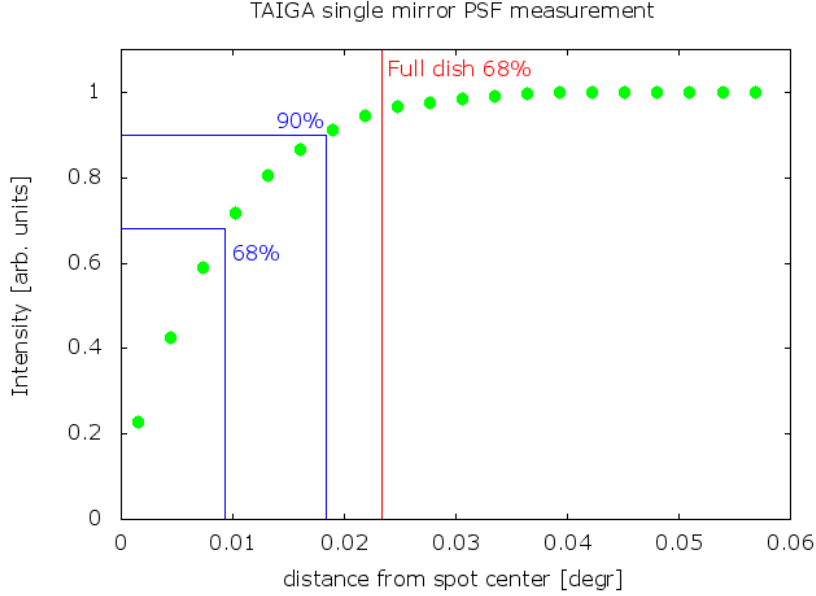


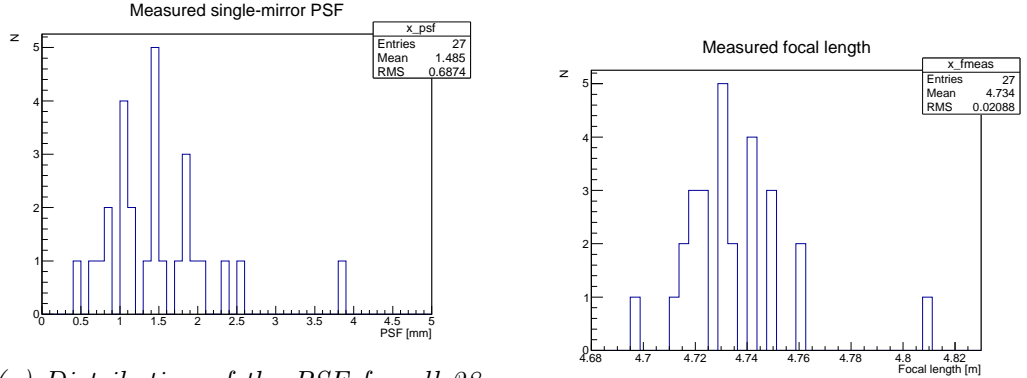
Figure 4.9: Cumulative radial profile of the PSF of a single mirror facet as seen in figure 4.8. The blue lines mark the d_{68} and d_{90} containment radii of the single-mirror measurement presented, the red line marks the full dish d_{68} as computed by MC simulation.

bench was placed at the point of smallest image extension, so that the light fell directly on the CCD without any use of concentrating optics. Figure 4.8 shows a typical image taken by this method. The triangularity of the image can be explained by the production process, the glass rests on a tripod while grinding and at the position of the resting points the glass can not give way as much as between the resting points, so the mirror gets a very slight triangular shape deviation.

To analyse the image, the "annulus" tool from the program DS9 [52] was used. DS9 is a .fits file analysis program designed by NASA for analysis of star images. The annulus tool splits an area up into concentric rings. The amplitude of all pixels is individually integrated for each ring and then divided by the respective area of each ring, yielding an average amplitude for every distance from the center. If the annuli are centred at the brightest spot of the image (the approximate CoG), these annuli profiles give the PSF in the dimension of pixels. With the size of the pixels known from the camera data sheet and the distance to the mirror known from the setup, the angular spread can be calculated as well and is shown for one example mirror in figure 4.9.

The values for all 28 mirror segments for the prototype IACT can be

4.2. METHODS AND RESULTS



(a) Distribution of the PSF for all 28 TAIGA mirror segments. The average PSF is 1.5 mm, which equals to 0.02° at focal length.

(b) Distribution of the measured focal distances for all 28 TAIGA mirror segments.

Figure 4.10: Measured mirror values

seen in figure 4.10a and found in appendix A. For all mirrors the PSF is distinctively smaller than the all-mirror PSF, so the single-mirror PSFs will only have a weak influence on the overall PSF. The average PSF for the mirror tiles is 1.5 mm, correspondent to 0.02° , a value that is taken as the respective simulation parameter.

The only outlier is mirror number 10 with a PSF of about 4 mm or approximately 0.04° . While still usable, this mirror is of poor quality, and since this mirror tile bears no obvious damages, imprecise manufacturing must be the origin of these deviations.

Figure 4.10b shows the measured focal distances of the mirrors. All mirrors have a focal distance close to the 4.75 m needed for the telescope, within the measurement accuracy (± 2.5 cm per mirror). The only outlier is mirror 24, as the focal length of 4.82 m deviates strongly from the mean focal length of 4.73 m.

That mirror 24 is off by more than 5 cm does not render it unusable. For all but the centermost mirror, the telescope's overall focal point lies farther away than the mirror tiles' individual focal points, where the rays from the tiles already start to spread out again. A larger focal length can therefore be an advantage for the outer mirror tiles because when the difference between the tile's focal length and the distance between mirror and overall focal point shrinks, the amount of spread due to being farther away than the focus is reduced, an effect that is most strongly felt on the outermost tiles.

Measuring the focal length of all the mirror tiles before deployment and mounting them on the main dish with the largest focal length as the outer-

most mirrors can thus have an improving effect on the PSF.

Not only the single mirror PSF, but also the precision of mirror alignment has a strong impact on the shape and size of the all-mirror PSF, as can be seen in figure 4.11. The reflections of the single mirrors overlap to form the resulting total image, and the farther out of the camera center the source sits, the more do the outermost mirrors reflect their light off-center.

To give an estimate of the mirror alignment precision, one has to take a look at the construction details and the adjustment process. The mirror tiles are mounted on three points, with one being a ball joint and the other two threaded bars. To align, the whole dish is lightened by a LED-illuminated panel at 800 m distance as a homogeneous light source and the resulting single-mirror spots are aligned to the center of the camera manually. The thread of the bars provides a lift of 0.075 cm per turn at 30 cm distance from the joint which, with an optimistically estimated turning precision of 1/100th of a turn for a human hand, yields a technical limit of $\pm 0.028^\circ$, corresponding to about 2 cm in the camera plane. The overlapping of the spots on the camera is done by eye, with the spots' position harder to see the more mirrors are already aligned, but the human eye is capable of a finer adjustment than the slippage in the thread allows.

Also, the alignment of the mirrors is done in a horizontal resting position. As soon as the telescope is moved to a different zenith angle, the gravitational strain of the telescope's own weight deforms the overall shape of the dish as illustrated in figure 4.12.

To neutralize the impact of the heavy camera, the mirrors and the camera support sit on different frames. The deformation of the camera suspension arms (red) only makes for a shift between camera center and mirror main axis, which can be countered with proper calibration.

The only deformation of the mirror dish (blue) is caused by the weight of the mirrors and their support structure itself. The design drawings estimate the total weight of the mirror support structure to be about 2000 kg, and thus, given its roughly H-shape, we can simplify down to each beam carrying about 500 kg more or less evenly distributed along its length of about 1.6 m.

The deformation of a beam that is fixed in one end ("cantilever beam") under uniform load follows the formula

$$\Delta s = \frac{\delta_F L^4}{8EI} \quad (4.3)$$

with $\delta_F = M_{dish} \cdot g/L$ being the force per m applied to the beam of length

4.2. METHODS AND RESULTS

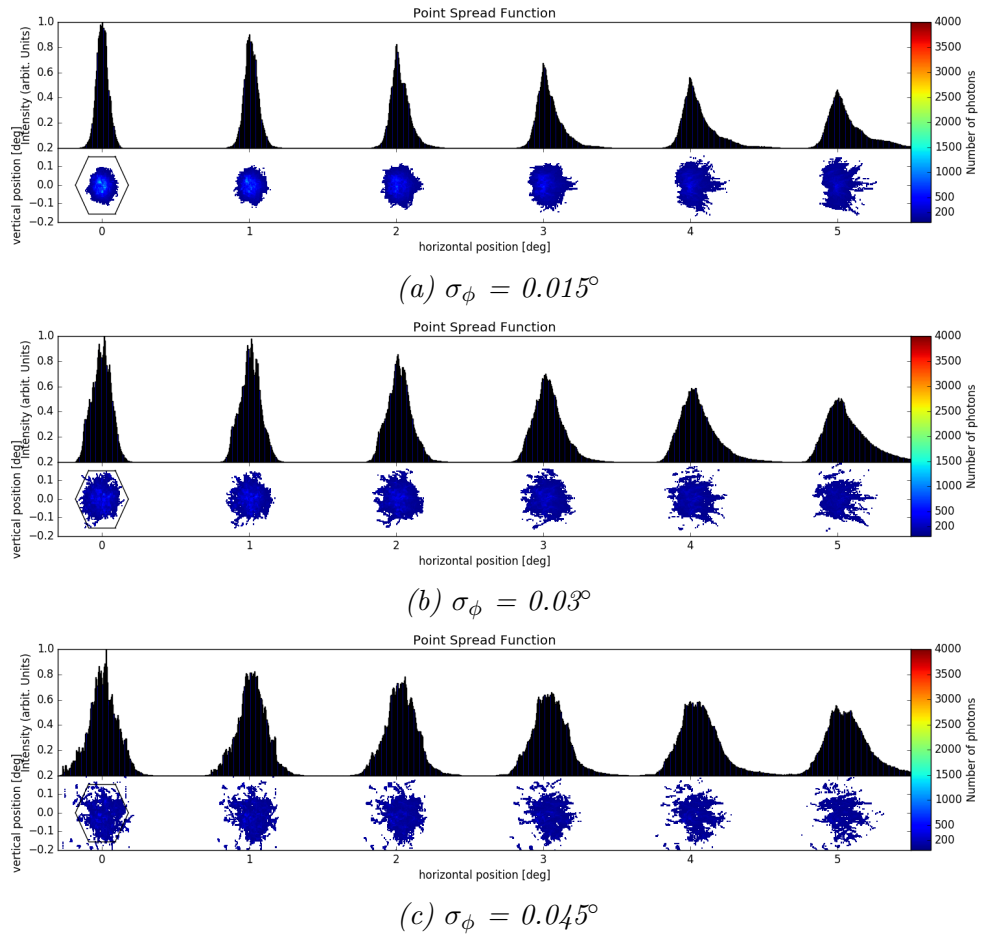


Figure 4.11: Example for the PSF for mirror optics with different imperfections of the mirror alignment σ_ϕ . Each spot represents a different off-axis angle, ranging from 0° to 5° respectively. The hexagon represents the size and shape of a TAIGA pixel. The spots vary in shape as the alignment varies per mirror facet.

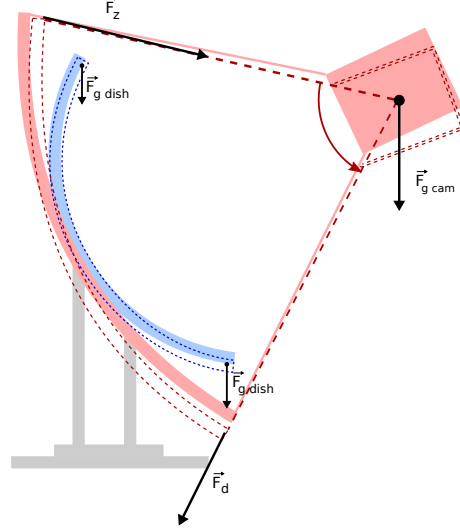


Figure 4.12: Illustration of how the telescope deforms under its own weight, with arrows marking the direction of the participating forces. Proportions exaggerated for illustration. $F_{g \text{ cam}}$ is the total weight of the camera, $F_{g \text{ dish}}$ is the amount of force the dish support has to bear at that point since the weight is distributed along the beam.

L , $E = 210 \cdot 10^9 \text{ N/m}^2$ the elasticity modulus of steel, and

$$I = \frac{bh^3 - (b - 2t)(h - 2t)^3}{12} \quad (4.4)$$

the second moment of inertia for a rectangular hollow beam of height h , broadness b and thickness t .

Since h , b and t are fixed by construction, the only parameter that is dependent on the zenith angle θ is the force exerted by the mass of the construction.

$$\delta_F = \frac{m \cdot g}{L} \cdot \sin(\theta)$$

Disregarding the curvature of the beams, rounding and inserting the design values of the telescope, the maximum deformation at $\theta = 0^\circ$ amounts to

$$\begin{aligned} \Delta s &= \frac{3125 \cdot \sin(0^\circ) \cdot (1.6)^4}{8 \cdot 210 \cdot 10^9 \cdot \frac{1}{12} (0.15 \cdot (0.15)^3 - (0.15 - 2 \cdot 0.005)(0.15 - 2 \cdot 0.05)^3)} \\ &= 1.198 \cdot 10^{-3} \text{ m} \\ &\approx 1.2 \text{ mm} \end{aligned}$$

4.2. METHODS AND RESULTS

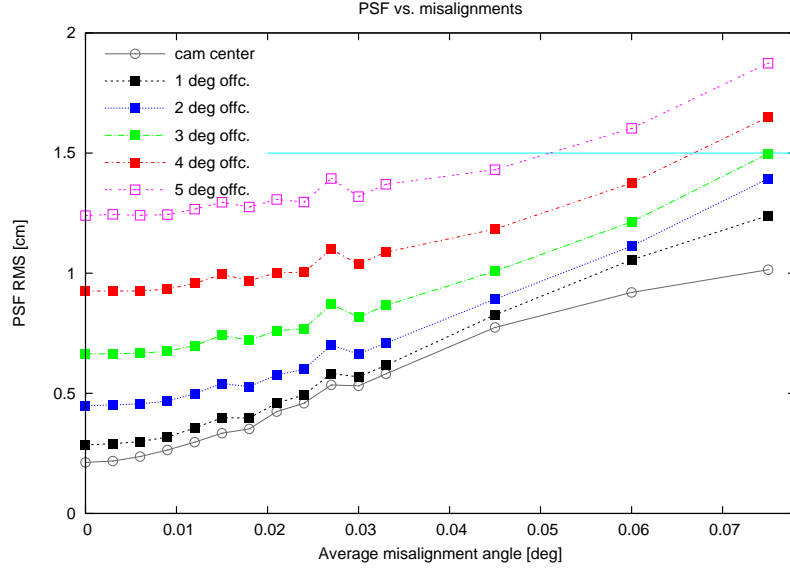


Figure 4.13: Behaviour of the TAIGA PSF for different mirror misalignment values. Different colours represent different off-axis angles, points are connected for visualisation, not as a fit. The horizontal line shows the radius of a TAIGA pixel.

The minimum of the deformation is found at $\theta=90^\circ$ and is (almost) zero.

A deformation of 1.2 mm on a 1.60 m beam results in an angular change of 0.02° . Since the mirror adjustment can only be done while in horizontal position, but the observations will be carried out at varying zenith angles, mostly around $25\text{--}35^\circ$, but up to around 50° to keep up with the tilted HiSCORE stations, the distortion will be small most of the time. A way to reduce the deformation effect would be to adjust the mirrors while in observation position, but this is not possible yet.

The direction of the misalignment due to deformation is not randomly distributed, but rather the mirror tiles are reliably tilted outward when the telescope is moved to a vertical position. The amount of deformation-caused misalignment also depends on the position of the mirror tile since a beam deforms continually and the closer the mirror sits to the fixed point of a cantilever beam, the smaller the deflection is. This makes the total misalignment value both direction- and position-dependent as it is the sum of the uniform alignment error and the direction- and position-dependent deformation error.

Figure 4.13 shows the behaviour of the all-mirror PSF for different average misalignment values, with the pixel size marked in cyan. A subset of corresponding profiles can be seen in figure 4.14. While the PSF rises with increasing misalignment value, even at a pessimistic misalignment error of 0.06° , only the outermost edges of the camera receive a spot that is larger than

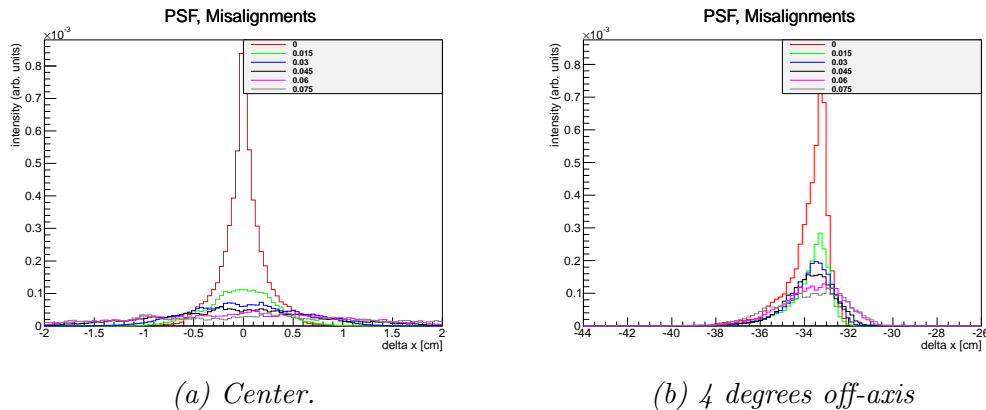


Figure 4.14: Longitudinal profile of the photon distribution for a star in the center (left) and 4° off-axis (right) for different values of mirror misalignments.

the pixels. This does not impact the performance much because showers that deposit the most light in those pixels are typically rejected by the nominal distance cut (distance camera center - shower center of gravity $< 4^\circ$).

Effective area

The detection rate of a flux Φ for a zenith angle θ can be calculated with [53]

$$R(\theta) = \int^{\Omega_0} d\Omega \int^{E_0} A_{\text{eff}}(E, \Omega, \theta) \frac{d\Phi}{dE} dE \quad (4.5)$$

for the solid viewing angle Ω and the primary energy E . The parameter A_{eff} is called the *effective area* of the detector and reflects the fact that a true detector can not make use of its full area, but rather has its area reduced to its effective area by the imperfect detection probability. This detection probability in turn is dependent on several detector-specific factors, for IACTs the strongest factors are incidence angle, energy and impact parameter.

To keep the observation time reasonable, a sufficiently high event rate is desired. Since the flux is nature-given and cannot be changed, to increase A_{eff} is the only way of achieving high enough rates for UHE observation, and A_{eff} is a direct measure of a detector's detection capability.

From MC simulation, the effective area can be directly computed from the ratio between detected and simulated showers for showers spread over an area A_{dist} large enough that the outermost showers will definitely not trigger the telescope any more. The effective area is then computed with

$$A_{\text{eff}} = \frac{N_{\text{triggered}}}{N_{\text{simulated}}} \cdot A_{\text{dist}} \quad (4.6)$$

4.2. METHODS AND RESULTS

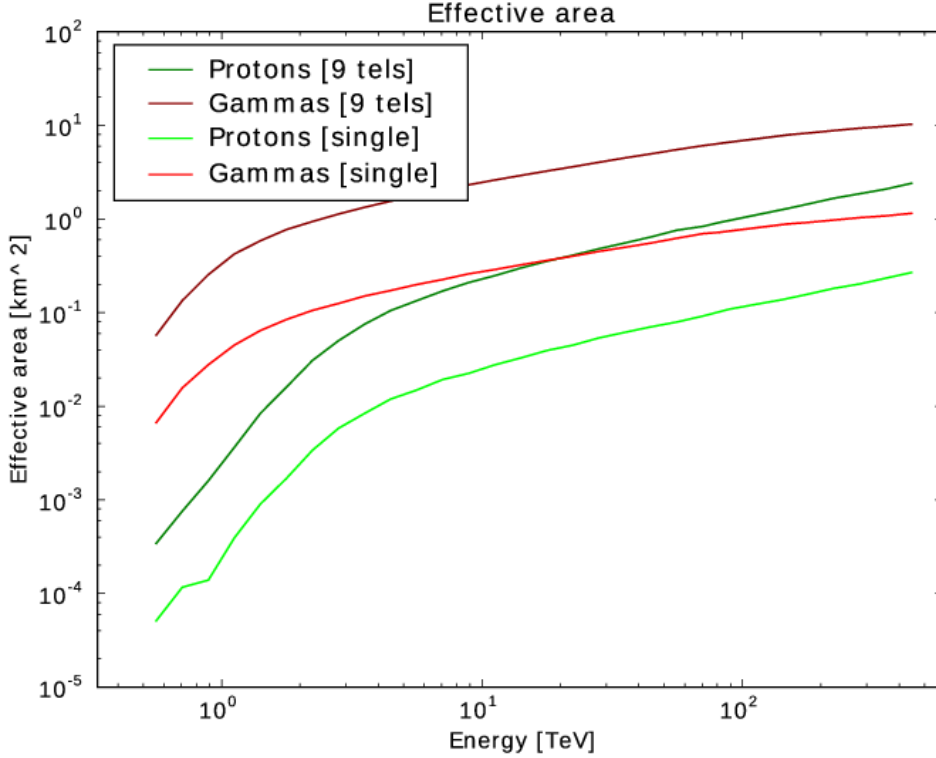


Figure 4.15: Effective area vs. primary energy for a single TAIGA IACT (bright) and the 9 telescope system (dark) for gammas (red) and protons (green). Protons produce about 1/3 of the light of a gamma shower with the same energy, so the effective area is different for different primaries.

Both the effective area of a single TAIGA IACT as well as the whole 9-telescope array can be seen in figure 4.15. The data set used to obtain the effective area consists of gamma and proton showers spread out over a circular area with 3 km radius. A detailed description of the data sets can be found a little further on in table 4.1.

A shower triggers the telescopes only if it is bright enough, so the effective area is tightly tied to the LDF. The steep rise at lower energies stems from the showers that are only bright enough to trigger the telescope if they are really close. At 2 TeV and about 0.06 km^2 (for single-telescope gammas), the area starts to increase more slowly. This area corresponds to a circular area with a radius of about 140 m, which is the size of the brightest region of a shower's Cherenkov light cone. This radius can be described as the telescope's viewing distance, the distance at which a shower can still trigger the telescope. The following slower rise is a consequence of the exponential

drop of the LDF's tails with core distance.

For different primaries, the effective areas are different. Protons above 1 TeV produce about a third of the light of a gamma shower because a part of shower energy is converted into hadrons, muons and pions who are fewer in number and therefore produce less light. This is particularly obvious near the energy threshold: The area for the gammas reaches its flattening at about 1-2 TeV, while protons at this energy are hardly detectable with the TAIGA IACTs ($A_{\text{eff}} = 10^{-4} \text{ km}^2$ corresponds to an impact parameter of 17 m). For higher energies, the relative impact of the primary on the effective area lessens, even though it never fully disappears. The relative difference shrinks because the fluctuations in the electromagnetic shower component of the proton showers decreases and therefore the relative fluctuation in shower brightness drops, and all showers produce enough light to always trigger the array.

The effective area of an array of detectors is harder to describe than the area for a single detector. In detector arrays, the detectors' "viewing distances" overlap and the precise arrangement of the detectors determines the arrays' detection capability.

At TAIGA, most showers are seen by only one telescope with only very little overlap in the viewed areas. This is reflected in the 9-telescope effective area (figure 4.15, darker lines), which is approximately 8.5 times larger than the single-telescope area, with otherwise similar features concerning initial steepness and flattening with energy. This factor 8.5 decreases with rising energy since the larger the shower energy, the more showers are detected with a multiplicity of 2 or more.

4.2.2 Energy reconstruction

The energy of an EAS can not be measured directly since it is distributed among all the involved particles. The only accessible parameter at ground level is the total amount of light produced in a shower, i.e. the shower size of the image taken. The image size furthermore depends on core distance to the telescope, the telescopes' collection area, shower zenith angle and shower primary.

Gammas and protons of the same energy produce different amounts of light. So, in order to use the right shower values for cuts and filters, we cannot use the true Monte Carlo energy, but must first reconstruct the energy from the respective image size to reproduce the systematic underestimation of proton energies.

4.2. METHODS AND RESULTS

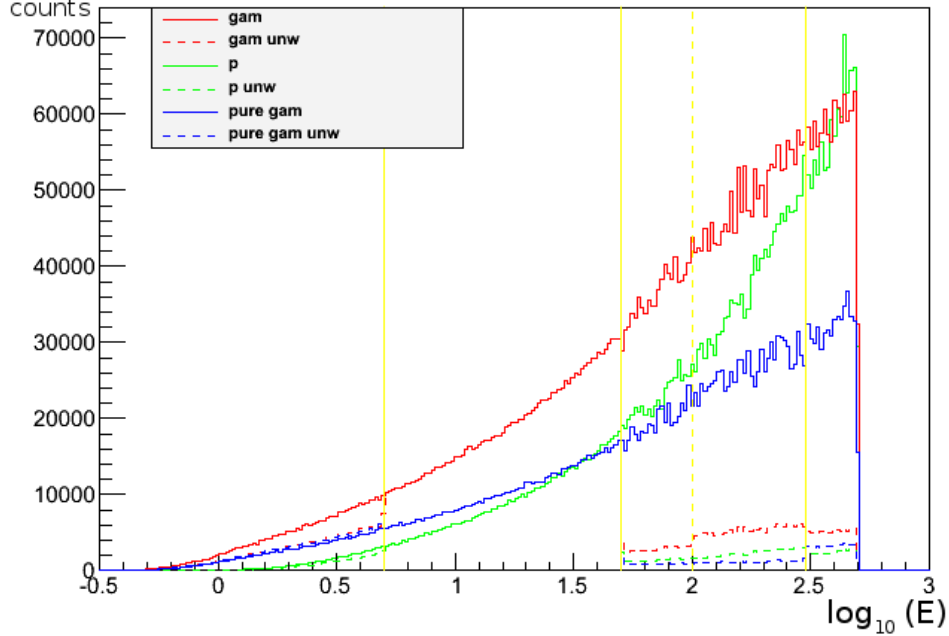


Figure 4.16: Data sample statistics for the pure gamma (blue) and the mixed gamma (red) and proton (green) dataset, before (i.e. unweighted, dashed) and after (solid) normalisation. Yellow lines indicate the borders of the simulated energy ranges. Triggered events only. The bigger slope of the proton sample is a result of the bigger increase of the effective area with energy for protons.

Statistic normalisation

Different energy ranges take different amounts of computing time, so for efficiency, the overall dataset was not computed in one block, but in several smaller energy ranges. In the raw resulting data set, some energy ranges are more prominent than others, as can be seen in figure 4.16 as the dashed line. Performing a fit or any other analysis on the raw data would skew the results due to the increase in weight for the more prominent energy ranges. Thus, before the energy can be reconstructed, the data samples must first be matched to each other so that each of them contributes an even weight to the energy fits and all further analyses.

The simulations have been performed in several energy ranges with a different amount of events in each bin. Also, the energy bins are not all equal in logarithmic size and differ in the area over which the showers were spread out. All these aspects contribute to the normalisation factor:

4.2. METHODS AND RESULTS

	E [TeV]	Prim.	$N_{\text{sim}} [10^6]$	$N_{\text{tr}} [10^3]$	$r_{\text{scatt}} [\text{km}]$	n_i
pure	0.5-5	γ	7.50	183.0	3	0.97
	5-50	γ	7.50	743.0	3	1.00
	50-300	γ	0.22	57.2	2	23.10
	300-500	γ	0.08	51.7	2	9.85
	0.5 - 500	γ	15.3	1 040		
mixed	0.5-5	γ	7.40	189	3	1.62
	5-50	γ	12.00	1 370	3	1.00
	50-100	γ	0.40	60	3	12.95
	100-300	γ	0.28	181	3	9.21
	300-500	γ	0.13	83	3	11.34
	0.5 - 500	γ	20.2	1 880		
mixed	0.5-5	p	17.00	40	2	1.37
	5-50	p	2.80	660	2	1.00
	50-300	p	1.20	110	2	16.29
	300-500	p	0.30	39	2	23.72
		0.5 - 500	p	21.25	850	

Table 4.1: Datasets and normalisation factors

4.2. METHODS AND RESULTS

$$n_i = \frac{N_i}{N_{\text{ref}}} \cdot \frac{\Delta_E}{\Delta_{E_{\text{ref}}}} \cdot \frac{A_i}{A_{\text{ref}}}$$

with N_i and N_{ref} the amount of simulated showers in a data range, Δ_E and $\Delta_{E_{\text{ref}}}$ the logarithmic energy range and A_i and A_{ref} the respective scattering areas. Since the respective 5-50 TeV energy range was chosen as reference for the different datasets, $\Delta_{E_{\text{ref}}}$ equals one. The individual aspects as well as the resulting normalisation factors can be found in table 4.1.

Figure 4.16 shows the amount of triggered showers with energy for the different energy ranges, before (dashed) and after (solid) normalisation. A higher energy means a brighter shower, and therefore a higher percentage of triggering showers with energy, and while the distribution of simulated showers over energy is flat after normalisation, the amount of triggered showers rises exponentially.

It can be seen that the proton line rises steeper than the gamma distributions. This is systematic and a result of the steeper increase of the effective area with energy for protons.

The fit

For a specific telescope and a specific zenith angle, the relation between $\log(\text{energy})$ and $\log(\text{size})$ is linear and only dependent on the core distance. Since all gamma showers were simulated from the zenith, the energy fit covers only $\theta = 0^\circ$.

Figure 4.17 shows the logarithmic size vs. energy distributions for core distances of 50 m, 350 m, 500 m and 650 m. It can be seen that with increasing impact parameter, the relation between size and energy flattens out. For smaller core distances, this is because the inner part of the LDF changes strongly with energy, while larger impact parameters only catch the tails of the LDF where the change is relatively small.

For the largest distances (>500 m), the flattening becomes extreme due to another cause. At these distances, only the showers with the highest energies are detected at all. The fit is performed on only a few bins, and these bins do not even have a fully reliable mean because the used data set cuts off at 500 TeV. Leaving out the contribution of higher energy showers to the size-energy fit skews the distribution towards a flatter relation. Simulations of showers with $E > 500$ TeV would be necessary to improve the fit at these distances, but due to the low number of events at that distance, this step has been omitted.

The resulting fit parameters were written into a file and subsequently used in any further analyses.

4.2. METHODS AND RESULTS

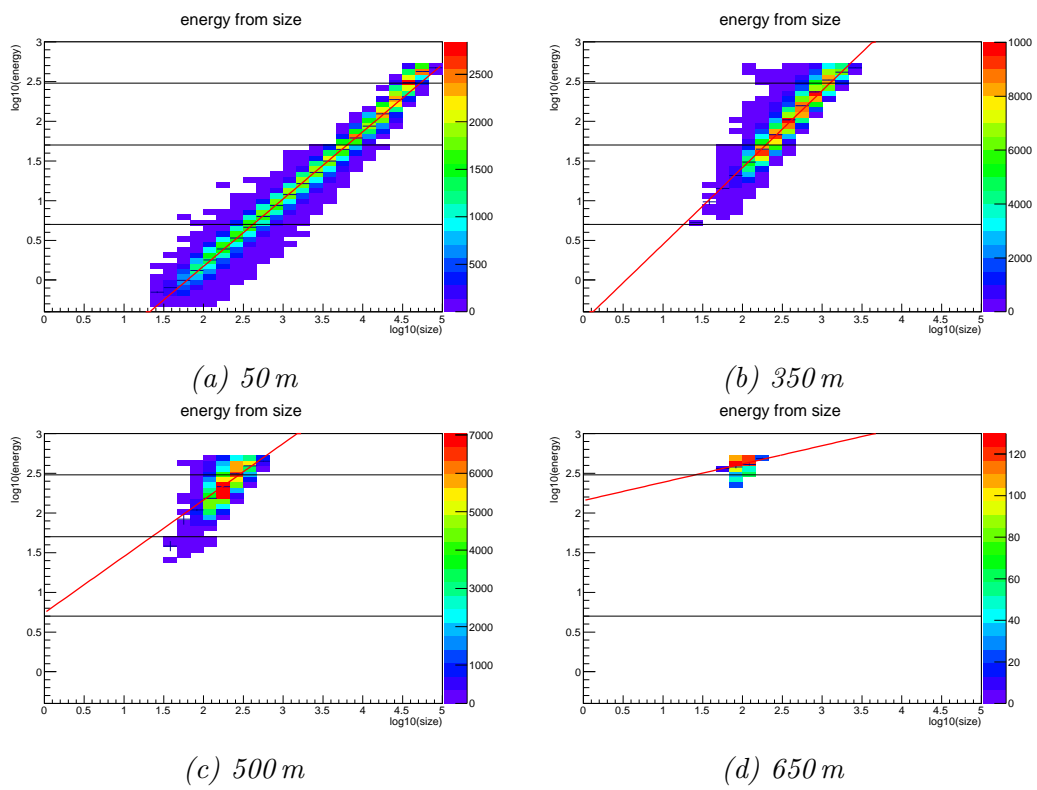


Figure 4.17: Fit: Image size vs. primary energy for different core distances

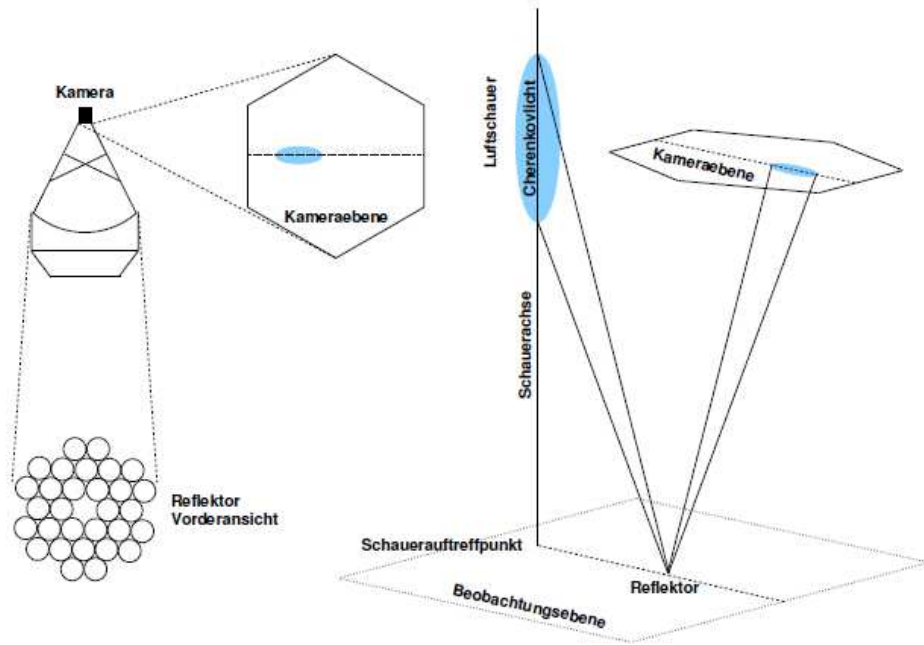


Figure 4.18: Schematic view of imaging with a cherenkov telescope [54]. After being reflected on the telescope mirror, the shower leaves an elliptic image on the camera.

4.2.3 Combination

In its final stage, the combination of the HiSCORE array with IACTs requires a full hybrid reconstruction algorithm. This hybrid reconstruction algorithm is complex and, while first steps have been made, has not been focus of this thesis. Also, the algorithm was not complete by the time of this thesis.

To get preliminary results of a combination without having the full reconstruction algorithm available, the simulation algorithms `sim_score` and `sim_telarray` were used independently of each other, and the results interpreted together as far as possible.

Shower reconstruction from telescope images

IACTs take a direct image of the Cherenkov emitting region of a shower. This region has a cigar-like shape and yields an elliptic image on the camera as illustrated by figure 4.18. To interpret this image, the image is first cleaned of all noise by a so-called *image tailcut*. The tailcut constrains the images to the pixels that actually contain signal as pixels that do not catch any shower light only contain electronic noise and *night sky background* (NSB) light.

Two varieties of the tailcut are commonly used among IACT collaborations: The two-level tailcut and the constant fraction tailcut.

The classic two-level tailcut as illustrated in figure 4.19 uses all pixels above a threshold of a certain number of photoelectrons (pe) plus all pixels that are above a slightly lower threshold (3 pe) that have at least two neighbours above the first threshold. The thresholds used for the TAIGA IACT's are 5 pe for the upper threshold and 3 pe for the lower one.

The constant fraction tailcut works similarly, but with all thresholds depending on the amplitude of the pixel with the largest signal. In both cases, all pixel signals not making the cut are discarded. The constant fraction tailcut slims down the width of the image ellipse for higher energy showers as pixels on the fringes of the image ellipse get rejected that would pass the two-level tailcut. Since the image width is the main parameter used, it was decided not to use the constant fraction tailcut in this work.

After image cleaning, the ellipse is parametrised into the so-called Hillas [46] parameters as shown in figure 4.20. Many of these parameters use the formula for the central moments μ_{ij}

$$\mu_{ij} = \sum_x \sum_y (x - \bar{x})^i (y - \bar{y})^j f(x, y) \quad (4.7)$$

for all image pixels with the coordinates (x,y) and the amplitude f(x,y). The most important Hillas parameters are:

- The *center of gravity* (CoG) of the image ellipse is the first moment of the amplitude distribution in the camera.

$$CoG = \frac{\sum_i (a_i \cdot (x_i, y_i))}{\sum a_i}$$

Note that even though the circumference of the image is elliptical, the CoG does not necessarily lie at the geometric center of the ellipse. At core distances larger than 50 m, the CoG is shifted slightly to the end of the ellipse that lies closer to the projected source position.

- The *image size* is the total sum of all image pixel amplitudes after the tailcut, the zero-th moment.
- The image *distance* is the distance of CoG to the camera center.
- The *angle* α describes the angle between the ellipse's main axis and the connection CoG - camera center. Therefore, alpha shows the orientation of the shower image.

4.2. METHODS AND RESULTS

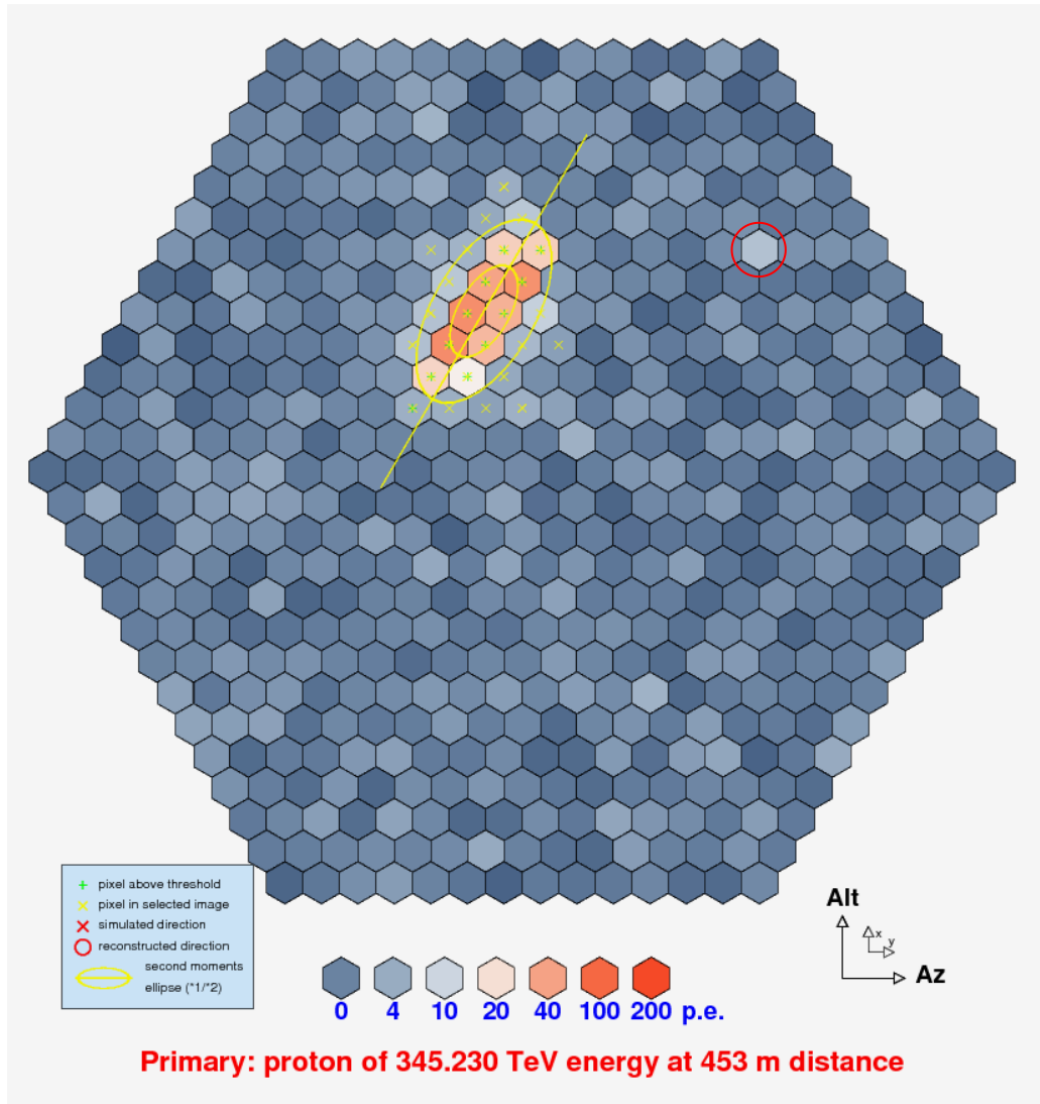


Figure 4.19: IACT image on which the pixels that are considered part of the image are marked. Green markers are pixels that have an amplitude above the main threshold, yellow marked pixels are part of the image due to their neighbours. The red marked pixel is an example for a rejected pixel: while its amplitude is higher than some of the selected pixels, it lacks the neighbours above the main threshold and is therefore considered noise.

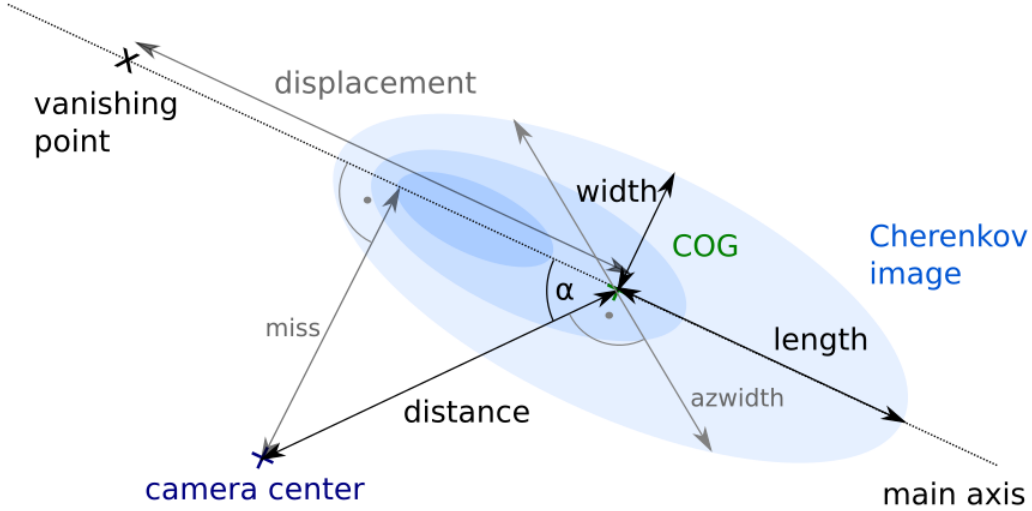


Figure 4.20: The Hillas [46] parameters as found in an IACT camera image.

We get α as

$$\alpha = \frac{1}{2} \arctan \left(\frac{2\mu_{11}}{\mu_{20} - \mu_{02}} \right) \quad (4.8)$$

- *width* and *length* of the image ellipse are calculated from the second moments.

The width and, even though a less strong parameter, also the length can be used to discriminate between gamma and hadron induced showers because hadronic showers have, on average, wider images.

- The *disp* parameter is the displacement between the COG and the vanishing point of the shower direction. The vanishing point is the point where an infinitely far away point on the shower axis (= the source) would be reproduced in the camera frame, and therefore equal to the direction.

By displacement alone, the point of origin is still ambiguous. Two areas on the main axis, one on each side of the ellipse, come into consideration. The decision on which is the right point of origin can either be made based on the asymmetry of the image, which is gained from a higher order image analysis, or on additional information, for example a triggering HiSCORE station, as is being studied in [55].

From these parameters, the shower direction, impact point and energy can be determined, as well as a certain distinction between primaries can be made.

4.2. METHODS AND RESULTS

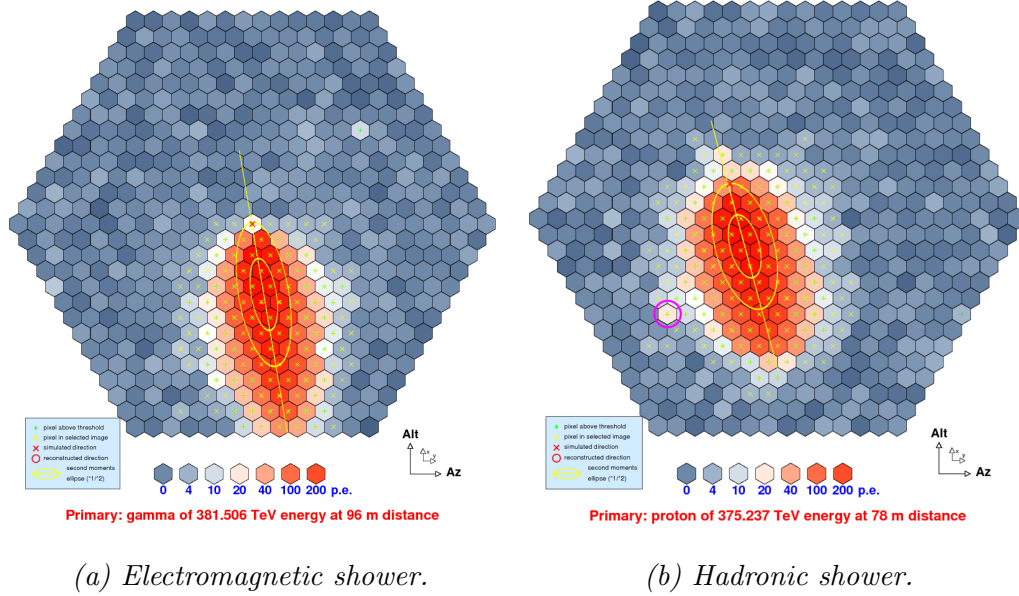


Figure 4.21: Two typical camera images for an electromagnetic and a hadronic shower of similar energy and core distance. Both showers are primarily elliptic, with the CoG of the gamma shower clearly shifted more towards the shower direction. The hadron shower is wider and more irregular, with a single high-amplitude pixel outside the main bulk of the shower image (marked in pink).

Gamma Hadron Separation

The primary intention of combining the HiSCORE array with IACTs was to improve the gamma-hadron separation of detected events.

The feature in which the two primaries differ most is the width of the camera image. It can be used to discriminate between the different primaries.

Two typical camera images can be seen in figure 4.21. 4.21a shows a regular EM shower with a smooth elliptic image. The point of highest intensity is shifted a little to the incidence direction because the shower maximum does not lie in the middle of a shower's lifetime but closer to the ground.

A hadronic shower as seen in 4.21b is more irregular and wider since the particles can receive a larger transversal momentum in the hadronic interactions. The majority of Cherenkov light is emitted in several electromagnetic sub-cascades caused by the decay of pions that were created in the hadronic interactions.

As described in chapter 4.2.3, the parameter used to discern gamma showers from hadronic showers is the width of the image ellipse after tailcuts.

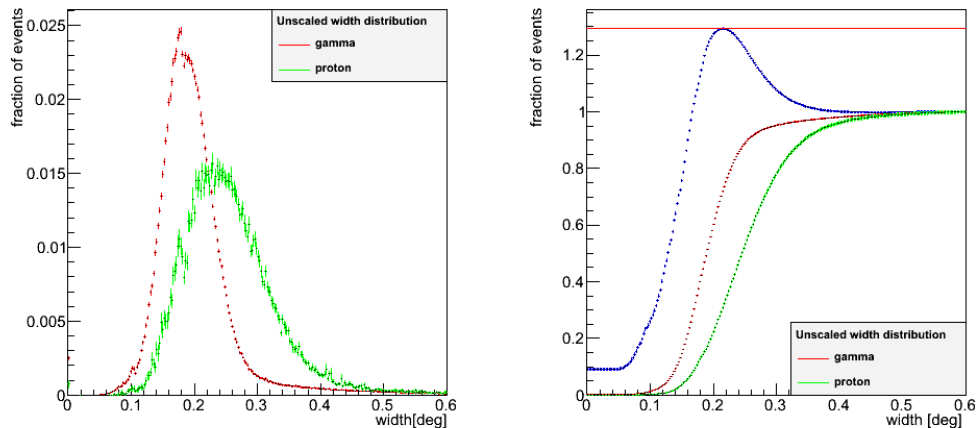


Figure 4.22: Unscaled raw image width distribution for a TAIGA telescope for showers from the zenith, left: differential, right: cumulative. Red: gammas, blue: protons. The two distributions overlap strongly. The blue line denotes the quality factor Q if a width cut is performed at the respective value, with its maximum at not even 1.3.

Raw data: Figure 4.22 shows the raw image width distribution for TAIGA IACT images. This distribution was obtained from the “mixed” data set in table 4.1 with $1.88 \cdot 10^6$ gamma and $0.85 \cdot 10^6$ proton showers from 0.5-500 TeV. Core distances in the distribution vary between 0 m and about 700 m, with showers further away from the telescope simulated, but not triggering the system and therefore not contributing to the image width distribution.

The difference in image width for the two different primaries is very apparent in this image width distribution. Electromagnetic showers show a relatively narrow distribution as they only contain an electromagnetic cascade. The hadronic distribution is wider due to the shower-to-shower fluctuations caused by the hadronic part of the cascade. The larger transversal momenta make for a tendency towards larger widths.

To assess the quality of a cut, the *quality factor* Q can be introduced:

$$Q = \frac{N_{\text{EM}}}{\sqrt{N_{\text{hadr}}}} \quad (4.9)$$

Q evaluates the number of retained EM showers against the number of kept hadronic showers. It is directly associated with the sensitivity of the detector, as the sensitivity improves linearly with the quality factor independent of observation time or, respectively, with a doubling of the quality factor, a source can be observed with the same sensitivity in one fourth of

4.2. METHODS AND RESULTS

the time.

The cumulative distribution shown on the right shows directly what percentage of the showers of which kind is retained if the cut is made at a certain width. The maximum quality of the cut does not exceed 1.3 due to the strong overlap of the gamma and the proton distribution.

Cuts: It is obviously not easy to reliably tell if a shower was gamma- or proton-induced from the raw width alone. A good way to increase the quality factor of a width cut is to introduce further supportive cuts.

A very typical cut for IACT source observation is the alpha-cut. Alpha is the angle between the shower's main axis and the connection camera center - shower COG. Cutting on this value rejects showers that come from certain directions, therefore rejecting the hadronic background showers by predefining source and background regions. This cut mode is ideal for the observation of point sources and can yield a very high quality factor (>100), but is not suited for observation of extended regions and especially not for wide-angle observations. This also applies for cuts on parameters that depend on alpha, such as the azwidth. Therefore, the directional alpha cut and cuts on its derivative parameters have deliberately not been studied for TAIGA.

One of the cuts performed is the nominal distance cut, cutting on the distance of the images' COG to the camera center. Showers with a distance of more than 4° (for TAIGA) are usually truncated by the camera edge and therefore appear wider than they actually should be because of the missing amplitude outside of the camera boundaries, independent of primary.

Another step is a cut on the core distance to the telescope. With larger core distance, the amount and distribution of light arriving at the telescopes stems from the tails of the LDF. The relative differences in observed width between a gamma and a hadron shower start to shrink as an ellipse seen at a greater distance has a smaller viewing angle as one seen closely, and the camera resolution provides a natural minimum of resulting image width. The resulting quality factor for large distances is therefore not ideal.

Also, especially high energy proton showers may produce muons at relatively large off-axis angles. These muons produce very intense rings of light that are seen at extremely large core distances. The resulting images are usually not ring-shaped, but only catch a segment of the ring, resulting in a small image width and are often misinterpreted as gamma events. Therefore, the maximum core distance should be constrained to a value at which the telescopes still trigger on the actual shower light. For the TAIGA telescopes, this distance lies at about 800 m.

The layout of the array however allows an even stricter limitation of core

nominal distance	$<4^\circ$
core distance	<300 m
energy	>20 TeV

Table 4.2: The cuts as performed on the MC data.

distance. In an array with telescopes that are 600 m apart, a core distance of >300 m usually means the shower is observed by more than one telescope and can therefore be more precisely reconstructed by the stereoscopic method. To predict the gamma-hadron rejection quality for the methods employed on a single telescope, the far away showers are not necessary and can be cut away.

The last cut employed is a cut on minimum energy. Low-energy showers show larger relative fluctuations in image width than high-energy showers. The number of e^\pm in a shower determines the amount and distribution of light. In proton showers this number depends on the amount of neutral pions produced, which is in turn much smaller than the amount of e^\pm of a gamma shower. A smaller possible number of pions results in a large relative fluctuation in their number and subsequently in the number of e^\pm and the amount of light. This is especially true for low-energy showers, where pions can be as few as a hundred.

The larger fluctuation in image width causes the respective distributions to spread out and overlap even more. Since the low-energy showers are dominant in number, this heavily reduces the resulting quality factor.

A way to avoid this is to reject all showers below HiSCORE's energy threshold of about 20 TeV, below which HiSCORE can hardly reconstruct the core position with necessary precision and therefore the classical combination is not possible.

A summary of the employed cuts is found in table 4.2. The result of the cuts can be seen in figure 4.23. The quality factor increases from 1.3 to 1.95 just by rejecting incomplete or insignificant events.

Scaling: To further improve the gamma hadron separation, each showers' width can be scaled to the expectancy value for a gamma shower at that respective distance, size, and zenith angle.

For the first studies, a lookup-table was generated from $1.04 \cdot 10^6$ gamma-only showers of 0.5-500 TeV from the zenith for various core distances (see table 4.1).

This lookup-table is shown in figure 4.24 and contains the MC-generated image width expectancy values for gamma showers for the respective core distances and sizes.

4.2. METHODS AND RESULTS

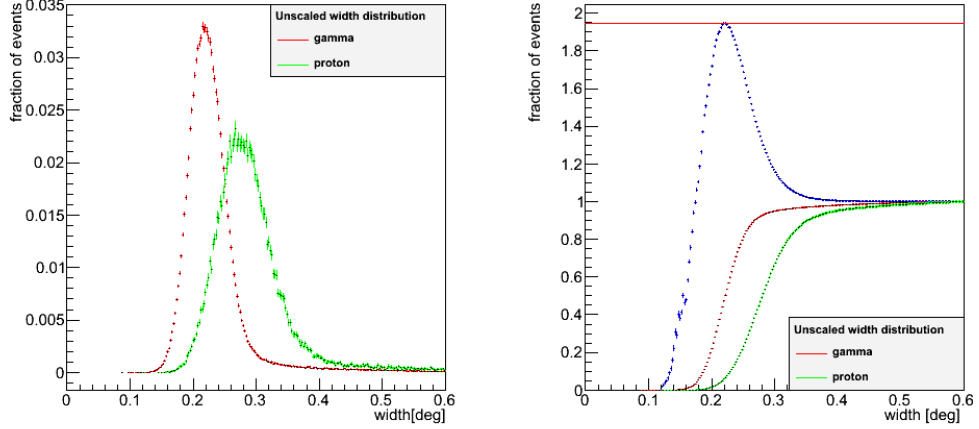


Figure 4.23: Unscaled image width distribution for a TAIGA telescope for showers from the zenith with the cuts listed in table 4.2. Left: differential, right: cumulative distribution. Red: gammas, green: protons. The two distributions overlap strongly. The blue line denotes the quality factor Q if a width cut is performed at the respective value, with a maximum of about 1.95.

In this lookup-table, one can see typical behaviour of shower images: For small core distances, the image width changes with the image size. For a fixed core distance, a larger image size means a brighter shower of larger energy, and the brighter the shower, the more pixels contain enough signal to not be rejected by image cleaning. Therefore the image width increases, as emphasised by figure 4.25 on the left, which shows the profile at 100 m core distance.

An interesting feature that can be seen in the lookup table is directly correlated with the LDF. At a core distance of about 100-120 m, the image width narrows down compared to smaller or larger core distances, as is shown for a size of 2.5 in figure 4.25 on the right, marked by the left yellow line. This is a consequence of the change in Cherenkov angle with changing altitude: At this core distance, the brightness of the center part of the shower is amplified compared to the outer parts because the angle by which the telescope looks at the shower is ideal for the center, but less perfect for the particles with more transversal momentum. The amplification of the center of the signal shrinks the second moment of the signal distribution, and so the image width appears smaller than for larger or smaller core distances.

For core distances larger than 250 m, as seen in figure 4.25 on the right marked by the right yellow line, the image width stays more or less constant, even though the shrinking of the LDF with core distance reduces the amount

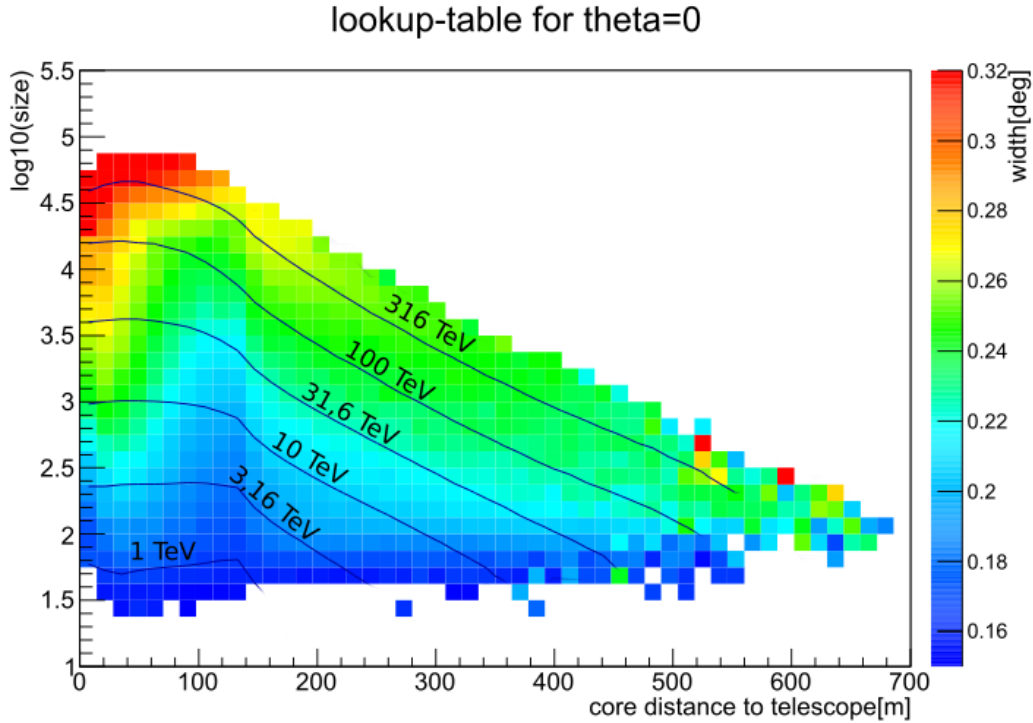


Figure 4.24: Two-dimensional lookup table for scaling of the IACT's image width for a zenith angle of 0° . This lookup-table is generated from the image widths of a separate set of gamma-only showers.

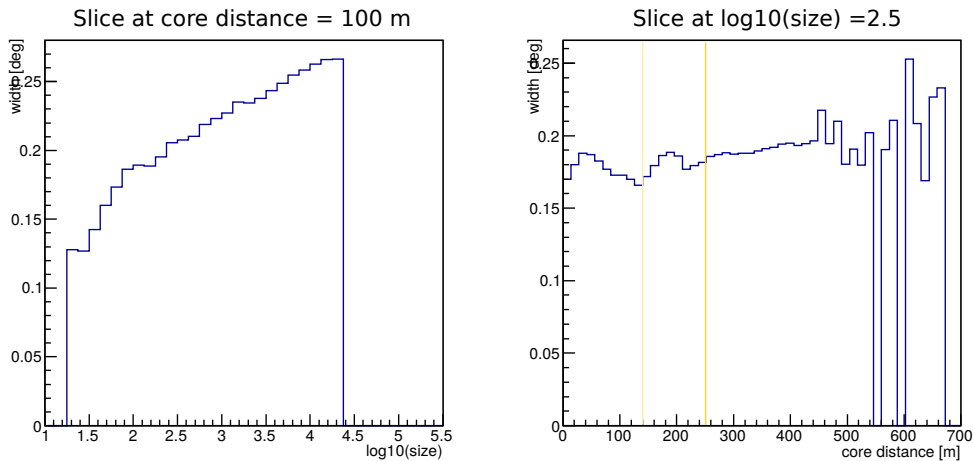


Figure 4.25: Lookup-table profiles for 100 m (left) and at $\log_{10}(\text{size}) = 2.5$ (right). While the image width rises continuously with size, it shows a local minimum at about 120 m (marked in yellow) before rising again. Dips at large core distances are the result of the low statistics, where there are no events in these bins.

4.2. METHODS AND RESULTS

of light reaching the outermost parts of the array. Only the brightest showers are intense enough to still trigger the telescope.

The fluctuations at the largest core distances are an artefact of the reduced statistics at these distances. Many showers beyond 600 m get rejected by a nominal distance cut because of truncation at the camera edge, and thus the outermost bins only contain very few events.

To scale an event’s width to their respective expectancy value, the correct bin in the lookup table needs to be selected. To emulate a core position reconstruction by the HiSCORE array, the MC-known, “true” core position of the shower is randomised with the HiSCORE position reconstruction resolution. This resolution is energy-dependent due to the resulting multiplicity of the stations. The more stations contain signal, the more accurate the reconstruction is, and the higher the energy, the more HiSCORE stations have a signal. The detailed description of the energy dependence can be found in [38].

The hybrid scaled width (HSCW) is defined as

$$W_{\text{HWSQ}} = \frac{w_{\text{image}}(\textit{size}, d_{\text{core HiSCORE}})}{w_{\text{MC}}(\textit{size}, d_{\text{MC}})} \quad (4.10)$$

with $w_{\text{image}}(\textit{size}, d_{\text{core HiSCORE}})$ the image width of the individual image dependent on image size and HiSCORE-reconstructed core distance and $w_{\text{MC}}(\textit{size}, d_{\text{MC}})$ the respective MC-generated expectancy value for a gamma shower of the same size and core distance.

The scaled distribution can be seen in figure 4.26. Scaling the width makes the distributions of protons and gammas move apart, and now a cut on the HSCW yields a quality factor of approximately 2.7, which is not only better than an unscaled cut, but also better than the HiSCORE-only separation at lower energies. The timing array barely achieves a Q of 1 at the threshold of a few TeV and only starts to approach 2 at a hundred TeV [38]. The blurring of the core position lowers the separation quality only little compared to the direct use of the MC core position (≈ 2.8) despite HiSCORE’s energy dependency in reconstruction quality.

The plots shown thus far are the overall quality factor integrated over all core distances and for all energies above 20 TeV. The bin-wise dependencies to these two observables were explored in figure 4.27, where the dependency of the quality factor on the core distance for different energy bins and on the energy for different core distances are shown in their respective diagrams.

Figure 4.27b illustrates again why a cut on a minimum energy is sensible when evaluating a hybrid reconstruction for a combined TAIGA array.

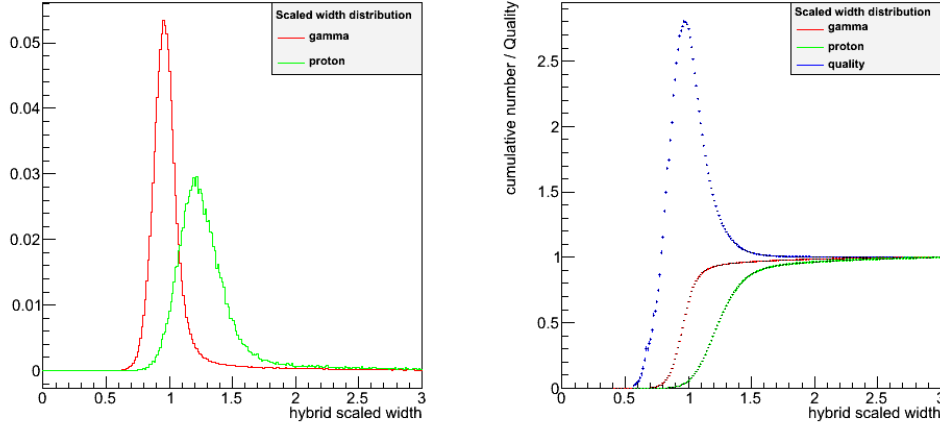


Figure 4.26: HSCW distribution for a TAIGA telescope for showers from the zenith, left: differential, right: cumulative. Red: gammas, green: protons. The two distributions have moved apart as compared to the unscaled distribution (figure 4.23). The blue line denotes the quality factor Q if a width cut is performed at the respective value. The cut quality factor rises to almost 2.7.

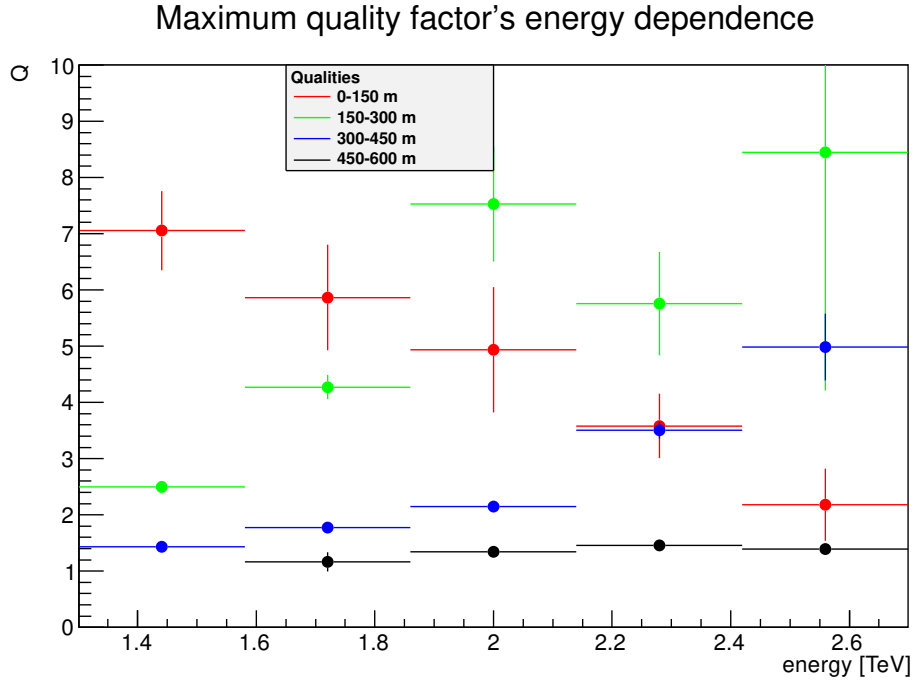
The gamma-hadron separation quality for low energy showers is, while large at small core distances, always inferior at core distances above 150 m when compared to higher energies. Since low energy showers are typically more numerous and most showers are detected beyond 100 m, the weight of numbers brings down the integrated quality factor drastically, even though on first glance it looks like the overall quality could be better than 2.7.

At close range (0-150 m), the separation quality is best for lower energy showers. Showers at about 100 TeV are best observed at medium range (150-300 m), with showers above 300 TeV best seen at about 300 m. Beyond 400 m, the separation quality is between 2 and 1 for all energies, due to an effect that is described a little further on in this thesis.

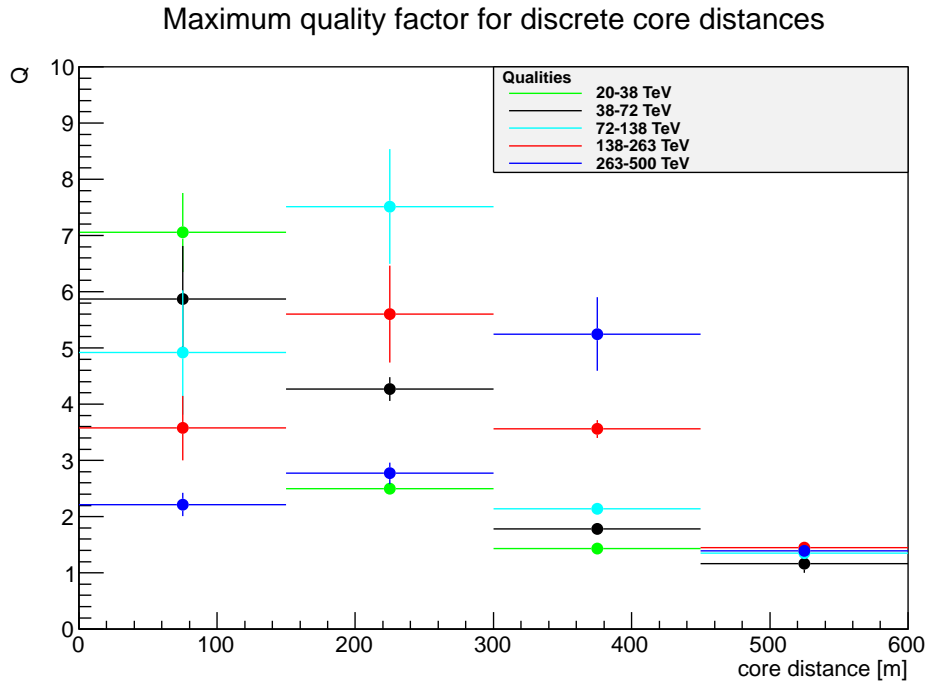
In the center, the particles of a gamma shower are strongly beamed along the shower axis and therefore to the shower center, while the particle distribution in a proton shower is more even, but irregular. With increasing energy, the relative fluctuations in a shower decline due to the large number of resulting secondaries. This lessens the irregularity in the proton images, which in turn reduces the possible separation quality at small core distances.

On the other hand, at large core distances, a higher energy is beneficial to the quality. The light arriving at large core distances originates from particles with large transversal momenta, which typically are more numerous in proton showers. Also, a higher energy raises the probability of sub-cascades with

4.2. METHODS AND RESULTS



(a) vs. energy



(b) vs. core

Figure 4.27: Maximum quality factor dependence on different energies and core distances for a HSCW distribution, binwise.

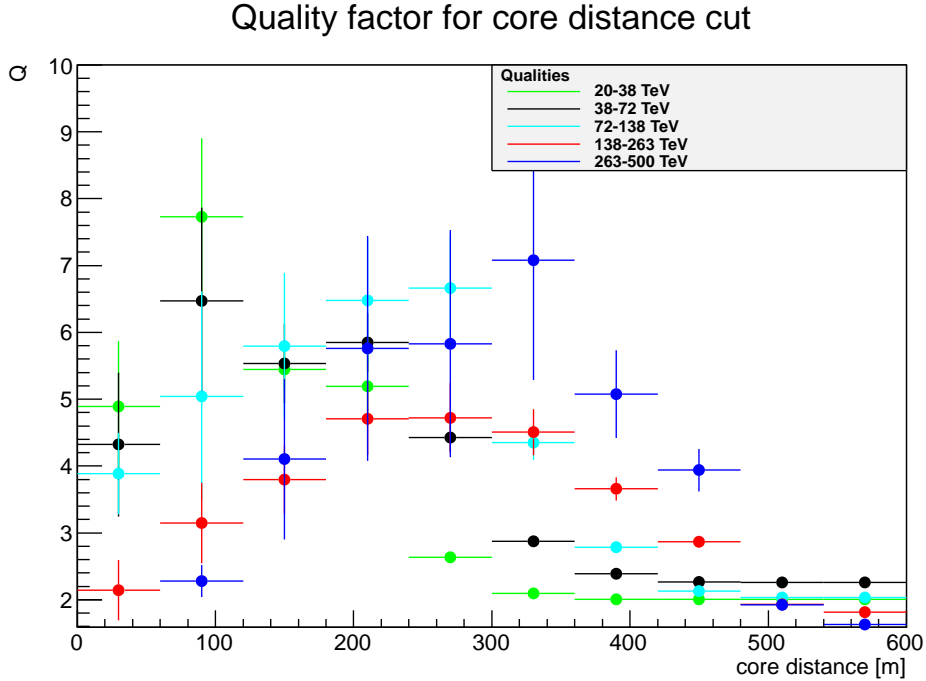


Figure 4.28: Quality of the HSCW method for different core distance cuts for different energy bins.

small off-axis angles. This makes proton showers appear even wider than gamma showers of the same size, who still appear slim due to the beaming.

While figure 4.27a shows the separation power for certain core distance bins (for example 150 m - 300 m), figure 4.28 shows the maximum possible quality factor for different core distance cuts, containing all showers from 0 m to the respective value. It can be seen that the "sweet spot" where most energies find their optimum quality lie at core distances smaller than 300 m, at least for showers from the zenith. It therefore suggests itself to constrain the core distance cut a little further down to 250 m.

Figure 4.29 shows the resulting energy-integrated distributions for core distances of less than 250 m. Both gamma and proton distributions have narrowed down drastically and the resulting overall quality factor with a value of 4.6 almost doubles itself in comparison to the distribution with the 300 m core distance limit shown in figure 4.28.

250 m is the distance at which the expected width changes its behaviour. With smaller core distances, the expected width changes, while, as mentioned before, above 250 m the expected width starts remaining constant (figure 4.25, right). This constancy renders the scaling process inefficient at these

4.2. METHODS AND RESULTS

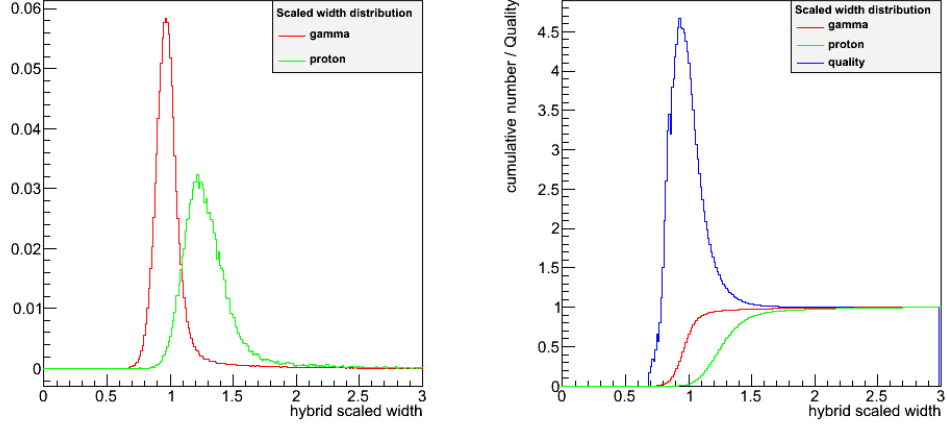


Figure 4.29: HSCW distribution for a TAIGA telescope for showers from the zenith for the cuts listed in table 4.2 and a tightened core distance cut of 250 m. Left: differential, right: cumulative. Red: gammas, green: protons. Both distributions have slimmed down drastically compared to figure 4.26. The blue line denotes the quality factor Q if a width cut is performed at the respective value. The cut quality factor rises to 4.6.

distances as scaling by a constant value does not change the shape of any distribution.

The Tur Tur effect, and viewing directions

A constant image width with increasing core distance means that the emitting region of the shower appears wider the farther away the observer is from the shower. This Tur Tur effect (named after Tur Tur, the illusory giant from the novel *Jim Knopf und Lukas der Lokomotivführer*, who appears larger the farther he is away [1]) is responsible for the inefficiency of the width scaling at core distances beyond 250 m.

The only light that reaches a telescope beyond 150 m is light from shower particles that have already scattered multiple times. One would expect that telescopes that are far away from the core impact position only see the low-most part of the shower, where the multiple scattering is the strongest and shower cone is relatively wide, and that this behaviour would compensate for the geometric loss of width by distance.

However, the distribution of the emission heights shown in figure 4.30 disproves this. The average emission height of the photons arriving at a certain core distance does not shrink with increasing core distance, but stays

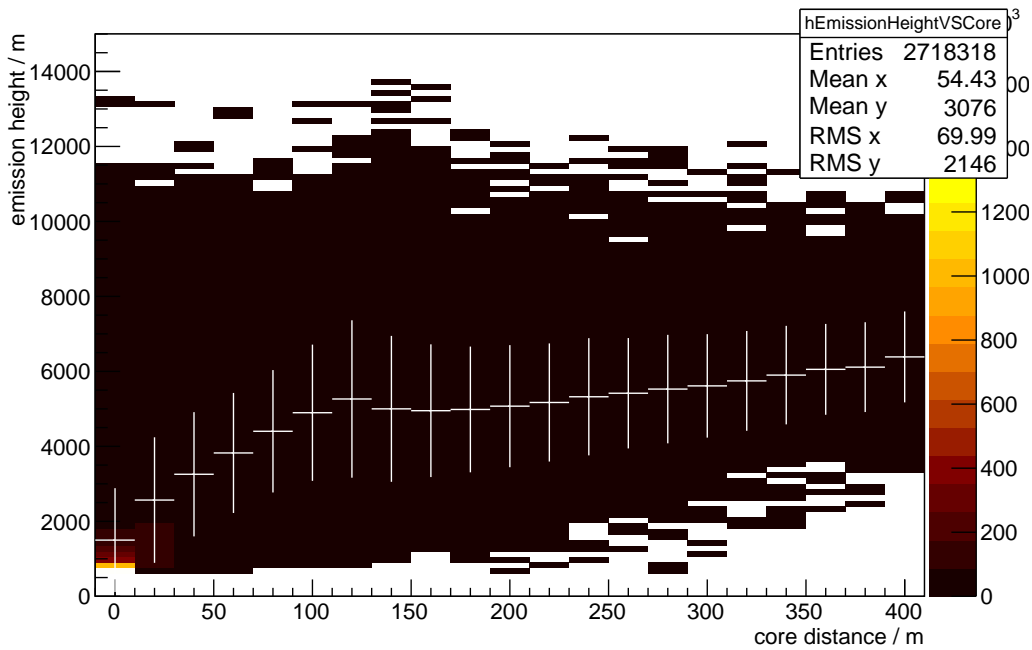


Figure 4.30: The average emission height for photons against the core distance they were detected at, for a gamma shower of 100 TeV, with a photon angle acceptance cut of 5° to represent the acceptance of an IACT. The average emission height is low for core distances smaller than 120 m and stays more or less constant for core distances beyond. Plot courtesy of D. Horns, M. Tluczykont, M. Kunnas, paper in preparation.

4.2. METHODS AND RESULTS

rather constant at the shower maximum for all distances beyond 120 m, even starting to rise again beyond 150 m. For core distances beyond 250 m, not only the average, but also the minimum emission altitude starts to rise, with no photons emitted lower than 3800 m for a core distance of 350 m.

On the other hand, at the very center of the shower the observer mainly receives light that was emitted right before the shower reaches the ground, from altitudes considerably lower than the maximum. This makes the shower appear closer to the observer, which should increase rather than decrease the detected shower width.

Obviously, the emission height alone is not the responsible factor for the constancy of the observed image with beyond 250 m core distance and the resulting deterioration of the gamma hadron separation at larger core distances.

The origin and impact of the Tur Tur effect can best be seen in figure 4.31, where the average distance from the shower axis at which the Cherenkov photons were emitted is plotted against the core distance they were detected at for a gamma shower of 100 TeV from the zenith. At the center of the shower, the extension of the emitting region is more or less constant at approximately 10 m. The main part of the particles at this distance possess a high kinetic energy at the time of Cherenkov emission, which reduces the amount of deflection and scattering.

Beyond 120 m, the average emission distance from the shower axis increases with the core distance, meaning that the observed transversal extension of the shower widens - the shower appears larger from farther away.

At these distances, the Cherenkov angle of an emitting particle alone is not enough to give a photon the necessary off-axis angle to reach the respective lateral distance to the shower center on ground level. The emitting particle itself needs to have a sufficiently large transversal momentum, which in a gamma shower can only be achieved by multiple scattering. Therefore, the Cherenkov photons detected at core distances beyond 120 m must have been emitted by low energy particles, which in turn must be the most abundant at a distance of more than 10 m from the shower axis and at the shower maximum (see figure 4.30) to cause the Tur Tur effect as we see it.

A prominent feature in this plot is the fact that for core distances beyond the core region, even a gamma shower is not rotationally symmetrical around its axis. The extension of the emitting region depends on the alignment of the shower towards Earth's magnetic field, a fact commonly omitted from considerations as most telescope arrays in operation only consider close showers due to their need for stereoscopy. For small core distances, the high kinetic energy suppresses the deflection on the Earth's magnetic field.

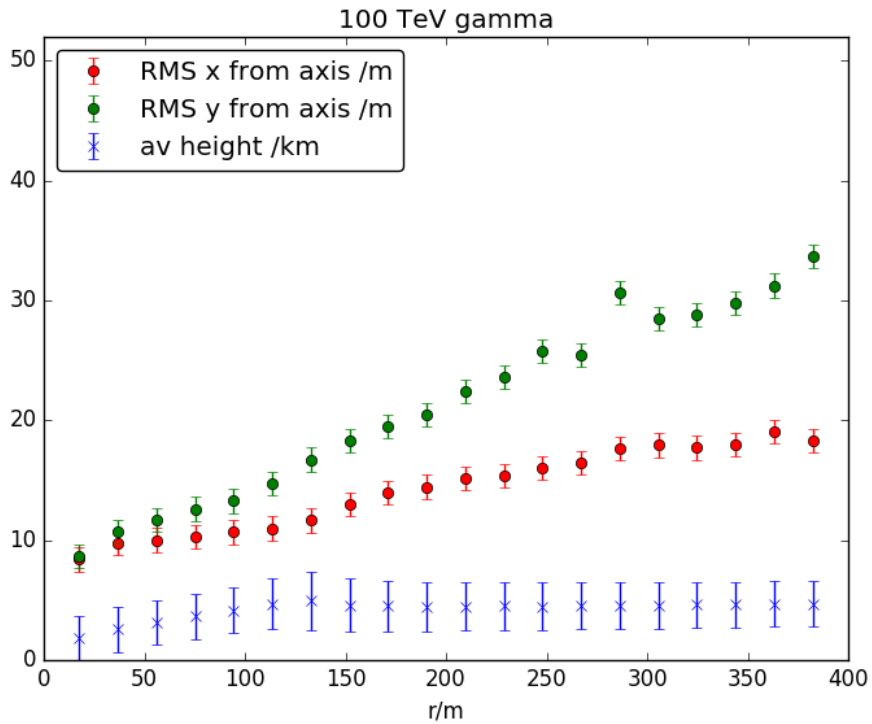


Figure 4.31: The average distance of the emission point of the Cherenkov photons from the shower axis against the core distance they were detected at, for a gamma shower of 100 TeV from the zenith and for the two ground directions: The red line denotes the extension of the shower in north-south direction, parallel to Earth's magnetic field lines, and the green points show the extension perpendicular to the magnetic field. The blue bars show the average emission height. It can be seen that the visible shower is wider for larger core distances, and for core distances beyond 120 m, the magnetic field strongly impacts the extension of the emitting region. Plot courtesy of D. Horns, M. Tluczykont, M. Kunnas, paper in preparation.

4.2. METHODS AND RESULTS

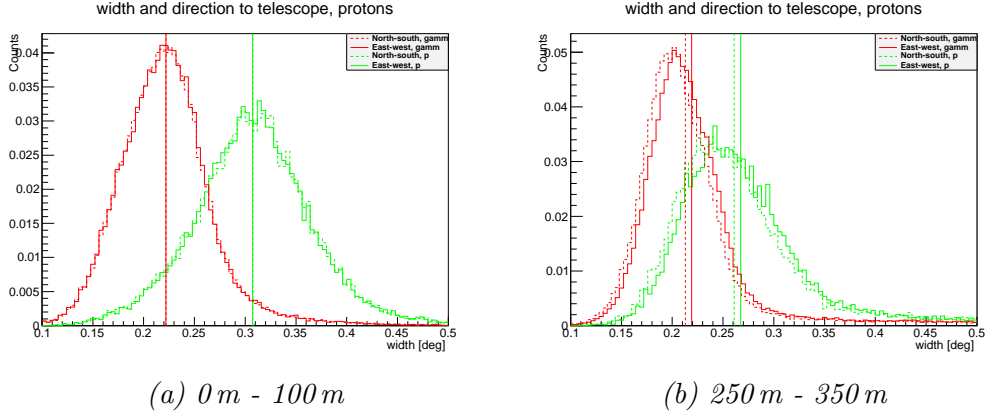


Figure 4.32: Distribution of image widths for gamma (red) and proton (green) showers at different core distances, depending on the direction from which the shower is seen by the telescope. The dashed line denotes the widths seen for showers that lie north or south from the detecting telescope, the solid line are showers that impact westward or eastward from the telescope. For close core distances (left), there is no difference between the resulting distributions, while the asymmetry due to deflection of the charged particles in the magnetic field of Earth is clearly visible at larger distances (right).

The low-energy component of the shower that is responsible for the light detected at large core distances is also the most susceptible to deflection by magnetic fields. This low energy component is not only the most abundant at the outer parts of the shower, but also causes the east-west extension of the shower to be larger than the north-south extension, as the deflection is perpendicular to the Earth’s magnetic field.

The dependence of the shower width from the observation direction is observable also in the IACT images. Figure 4.32 shows the image width distribution dependent on the direction under which the shower is observed. The behaviour is as would be expected from figure 4.31: At close distances (figure 4.32a), the distributions do not show a significant difference, while larger core distances (figure 4.32b) show a distinctive difference between showers seen in east-west direction and showers observed in north-south direction. The total difference amounts to approximately 0.01° , which is about 10% of the full width half maximum of the gamma shower distribution. It stands to note that the absolute difference between the viewing directions seems to be the same for both types of shower primaries; as the energy distribution of the particles in the shower at emission time (i.e. the shower maximum) is similar, then of course the amount by which the magnetic field deflects the particles is almost independent of any initial transversal momentum the

particles may have received higher up in the atmosphere.

The difference in width with viewing direction is dependent on the cosine of the angle between north direction, shower maximum and observer. Including this angle into the scaling process might improve the quality of the MSCW cut as the expectancy values in the lookup table can be determined more precisely, since in the current approach the widths are averaged over all azimuthal viewing directions. This proposition however could not be followed in the scope of this thesis and will be subject to further studies at a later time.

Conclusion: The simulation with the emulated HiSCORE core position reconstruction shows that the TAIGA IACT design is adequate for its intended purpose. The PSF stays small enough to not oversample the showers even for large off-axis angles and given setup inaccuracies.

The effective area shows an optimal usage of space in a 600 m x 600 m telescope grid at trigger level, and the system can provide a viable gamma-hadron separation near the energy threshold of HiSCORE, where the timing array cannot separate.

On the other hand, the simulations suggest that the gamma-hadron separation and therefore the sensitivity can be further improved by the factor of 1.7 by reducing the distance between the telescopes to 500 m, so that the maximum distance at which a telescope sees a shower monoscopically is always smaller than 250 m.

4.3 Optimisation of pixel size 1

The width of the IACT camera image is the most important parameter for gamma hadron separation by IACT. On one hand, it is desirable to have a fine resolution to be able to determine the image width as precisely as possible. On the other hand, each pixel increases the cost of the telescope, so it is also desirable to cover the field of view with as few pixels as possible. Thus, a big challenge in telescope design is to find the optimum balance between width precision and pixel size.

The question of optimum pixel size was studied in two different ways in the course of this thesis: by `sim_telarray` MC simulation, described in this section, and by analytical description to be found in section 5.2.

A combination of pixels

To simulate various cameras with different pixel sizes with the classic `sim_telarray` code, it would be necessary to define a camera file for every camera of interest and then run the full simulation for each one of them. Especially for fine cameras with a high number of pixels, this method is demanding on machine memory and computing time.

To cut on the simulation time, a pixel combination algorithm was implemented into a copy of the `read_hess` code. This method starts from a `sim_telarray` simulation of a telescope with the finest camera possible. The maximum number of pixels in a camera is limited by the memory of the machine used for the simulation, and was found to be 16 000 for this thesis.

The modified `read_hess` code takes the pixel-specific x and y positions and the amplitude of the pixels to combine respective neighbours into macropixels as illustrated in figure 4.33. The size of the macropixels is determined by the amount of pixels combined, with the smallest macropixel being the sum of seven primary pixels, one ring of pixels around a center hexagonal pixel. The central pixel gives the x/y position of the new macropixel, the radius amounts to $(N + 0.5)r_{\text{pix}}$ with N the amount of rings around the center pixel and r_{pix} the radius of the primary pixel.

The amplitude of a macropixel is the sum of its members' amplitudes, NSB noise, pedestals and tailcuts are scaled with the area of the macropixel. Macropixels that do not get the full amount of members are rejected since keeping the incomplete pixels would create inconsistencies, especially concerning noise and possible pixel shape effects.

After combining the pixels, the `read_hess` code continues as normal, performing a Hillas analysis and plotting. An example of resulting images can be seen in figure 4.34.

Again, all simulations were performed under the assumption of a perfect TAIGA IACT.

Results and conclusions

When the pixel's diameter exceeds the shower's width, one would expect a slight increase in observed width. When a macropixel is formed close to the edge of the shower ellipse, micropixels that do not contain enough amplitude to be considered part of the image are summed up with pixels that are, and provided with one new, common set of coordinates. These coordinates most likely lie further outwards from the image COG than the pixels that actually had amplitude, and since the image width is computed as the second moment of the pixel amplitude distribution, the ellipse edge pixels contribute more

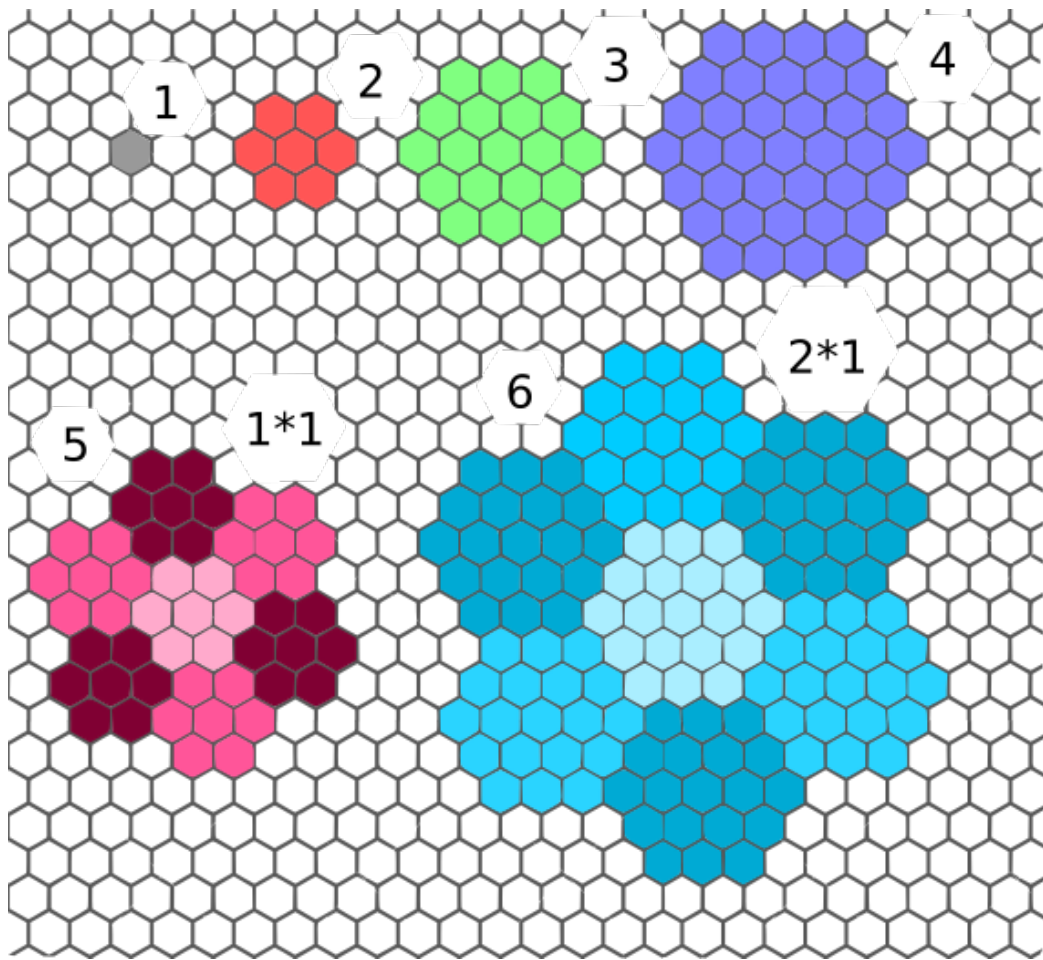


Figure 4.33: Schematic view of how pixels are summed up in the pixel combination process.

4.3. OPTIMISATION OF PIXEL SIZE 1

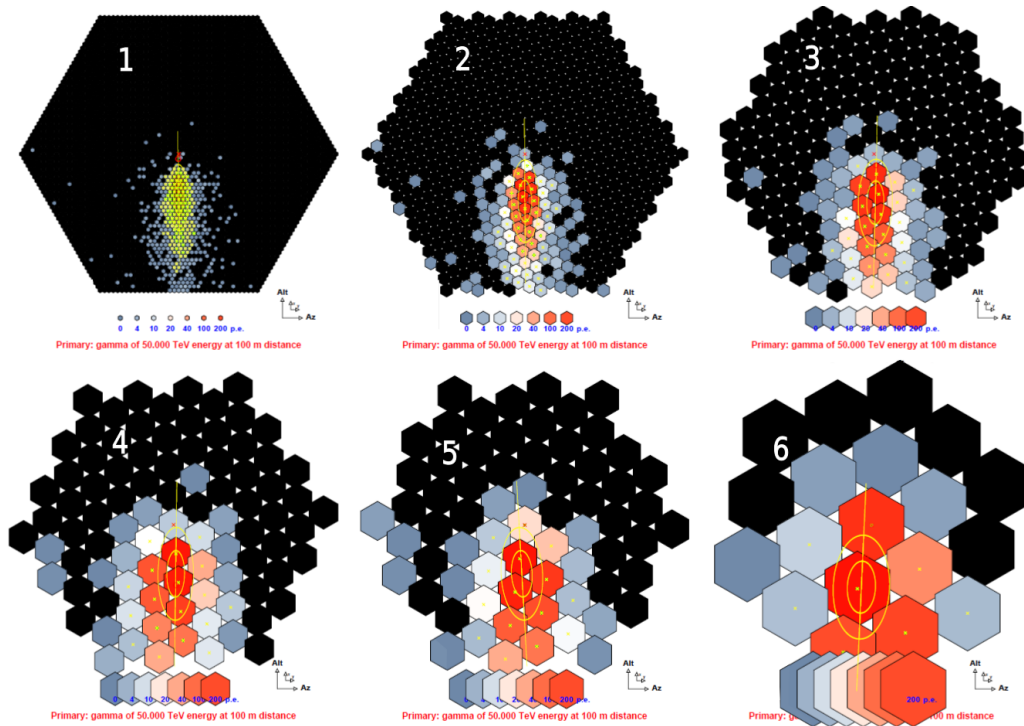


Figure 4.34: Example for resulting images of the pixel combination. 1.) Original image (primary pixels) 2.) 1 ring around center pixel 3.) 2 rings 4.) 3 rings 5.) double combination: combining 1 ring of pixels of 1 ring 6.) 1 ring of 2-ring pixels. Numbers correspond to pixel shapes as shown in figure 4.33. Please note that the x/y scale of the images is not constant for all images, the camera in image 1 has a FoV of 10° while the camera in image 6 hardly reaches a FoV of 5° due to the rejection of incomplete pixels.

4.3. OPTIMISATION OF PIXEL SIZE 1

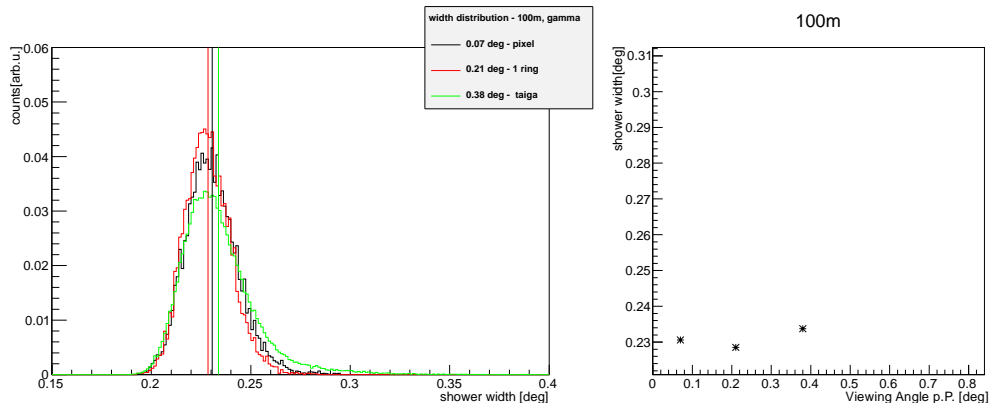


Figure 4.35: Resulting image widths for the high-resolution camera (0.07° per pixel), the first pixel-combination (0.21° per pixel) and the direct TAIGA simulation (0.38° per pixel), for showers of 50 TeV and a core distance of 100 m. The observed image width is almost independent of pixel size. The larger pixel sizes are left out for clarity.

to the image width than before.

The smallest possible pixel size for a camera with a 10° viewing angle is 15769 micropixels with $d_{\text{pix}} = 0.07^\circ$ viewing angle each in 72 rings around the camera center. The resulting image widths for the original pixels, the first combination and the of the original TAIGA simulation can be found in figure 4.35. For the original pixels of 0.07° , the average image width lies at about 0.23° , which agrees well with the image width of approximately 0.235° of the standard TAIGA telescope. Also, the first pixel combination with a macropixel size of 0.21° shares this result. Up to this pixel size, the image width seems to be independent of it, even though the TAIGA pixels are larger than the resulting image width.

The first small differences start to arise at $d_{\text{pix}} = 0.35^\circ$, which is shown in figure 4.36 together with the values for the larger pixels. The resulting image width of 0.24° is larger than the value for the TAIGA design, but the difference is not great enough to disprove this method.

The real problem can be seen for the pixels that were combined twice. Pixels of 0.63° (almost three times the actual image width) show a width of 0.27° . The increase in width is a result of the rejection of incomplete pixels at the edge of the camera. A doubled combination process rejects incomplete pixels twice, which is especially devastating in the second iteration. The rejection shrinks down the camera from about 10° viewing angle to about 5.7° , which in turn truncates the image (check figure 4.34 for illustration) and therefore increases the width. This effect is even worse for the second

4.3. OPTIMISATION OF PIXEL SIZE 1

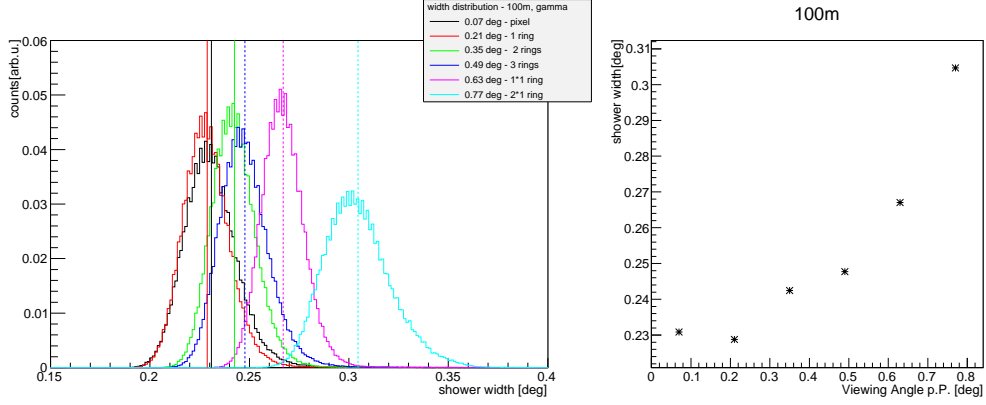


Figure 4.36: Resulting image widths for the high-resolution camera and the pixel-combined images for showers of 50 TeV and a core distance of 100 m. The observed image width increases drastically with pixel size.

double combined pixel set (0.77°), where almost every image is truncated and the width is enormously inflated.

Proof of this truncation can be found in the distribution of the Hillas α angles. Alpha is the angle between camera x-axis and the image ellipse, and for perfect reconstruction in the simulated setup, this angle should be always 0° . A value bigger than 0° indicates that the image axis is rotated corresponding to the nominal axis, an effect that only happens if the outer parts of the image are lost due to rejection or truncation. Such a rotation leads to a misidentification of the positions along which the Hillas parameters are calculated, which artificially increases the width, decreases the length and effectively destroys the gamma-hadron-separation.

Figure 4.37 shows the resulting distribution of α with a clear increase in value with increasing combination number. The combination thus obviously does distort the orientation of the shower axis above the combination of one ring of pixels .

Conclusion: Systematically, combining the pixels can only give a broad overview over the behaviour with different pixel sizes, rather than providing the possibility to examine the pixel sizes freely. Each primary pixel size gives a fixed set of macropixels; for 0.07° we get 0.21° , 0.35° , 0.49° , 0.63° and 0.77° . The pixels size increases steeply by adding $2 \cdot r_{\text{pix}}$ each combination step, and already the third combination step reaches a pixel size that is larger than the actual width of the shower image.

While the smaller pixels imply that the image width might be almost independent of the pixel size, the pixel combination method is not an appro-

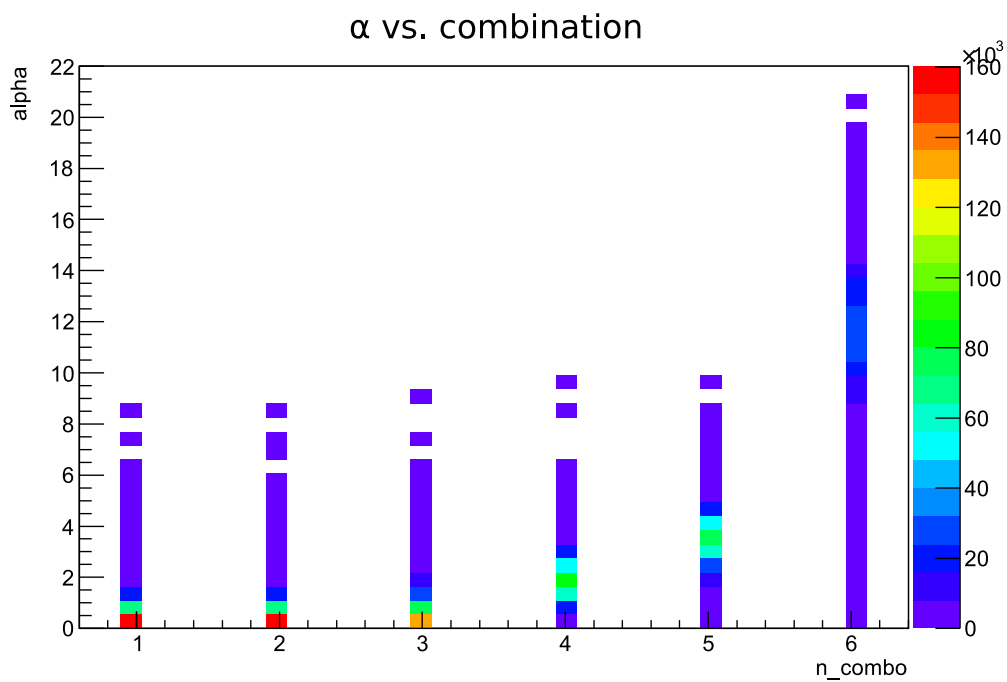


Figure 4.37: Resulting angles between camera x -axis and image ellipse main axis, dependent on the number of combined pixels. Enumeration as in figure 4.33. The increase in α is a definitive sign of misreconstruction due to truncation of the image at the camera's edge.

4.3. OPTIMISATION OF PIXEL SIZE 1

priate tool to evaluate this statement. The effects of truncation due to the rejection of incomplete pixels are too severe to form appropriate conclusions. The truncation could be reduced by a more careful choice of which pixels are summed up together as macropixels, but could not be fully avoided. Increasing the overall size of the camera to more than 10° to compensate for the rejected edges could prevent the truncation of the image, but the amount of computation time and memory needed increases with the square of the camera radius. The smallest pixels simulated were already chosen as the highest number of pixels which are possible to simulate with the given hardware.

Instead, a different method was to be chosen, a semi-analytic modelling of the shower itself, which will be discussed in the following chapter.

Chapter 5

Semi-analytical study

All processes inside a detector simulation like `sim_telarray` are tracked and recorded, which generates a large volume of data, and the results require a large number of data sets to be sufficiently precise, which in turn amounts to large computing time. Also, these computations need to be re-done every time something changes in the model or the detector, for example the number of mirrors in the telescope dish or the presumed observation level. Especially the number of pixels in the camera increases the computation time and memory usage of `sim_telarray` and `read_hess` drastically.

Calculating the number of photons arriving at a camera analytically to obtain image parameters like image width is a time-efficient alternative to individually tracking millions of particles and photons. A purely analytic model does not give any statement on the shower-to-shower fluctuations, so a semi-analytic approach was chosen to study the behaviour of the image with changing telescope parameters.

The studies presented here examine the change of the image width with pixel size, give an estimation about the quality factor of a width cut of this model and assess whether or not a shower can be detected by a high-resolution CMOS camera.

5.1 The model

To make a statement about resulting camera images, one must first perform a pixel-wise calculation of the possible amplitude.

The model used to predict the number of Cherenkov photons arriving at a camera pixel from a gamma shower was devised by M. Lemoine-Goumard, B. Degrange, and M. Tluczykont (2006, [56]) as part of a new reconstruction algorithm for the HESS experiment. The base of this model is the assumption

5.1. THE MODEL

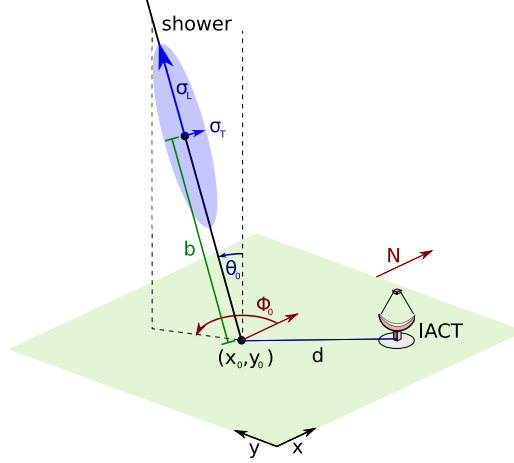


Figure 5.1: Parameters used in the analytic calculation of the expected number of arriving photons in a pixel. d : distance between shower core and telescope, σ_L and σ_T : length and width of the 3D ellipsoid, b : height of the ellipsoid's barycenter, θ_0 : shower zenith angle, Φ_0 : shower azimuth angle, (x_0, y_0) : shower core coordinates, N : north direction.

that the emitting region of the shower can be considered a 3D Gaussian ellipsoid, rotationally symmetric around the shower axis (for visualisation, see figure 5.1). The ellipse is parametrised by the position of the barycenter B on the shower axis, which corresponds to the shower maximum, with the barycenter height h the distance between impact point and barycenter on the shower axis; the polar angles θ_0 and ϕ_0 giving the incidence direction of the shower axis; the core impact position (x_0, y_0) ; the 3D-length and twofold degenerate 3D-width σ_L and σ_T , which are the longitudinal and transversal standard deviations of the Gaussian ellipse; and the total number of photons in the shower N_c , which is mainly energy dependent [57]:

$$N_c(E) = 4.5 \cdot 10^{10} \cdot \frac{E[\text{eV}]}{10^{15} \text{eV}} = 45 \frac{E}{\text{MeV}} \quad (5.1)$$

The approximation of a shower as a 3D ellipse seems counter-intuitive at first, as the distance a shower traverses before reaching its maximum is far greater than the distance after the maximum. However, the number of electrons and positrons at high altitudes (>12000 m) is small and only contributes a few percent of the total amount of light. Lemoine-Goumard et al. came to the conclusion that the average 3D length is about 3000 m and almost independent of primary energy [56].

In principle, approximating the transversal distribution as Gaussian is

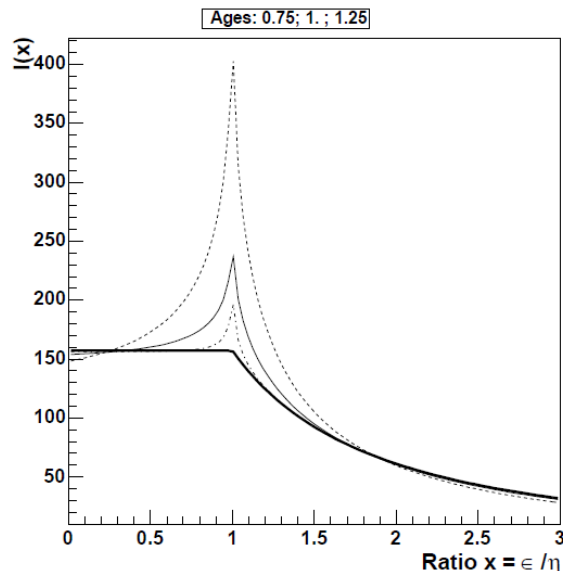


Figure 5.2: Cherenkov photon emission distribution per unit solid angle for different angles ϵ relative to the shower axis for different shower development stages (shower ages 0.75, 1.0, 1.25) and an energy of 0.5-1 TeV. The parameter η is the maximum Cherenkov angle at the respective altitude. In normalised form, the bold line describes the $I(\epsilon)$ used in the analytical model. Plot taken from [56].

inaccurate, as a shower's transversal distribution is far more peaked in the center than a gaussian profile. However, the typical gamma 3D-width of 10-15 m, viewed at a distance of 8-10 km, corresponds to a viewing angle of about 15 mrad (0.004°). So as long as the pixels of the camera stay larger than this measure, a finer description of the shower center is not needed and a Gaussian can be used as an approximation.

Another simplification is the assumption that the angular distribution of Cherenkov photons relative to the shower axis is independent of primary energy and the emitting region's position with respect to the shower axis. Instead, the emission probability $I(\epsilon)$ for a direction is dependent on the factor $x = \epsilon/\eta$, with the angle ϵ between the shower axis and the direction divided by the respective altitude's maximum Cherenkov angle η . The probability distribution for different shower ages (i.e., different development stages of the shower, with an age of 1 denoting the shower maximum) can be seen in figure 5.2.

After asserting that the peak at $x = 1$ that a real shower would have does not contribute much to the accuracy of the model, Lemoine-Gourmard et al parametrise $I(\epsilon)$ down to

5.1. THE MODEL

$$I(\epsilon) = K \text{ for } \epsilon < \eta$$

$$I(\epsilon) = K \frac{\eta}{\epsilon} \left[-\frac{\epsilon - \eta}{4\eta} \right] \text{ for } \epsilon > \eta \quad (5.2)$$

With $K = 1/(9\pi\eta^2)$ being the normalisation obtained from $\int I(\epsilon)d\Omega = 1$.

Further fits performed by Lemoine-Gourmard et al proved that using an altitude and energy independent value for η was sufficiently accurate, so that only the zenith angle ζ dependency of the Cherenkov angle η remains

$$\eta = 15 \text{ mrad} \cdot \sqrt{\cos\zeta}. \quad (5.3)$$

Usable for an atmosphere whose density is assumed to decrease exponentially with altitude.

The fraction of Cherenkov photons reaching the mirror of an area S_{tel} from an emission point E to reach the pixel of interest is given by the emission probability $I(\epsilon)$ and the solid angle under which the mirror is viewed from the emission point, $d\Omega = S_{\text{tel}} \cdot \cos(\theta) / r^2$, with θ being the angle between the telescope axis and the line of sight of the pixel.

The amount of collected photons is the integral over the line of sight of the Cherenkov photon density $n_c(r)$ in the volume $r^2 dr \Delta\omega_{\text{pix}}$ at the distance r along the line of sight, with $\Delta\omega_{\text{pix}}$ the solid angle seen by the pixel. From this, the amount of Cherenkov photons arriving at a pixel amounts to:

$$\begin{aligned} q_{\text{th}} &= \int_0^\infty N_c(r) r^2 dr \Delta\omega_{\text{pix}} I(\epsilon) \frac{S_{\text{tel}} \cos(\theta)}{r^2} \\ &= S_{\text{tel}} \Delta\omega_{\text{pix}} I(\epsilon) \cos(\theta) \int_0^\infty N_c(r) dr \end{aligned} \quad (5.4)$$

This formula, implemented into a code called *ana_sol* in the frame of this thesis, allows to calculate the expected number of incoming Cherenkov photons per pixel for cameras of various pixel numbers, layouts and sizes. The camera images generated this way, like the ones shown in figure 5.3, are subsequently evaluated by a standard Hillas analysis and can be interpreted as a gamma shower seen by a camera with 100% efficiency.

This 3D model was developed and optimised for gamma showers. Proton showers are only described inadequately; as no 3D model of proton showers exists, proton showers are assumed to be gamma showers with a far larger 3D width.

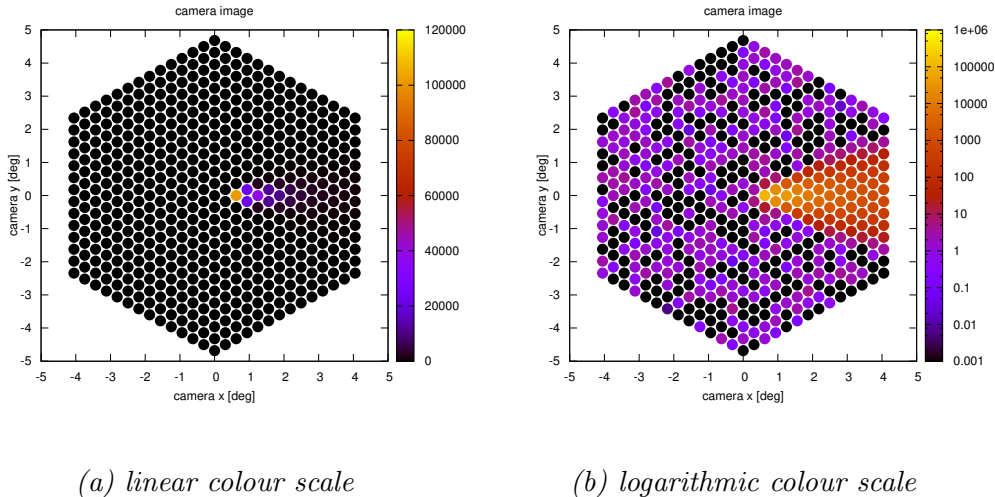


Figure 5.3: Example of an image produced with formula 5.4 for a shower of 50 TeV and the TAIGA IACT configuration, in units of arriving photons per pixel.

Values with randomised components and dependencies

Certain aspects of a shower are subject to the distinctive shower to shower fluctuations that shape the image width distributions of gamma and proton showers. To adequately reproduce these distributions, the analytic equations mentioned above need to be fed with parameters that match the natural fluctuations as good as possible.

The height of the shower maximum, represented by the barycenter of the 3D ellipse, depends on the energy of the primary. The base energy-dependent depth of the shower maximum is calculated via equation 2.3, this base depth is then randomised by one radiation length ($37.1 \text{ g}\cdot\text{cm}^{-2}$) in air for gammas or one mean free path ($80 \text{ g}\cdot\text{cm}^{-2}$) for protons. The resulting barycenter depth is then converted to meters above ground using density values taken from the International Standard Atmosphere table [58].

The value that has the strongest impact on the resulting image width is, of course, the actual width of the 3D ellipse, σ_T . This width is a portrayal of the transversal momenta that are prevalent in the shower. Figure 5.4a shows the distribution of σ_T for gamma and proton showers as reconstructed from real observational data by the authors of [56]. This distribution has been used as a template and implemented into the ana_sol code by inversion, the resulting algorithms reproduce this distribution well (seen in figure 5.4b).

5.2. GENERAL BEHAVIOUR OF IMAGE WIDTH AND QUALITY FACTOR

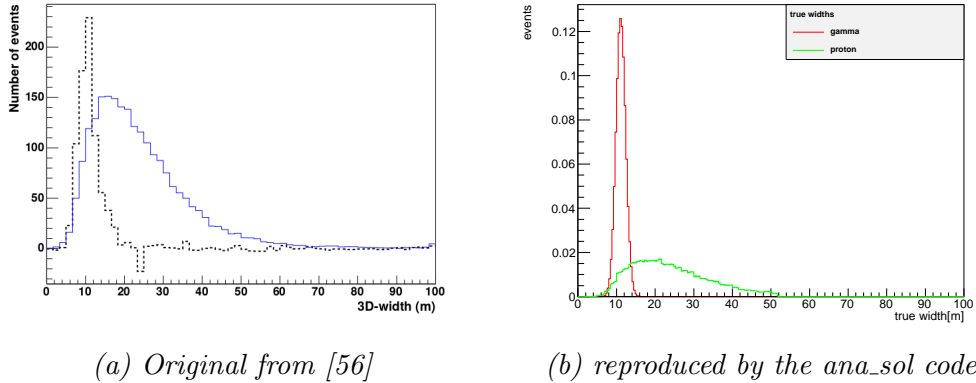


Figure 5.4: Distribution of the ellipse widths σ_T for gamma and proton showers. Left: σ_T as determined by [56] by reconstruction of actual shower data; right: reproduction of the distribution to the left by `ana_sol`, normalised.

The NSB is approximated by adding a small randomised amount of extra photons to each pixel, depending on pixel size and estimation of background.

Any contributions of electronics, imperfect mirror alignment and telescope PSF are omitted as we assume optimal conditions.

5.2 General behaviour of image width and quality factor

Studying the behaviour of the Hillas-type image with pixel size to determine the optimum balance between resolution and cost is cumbersome to perform with MC simulation. Using the analytic approach allows to examine the behaviour more closely, especially in the range of 0.1° - 0.6° where the typical IACT pixel sizes lie.

Figure 5.5 shows the behaviour of the analytical image width of gamma showers of 100 TeV at a core distance of 100 m with varying pixel size. The resulting image widths lie very close together and show a tendency that larger pixel sizes result in smaller image widths, even though the correlation is not very strong.

The deviation from a strict correlation can be explained by the orientation of the image inside the camera: The direction between shower core and telescope is always the same in this data set, with only the core distance being varied, so the image always sits on the very same location in the camera. The exact number and position of pixels hit by the light thus only depends on the size of the pixels, and the threshold line between pixels above and below

5.2. GENERAL BEHAVIOUR OF IMAGE WIDTH AND QUALITY FACTOR

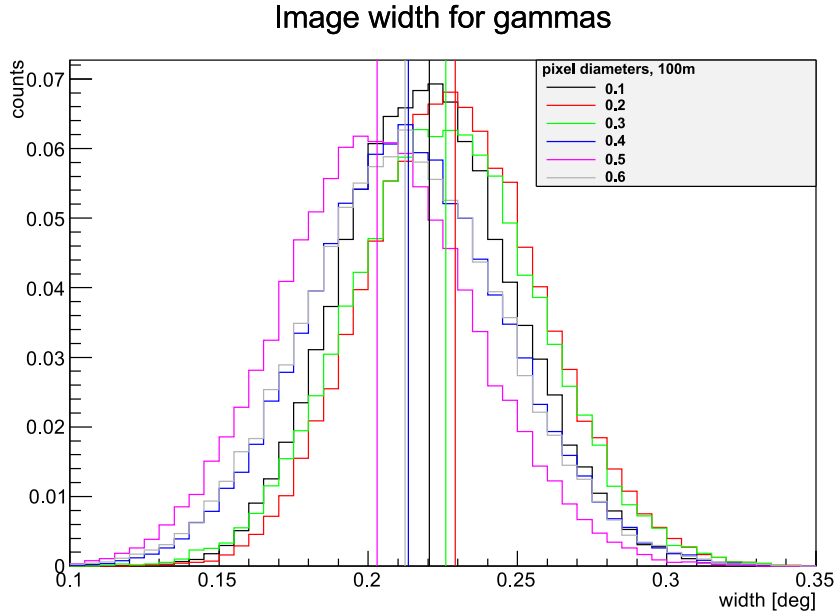


Figure 5.5: Analytical image widths for gamma showers of 100 TeV for pixel sizes from 0.1° to 0.6° for a core distance of 100 m, normalised.

the tailcut varies a little with the pixel positions. The spread of the average image widths between 0.2° and 0.23° is a result of this small variation, the overall image width is almost independent of the pixel size even for pixels with three times the extension of the image. To get a more reliable result, this part of the study needs to be repeated with a randomisation of the actual 2D core position, not just the core distance.

Even though the 3D model does not resolve the inner structure of proton showers, it is still accurate enough to study the effects of undersampling. The image width distribution of the proton showers is shown in figure 5.6. The distribution has its average at a higher value and is wider than the gamma distribution since the assumed 3D-width is larger. The asymmetry of the distribution is also a consequence of the shape of the original 3D width distribution of the emitting region (check figure 5.4b). For the proton showers the averages of the image width distributions do not vary much, but show a slight dependence on the pixel size, with larger pixels featuring slightly larger image widths. Since the protons have a greater image width, the relative influence of the image always having the same orientation in the camera can be neglected.

Figure 5.5 and 5.6 show that the Hillas width of the shower images is almost independent of pixel size. The development of the quality factor with

5.2. GENERAL BEHAVIOUR OF IMAGE WIDTH AND QUALITY FACTOR

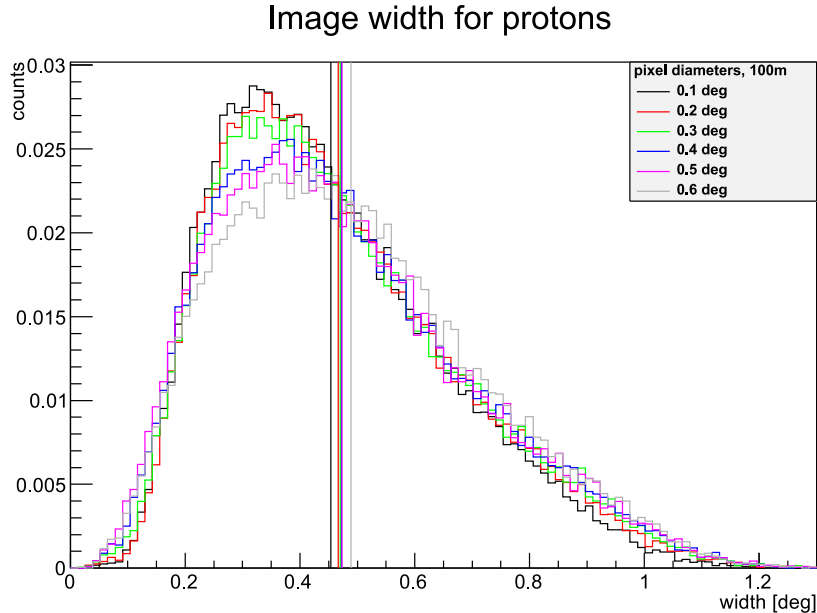


Figure 5.6: Analytical image widths for proton showers of 100 TeV for pixel sizes from 0.1° to 0.6° for a core distance of 100 m, normalised.

pixel size is shown in figure 5.7. As was to be expected, the quality is also almost constant at a value of about 2.3. The best quality factor of 2.35 is reached at pixels of 0.5°. To confirm that the quality factor truly favours larger pixels instead of being independent, the randomisation of the core position mentioned above needs to be implemented. So far, the statement that can be safely made is that the pixel size is not the determining factor for the quality of gamma-hadron separation.

A thorough sampling of a shower is obviously not necessary for gamma hadron separation, especially in a system such as TAIGA. The gamma showers are undersampled, as their images are and stay narrow, with the proton showers having enough image width to discern them from the gamma showers even though their inner structure is neglected.

Strong undersampling can impede the classical monoscopic Hillas analysis, as especially for the thin gamma shower images the orientation of the main image axis can “snap” to certain angles relative to the pixel layout, as the spread of the average image widths in figure 5.5 illustrates. For stereoscopic systems, this snapping is removed by the reconstruction from more than one image. The TAIGA setup with its monoscopic IACTs can compensate this behaviour as well, since the core impact position and therefore the nominal image axis orientation is known from the sampling array.

5.2. GENERAL BEHAVIOUR OF IMAGE WIDTH AND QUALITY FACTOR

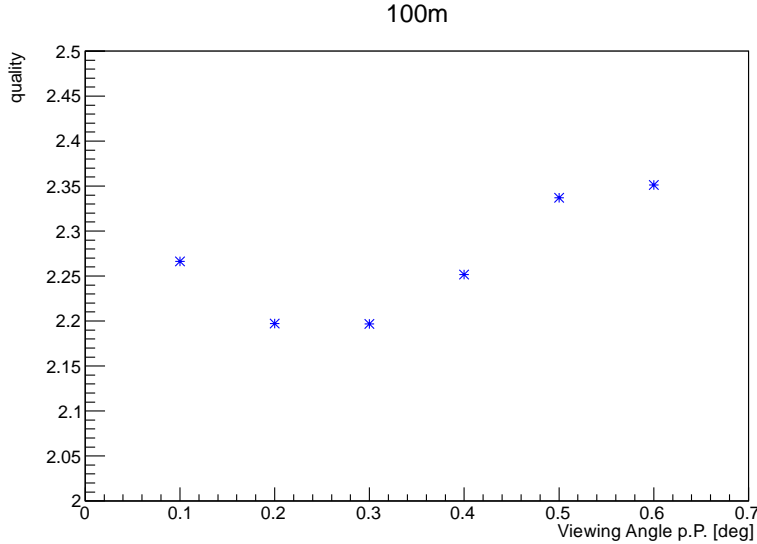


Figure 5.7: Maximum reachable quality factor for showers with 100 TeV at a core distance of 100 m, for pixels from 0.1° to 0.6° . The quality factor is almost constant, but favours larger pixel sizes.

Another point of caution of large pixels is the amount of NSB noise. The Cherenkov light produced by showers of low energy is relatively faint. In such a case, large pixels would collect too much background noise. For showers of high energy however, the Cherenkov flashes that the IACT needs to detect are bright. IACTs optimised for high energies can therefore be equipped with large pixels, because while the lower energy threshold may rise, the showers in the energy range of interest still have a more than sufficient signal to noise ratio.

These two factors allow the camera pixels of IACTs to be far larger than so far common as the reconstruction of impact point and incidence direction can still be performed with sufficient accuracy, and NSB does not pose a problem. Larger pixels reduce the amount of pixels in a camera and therefore the cost of the IACT electronics, which in turn allows to build more IACTs on a given budget. The TAIGA IACT pixels with a diameter of 0.38° are a good choice between resolution and cost, even though it might even be possible to further reduce the amount of pixels per telescope by using larger ones.

5.3. LARGE CORE DISTANCES: THE LIMITATIONS OF THE 3D MODEL

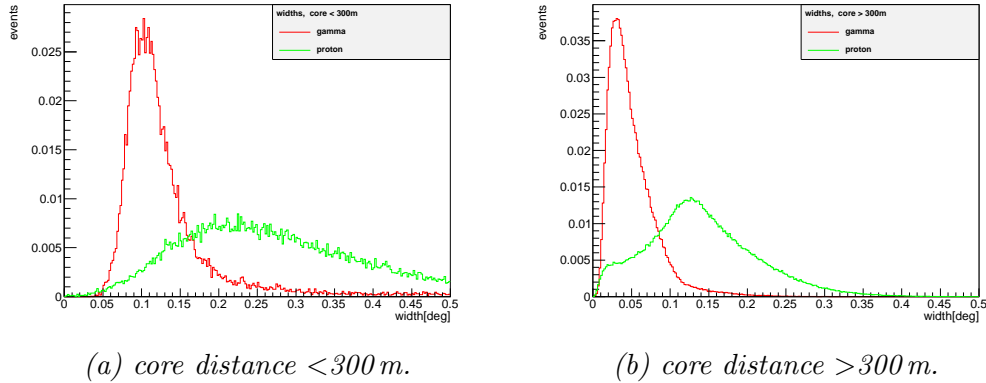


Figure 5.8: Analytic width distribution for gamma (red) and proton showers (green) at different core distances. The distribution for close showers (left) matches the expected shape of the MC distribution as seen in figure 4.23, while the shape for far away showers does not match at all.

5.3 Large core distances: The limitations of the 3D model

The original purpose of the 3D model was to properly reconstruct showers that were detected by the HESS array. As HESS is operating stereoscopically, the focus of the model lies at core distances closer than 150 m.

Using this model to predict possible shower images has shown that apart from the inaccuracy concerning proton showers, the core distance yields the strongest limitation to the usability of this model. Figure 5.8 shows the image width distributions obtained from the methods described above for gamma and proton showers, separated by core distance of less than 300 m (figure 5.8a) and more than 300 m (figure 5.8b).

For close core distances, the shape of the obtained distributions matches the shape expected from the MC simulation. The average image width is a little bit smaller than the `sim_telarray` result (compare figure 4.23, left), but the width of the distributions is similar.

For core distances larger than 300 m as seen in figure 5.8b, the distributions lose their semi-natural shape. Where natural (MC) image width distributions change shape only little with increasing core distance as result of the Tur Tur effect (see Chapter 4.2.3), the analytical distributions become narrower and shift to far smaller means.

A direct comparison between the image widths expected from MC and obtained from the analytical method can be found in figure 5.9 for gamma showers. For small core distances (< 50 m), the analytical model overesti-

5.3. LARGE CORE DISTANCES: THE LIMITATIONS OF THE 3D MODEL

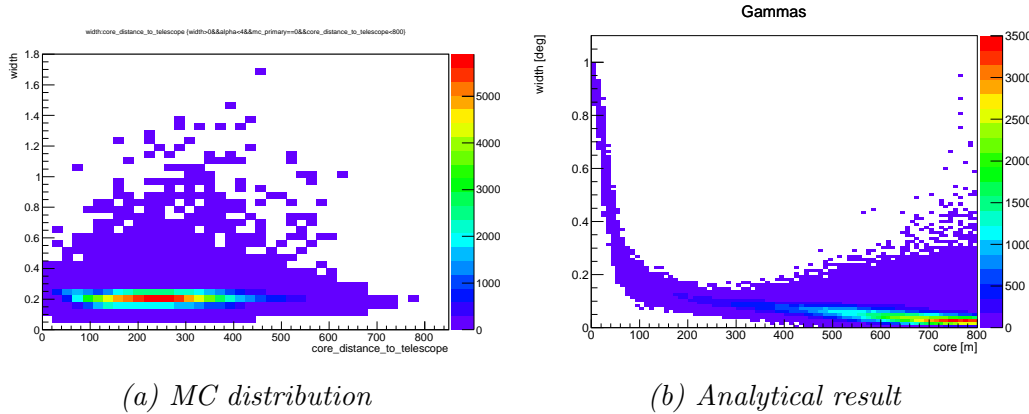


Figure 5.9: Image widths against core distance, from the TAIGA MC study (left) and the analytical solution (right). While the MC showers remain smoothly around 0.2 , the widths by the analytical solution behave vastly different: For the smallest core distances, the width rises up to 1° as a consequence of the simplification of the emission probability function as shown in figure 5.2. The peak at $x = \epsilon/\eta = 1$ in figure 5.2 is neglected, which removes the inner structure of the image and results in a larger image width. The image widths for larger distances become really small, approaching zero, as the Tur Tur effect is neglected as well.

mates the image width as it neglects the strong particle pileup at the center of the shower and simplifies the emission probability function as shown in figure 5.2. The peak at $x = \frac{\epsilon}{\eta} = 1$ is neglected, which removes the inner structure of the image and results in a larger image width. This overestimation however does not have a strong impact on the overall distribution as there are only few showers; the number of showers that arrive at a certain core distance rises with the square of the radius.

The impact is much larger for the severe effect that arises for core distances above 150 m: The image width drops below 0.1° and continues dropping with increasing distance. Due to their large number, these showers have the largest weight in the distribution.

The origin of this narrowing lies in the exclusion of the Tur Tur effect from the 3d model. The emission probability function of the 3D model as shown in figure 5.2 is used for all emitting volume elements independent from their position relative to the shower axis. In real showers, however, the emission angle is in fact not independent from the emitting particles' position relative to the axis.

Figure 5.10 shows the distribution of emission angles obtained from a 100 TeV gamma shower simulated by CORSIKA, for photons detected close to the shower axis (green) and far away (blue). Contrary to the small 3D

5.3. LARGE CORE DISTANCES: THE LIMITATIONS OF THE 3D MODEL

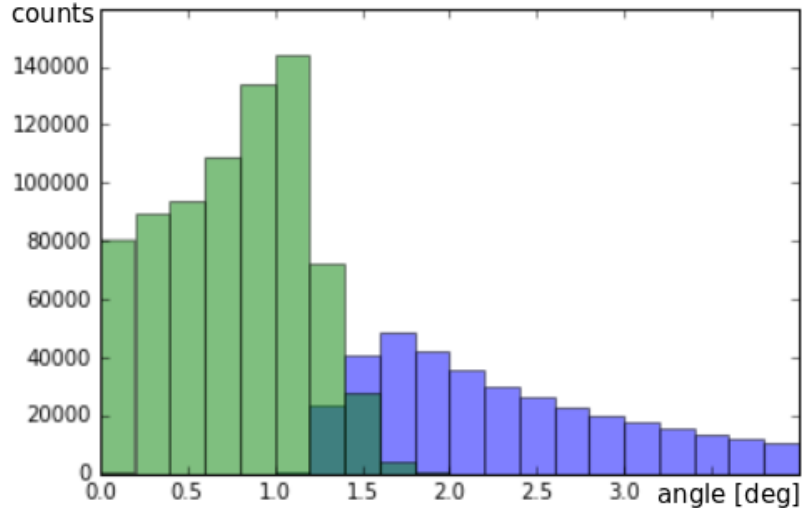


Figure 5.10: Emission angles relative to the shower axis for photons emitted close to the shower axis ($r' < 150$ m, green) and far away ($r' > 150$ m, blue). The distribution for close photons matches the emission probability distribution shown in figure 5.2, as the Cherenkov angle is approximately 1° . The distribution for larger distance from the shower core however does not follow the same correlation. Plot courtesy of D.Horns.

width σ_T of the 3D model, the distinction between near and far has been made at 150 m, which is close to the Molière radius at the shower maximum. A particle cascade’s transversal momentum stems from multiple scattering, and the Molière radius characterises a cylinder of the radius r_M in which 90% of the energy of a particle cascade is deposited in a medium. It depends on critical energy and radiation length of the medium and changes with altitude, with the radius at the shower maximum varying between 110 m - 180 m depending on the height of the shower maximum [18].

In the distribution of figure 5.10, it can be seen that for close photons and an angle of below 1.5° , the shape of the distribution does match the probability function shown in figure 5.2, including the strong spike at the Cherenkov angle that is deliberately disregarded in the 3D approach. Above 1.5° , the distribution does not show the strong tail that the function of the 3D model provides, but rather a cutoff at 1.8° .

This tail on the other hand can be found for the photons emitted at larger distance from the shower axis. Almost no photons are emitted at the Cherenkov angle or less, the photons are distributed over several degrees, which causes the Tur Tur effect: The emission of the outer parts of the shower are stronger under larger observation angles (i.e. core distances), which in

turn makes the shower image wider with increasing core distance.

As a conclusion, assuming the emission probability function to be a merging of these two distributions may be accurate enough for small core distances as the emission angles of the received photons do not exceed 1° , but for larger core distances and therefore larger observation angles the emission probability function of equation 5.2 is inadequate, which in turn leads to the extreme slimming of the shower images shown by the 3D model.

To improve the 3D modelling of the showers, the emission probability function needs to be made dependent on the position of the emitting volume relative to the shower axis. This task however exceeds the scope of this thesis and will be pursued on a later date.

5.4 CMOS Cherenkov detection

The high energy end of the spectrum of cosmic rays and gamma rays remains a mystery to us. We know that the flux goes down harshly and the effective areas needed to observe showers of more than 100 TeV are enormous and impossible to cover with IACTs.

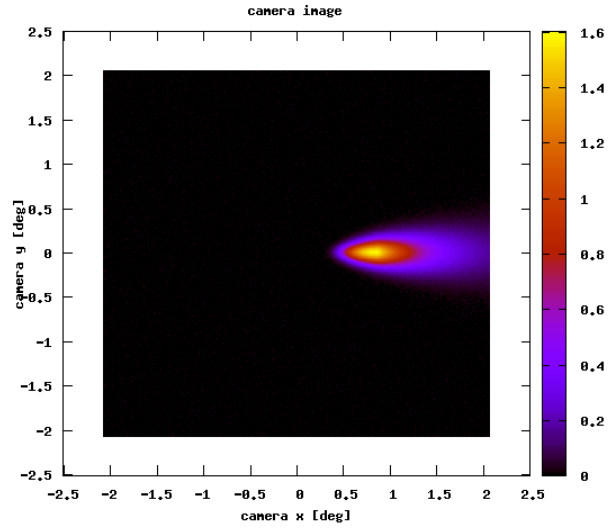
The analytic method was used to determine if the expensive IACTs can theoretically be replaced by far cheaper off-the-shelf CMOS cameras for the highest energies. Standard CMOS cameras operate at 4M pixels, but since the code runs out of memory the size of the camera was reduced to 500x500 pixels, which is enough for the proof of principle.

Due to the limitations of the 3D model described above, the core distance for this study was chosen to be 100 m, where the model is the most accurate, with only the NSB as a noise source.

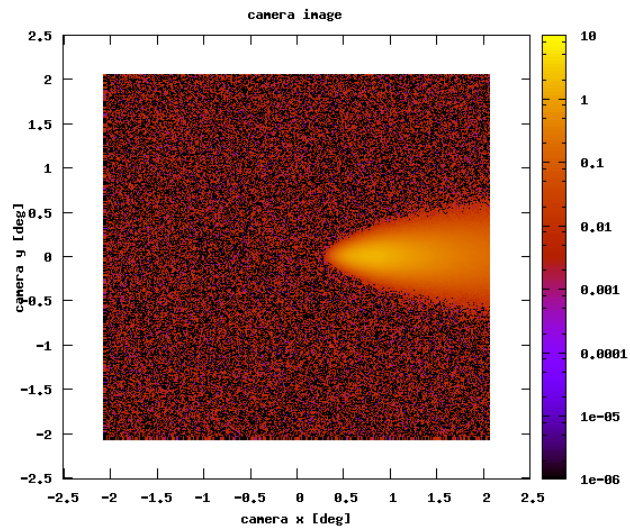
Figure 5.11 shows the image of a 5 PeV shower as would be seen by a telescope with a collection area of 0.008 m^2 , which corresponds to a commercially available 50 mm CMOS camera. The resulting image contains many pixels with one or more photons arriving, making image reconstruction fully possible.

Even with regards to detection efficiency, the 3D model reaches the conclusion that a detection of 5 PeV showers with a CMOS camera should be possible. Further study of this principle as well as the first experimental setups and measurements can be found in the PhD thesis of Rayk Nachtigall [59].

5.4. CMOS CHERENKOV DETECTION



(a) linear colour scale



(b) logarithmic colour scale

Figure 5.11: Exemplary image of a 5 PeV shower seen with a CMOS of 50 mm aperture in units of arriving photons with different colour scales.

Chapter 6

Conclusion and Outlook

In this thesis, the properties of the TAIGA IACTs were studied with two different approaches. The Monte Carlo method was chosen to assess the performance of the intended IACT design and the combination of IACTs with the HiSCORE timing array. An analytical approach was taken to analyse the more theoretical questions like optimisation of pixel size and observation of PeV showers with CMOS cameras.

6.1 MC simulation

Summary: The point spread function of the TAIGA IACTs has been studied by MC ray tracing and found to be smaller than an IACT pixel for all possible off-axis angles. The influence of the ratio between mirror tile radius and main dish radius shows that large mirror tiles are favourable for a large FoV telescope as the PSF for larger off-axis angles is smaller than for small mirror tiles.

Also, the properties of the mirror facets of the first telescope were determined by measurement, with single-mirror PSF and focal length found to be as specified for the telescope.

The average mirror misalignment angle of the TAIGA setup was estimated to be of the order of 0.02° due to construction and calibration methods, the MC ray tracing study showed that for all average misalignment angles below 0.05° , the overall PSF stays smaller than the size of a TAIGA pixel for off-axis angles up to 5° .

The effective areas of a single TAIGA IACT and of a nine station array has been determined for both gamma- and proton-induced air showers. The TAIGA IACTs have been deemed suitable for the application with the HiSCORE array and shows an optimal usage of the 600 m x 600 m telescope

6.1. MC SIMULATION

spacing.

The differences in simulated event count for different energy bins were normalised out and fits were performed to determine the dependency of the energy on the image size for different core distances, which then were used for any further analyses.

The main goal of the MC studies was to determine the gamma hadron separation power of the combined TAIGA system, where the HiSCORE stations provide core position and incidence angle and the nature of the primary is determined from the width of the resulting shower image. As a full combined simulation was not possible in the scope of this thesis, the IACT simulation was used without any direct HiSCORE information, but with the MC-known core position randomised with the known energy-dependent core resolution of the HiSCORE array to emulate a combination. A cut on the raw (unscaled) image width of the data sample yields a separation quality factor (defined in equation 4.9) of 1.3, while a preliminary factor of 1.95 is reached by removal of incomplete images.

Further improvement to the separation factor is made by scaling the shower widths to the expectancy values of gamma showers of the same image size. For this purpose, a lookup table was computed (figure 4.24). Scaling the previous image width distribution results in an increase of the quality factor to 2.7, which is significantly better than the quality factor of the HiSCORE array alone, which only reaches 2 at an energy of about 100 TeV.

The maximum quality factors were studied for their energy and core distance dependence. The conclusion was that the optimum cut distance lies at about 250 m. The all-energy hybrid scaled width distribution for core distances below 250 m reaches a quality factor of 4.6.

The reason behind the mediocre separation quality at large core distances was found to be the Tur Tur effect. The average emission distance of the Cherenkov photons increases the further the observer is from the shower core, which makes the shower appear wider the farther the observer is away. This effect is almost cancelled out by the geometric shrinking of the viewing angle, so that the image width expectancy value of the gamma showers stays almost constant with core distance, which in turn renders the scaling ineffective.

The magnetic field of Earth was also found to have an impact of about 10% on the image width, though no deeper study was conducted there.

As a last step with the MC simulation, the attempt of creating a time-efficient study of pixel size on image width has been made. The idea was to simulate shower images with a ultra fine camera and the summation of the amplitude of adjacent pixels to create larger macropixels without re-running the MC simulation. This method has proven itself to be deficient however, as the rejection of incomplete pixels lead to a truncation of the shower image

at the edge, which distorted the image width.

Outlook: The TAIGA IACT design is well-suited for the intended purpose and can be kept as-is for the observations. The simulations however need to be further refined, as by now, the simulated parameters differ slightly from the final design in respects of exact pixel layout and number of pixels, trigger drawers in the camera, number and alignment of mirrors and telescope positions. As MC simulations are the only way of obtaining the lookup table for scaling the true detected showers, the MC simulations need to be repeated with great attention to detail. Also, so far no true hybrid simulation has been performed yet, but the respective code is well under way.

The origin and implications of the Tur Tur effect are being studied more thoroughly, with the deepened understanding of the shower mechanics possibly opening the way to improved reconstruction of far away showers.

Also, the scaling of showers to their gamma expectancy value can be improved by introducing a factor dependent on the cosine of the angle between north direction, telescope position and shower impact position to take the impact of Earth's magnetic field on the shower width into account and possibly improve the gamma hadron separation even further.

As the summation of pixels did not prove to be constructive, the only option to truly assess the effect of pixel size on gamma hadron separation is to perform a separate, full MC simulation for each pixel size of interest.

6.2 Analytical Study

Summary: To simplify the study of pixel size, a semi-analytical model was used to generate camera images by calculating the expected number of arriving photons at the respective pixel, based on a formula by Lemoine-Gourmard et al [56]. In this model, a gamma shower is simplified down to a 3D gaussian ellipsoid that emits Cherenkov light with the angular distribution found in figure 5.2. Their formula was implemented into a code, which combines the deterministic information from the formula with shower-to-shower fluctuations of shower depth and ellipsoid widths and NSB noise, with different base and variation values for gamma showers and proton showers.

This code was then used to generate gamma and proton showers as seen with different pixel sizes and determining the resulting image width analogous to the MC-generated images. The pixel size range of 0.1° to 0.6° was studied for showers of 100 TeV and 100 m core distance. The image width was found to be varying only little between different pixel sizes. The resulting quality factor was therefore almost constant between 2.2 to 2.3, with a

6.2. ANALYTICAL STUDY

slight favouring of larger pixel sizes. This brings the conclusion that a fine sampling of gamma showers is not necessary to distinguish them from proton showers, and that the TAIGA design with its comparably large pixel size of 0.38° is sensible.

The analytical model has its limitations however. At small core distances, the image width is largely overestimated as the emission probability function neglects the probability spike at the Cherenkov angle that a natural shower shows. At large core distances, the disregarding of the Tur Tur effect leads to a severe underestimation of the image width, so that the model is only adequate for core distances of less than 300 m.

Lastly, the analytic model was used to prove that, in principle, a gamma shower of 5 PeV could be seen by a standard 50 mm aperture CMOS camera.

Outlook: The fact that the pixel size is not decisive in the question of gamma hadron separation allows for new possibilities in the observation of UHE showers with IACTs. So far, the IACT collaborations typically use finely pixelated cameras to reduce the amount of NSB noise accumulated by the PMTs. IACTs with large pixels have a higher energy threshold as the shower signal to NSB noise ratio is less ideal for showers of lower energy, but this is inconsequential for IACTs specialised for UHE observation, as they are meant to observe very bright showers. Therefore the pixels can be chosen large, which increases the lower energy threshold, but drastically reduces the cost of the telescopes. As the analytical study showed that a fine sampling of the gamma shower is not necessary, it might be efficient to incorporate this fact into the design of future UHE IACTs.

The model itself still needs some refinement. The angular emission probability distribution needs to be made dependent on the position of the emitting volume element relative to the shower axis, as shown from the distribution obtained from a shower generated with CORSIKA, to incorporate both the emission spike at the Cherenkov angle for close core distances and the Tur Tur effect as seen from far away.

The observation of showers with a CMOS camera is under study, with a first experimental setup and measurements described in the PhD thesis of Rayk Nachtigall [59].

Appendix A

Measured mirror parameters

mirror	R_{nom}	R_{meas}	FWHM	r_{86}
3	9.45	9.45	0.29	1.13
4	9.45	9.46	0.575	2.545
5	9.5	9.52	0.325	1.775
6	9.45	9.46	0.275	1.875
7	9.45	9.45	0.425	1.925
8	9.40	9.46	0.275	1.425
9	9.45	9.47	0.225	1.425
10	9.45	9.46	0.525	3.875
11	9.4	9.43	0.225	0.725
12	9.45	9.52	0.275	1.025
13	9.4	9.48	0.325	0.475
14			broken	
15	9.5	9.48	0.225	1.075
16	9.47	9.44	0.225	2.075
17	9.40	9.42	0.225	1.025
18	9.45	9.44	0.275	1.025
19	9.45	9.44	0.225	1.475
20	9.4	9.48	0.225	1.475
21	9.4	9.45	0.275	0.625
22	9.45	9.48	0.325	1.825
23	9.4	9.39	0.225	0.875
24	9.55	9.62	0.175	1.525
25	9.45	9.5	0.275	1.175
26	9.48	9.50	0.225	1.425
27	9.45	9.43	0.325	0.825
28	9.45	9.50	0.275	1.325
29	9.45	9.47	0.375	2.325
30	9.4	9.46	0.375	1.825

Acknowledgements

First of all, I want to thank my supervisor Prof. Dieter Horns and our post-doc and project coordinator Martin Tluczykont for their unending patience, helpfulness and proofreading. Also large thanks for Rayk Nachtigall and the rest of our group, with all their tips and tricks and little hints that make day-to-day office life so much easier.

I want to thank my longtime sweetheart and fresh husband Alexander, for without him I would have given up on this thesis a long time ago. Same goes for my best friend Ricarda Laasch, her husband Sebastian Aderholt, my own family and all those other crazy people I am lucky to call my friends. Your support was, is, and always will be invaluable.

Special thanks go to my buddy Dr. Sven Ackermann, who also proofread this thesis for me despite him being a specialist not for cosmic, but man-made accelerators.

Finally, I also thank all those people who enabled me to write my thesis without ever knowing I exist. Therefore, I extend my thanks to Konrad Bernlöhr, who wrote the fantastic piece of code that is `sim_telarray`, the makers of Linux and LaTeX, every musician who plays metal, and the person who invented the energy drink. All these things were mandatory for the completion of this work.

List of abbreviations

α	:	Tessellation ratio, $\alpha = r_{\text{mirror tile}} / R_{\text{mirror dish}}$
BS	:	Bremsstrahlung
CMB	:	Cosmic microwave background
CoG	:	Center of gravity
CR	:	Cosmic rays
EAS	:	Extensive air shower
EM	:	Electromagnetic (showers)
FoV	:	Field of view
HiSCORE	:	High Surface Cosmic Origin Explorer
HSCW	:	Hybrid scaled width
IACT	:	Imaging Air Cherenkov Telescope
LDF	:	Light density function
MC	:	Monte Carlo method
NSB	:	Night sky background
PMT	:	Photomultiplier tube
PSF	:	Point spread function
Q	:	Quality factor, a measure of the background rejection power of a cut
TAIGA	:	Tunka Advanced Instrument for Gamma-ray and Cosmic ray Astrophysics
UHE	:	Ultra-high energy, $E > 10^{18}$ eV

List of Figures

2.1	All-particle CR spectrum	7
2.2	Shower parameters	11
2.3	Development of air showers	12
3.1	HiSCORE data processing	16
3.2	principle of a shower plane fit	18
3.3	TAIGA pixels and camera (photo)	21
3.4	Camera front view	22
4.1	Combination concept	26
4.2	Ray diagram: Spherical vs Davies-Cotton	28
4.3	Ray diagram with labels	29
4.4	TAIGA PSF spots	30
4.5	Comparison TAGIA-PSF vs. analytical prediction	31
4.6	Spot comparison: different tessellation ratio	32
4.7	Mirror test setup for the 2f-method, schematic view.	33
4.8	Mirror measurement example image	34
4.9	Cumulative radial profile of the PSF of a single mirror facet	35
4.10	Measured PSFs and focal lengths for the first 28 TAIGA mirrors	36
4.11	Example TAIGA PSF spots /w mirror misalignments	38
4.12	Deformation of the telescope under its weight	39
4.13	Spot size change with misalignments	40
4.14	Spot profiles for mirror misalignments	41
4.15	Effective area vs. primary energy for TAIGA	42
4.16	Normalized shower statistics	44
4.17	Fit: Image size vs. primary energy for different core distances	47
4.18	Schematic of imaging with a cherenkov telescope	48
4.19	Tailcut example image	50
4.20	The Hillas [46] parameters as found in an IACT camera image.	51
4.21	Examples for hadronic and EM shower images	52
4.22	Unscaled raw image width distribution for TAIGA	53

LIST OF FIGURES

4.23	Unscaled image width distribution for TAIGA, including cuts	56
4.24	TAIGA IACT width lookup table	57
4.25	Lookup table profiles along 100 m and $\log(\text{size})=2.5$	57
4.26	Scaled width distribution for TAIGA for 300 m cut	59
4.27	Q vs. core and energy	60
4.28	integrated quality factor for energies	61
4.29	Scaled width distribution for TAIGA	62
4.30	Photon emission height vs. detection core distance	63
4.31	Photon emission off-axis distance vs. detection core distance	65
4.32	Image widths by viewing direction	66
4.33	Pixel summation concept	69
4.34	Pixel combination example images	70
4.35	Pixel combination image widths with TAIGA	71
4.36	Pixel combination image widths for larger pixels	72
4.37	Pixel combination alpha angles	73
5.1	Parameters used in the analytic calculation	76
5.2	Cherenkov photon emission distribution per solid angle	77
5.3	Analytical example image for 50 TeV	79
5.4	Image widths by viewing direction	80
5.5	Analytical image widths, gammas	81
5.6	Analytical image widths, protons	82
5.7	Quality vs. pixel size	83
5.8	Analytical image widths, divided at 300 m	84
5.9	Image widths vs. core distance, MC and analytical	85
5.10	Emission angles by CORSIKA	86
5.11	CMOS example images	88

List of Tables

3.1	Table of telescope parameters as used in the simulation.	20
4.1	Datasets and normalisation factors	45
4.2	Table of cuts on MC data	55

LIST OF TABLES

Bibliography

- [1] M. Ende. *Jim Knopf und Lukas der Lokomotivführer*. Thienemann, Stuttgart, since 1960.
- [2] V. Hess. Observation of Penetrating Radiation of seven Balloon Flights. *Physikalische Zeitschrift*, 13:1084, 1912.
- [3] R. A. Millikan and G. H. Cameron. The origin of the cosmic rays. *Phys. Rev.*, 32:533–557, Oct 1928.
- [4] P. Dirac. Quantised singularities in the electromagnetic field,. *Proceedings of the Royal Society of London A: Mathematical, Physical and Engineering Sciences*, 133(821):60–72, 1931.
- [5] P. Auger, P. Ehrenfest, R. Maze, J. Daudin, and R. A. Fréon. Extensive Cosmic-Ray Showers. *Reviews of Modern Physics*, 11:288–291, July 1939.
- [6] A. M. Hillas. Cosmic Rays: Recent Progress and some Current Questions. *ArXiv Astrophysics e-prints*, July 2006.
- [7] E. Fermi. On the Origin of the Cosmic Radiation. *Physical Review*, 75:1169–1174, April 1949.
- [8] R. Aloisio, V. Berezhinsky, and A. Gazizov. Transition from galactic to extragalactic cosmic rays. *Astroparticle Physics*, 39-40(Supplement C):129 – 143, 2012. Cosmic Rays Topical Issue.
- [9] A. M. Hillas. TOPICAL REVIEW: Can diffusive shock acceleration in supernova remnants account for high-energy galactic cosmic rays? *Journal of Physics G Nuclear Physics*, 31:R95–R131, May 2005.
- [10] T. Wibig and A. W. Wolfendale. At what particle energy do extragalactic cosmic rays start to predominate? *ArXiv Astrophysics e-prints*, October 2004.

BIBLIOGRAPHY

- [11] K. Greisen. End to the Cosmic-Ray Spectrum? *Physical Review Letters*, 16:748–750, April 1966.
- [12] G. T. Zatsepin and V. A. Kuz'min. Upper Limit of the Spectrum of Cosmic Rays. *Soviet Journal of Experimental and Theoretical Physics Letters*, 4:78, August 1966.
- [13] M. J. Rees. Studies in radio source structure-III. Inverse Compton radiation from radio sources. *MNRAS*, 137:429, 1967.
- [14] G. Fossati, A. Celotti, G. Ghisellini, and L. Maraschi. Average Spectral Energy Distributions of Blazars from Radio to Gamma-Rays. In M. Ostrowski, M. Sikora, G. Madejski, and M. Begelman, editors, *Relativistic Jets in AGNs*, pages 245–248, 1997.
- [15] J. A. Hinton and W. Hofmann. Teraelectronvolt Astronomy. *ARA&A*, 47:523–565, September 2009.
- [16] S. Gabici and F. A. Aharonian. Searching for Galactic Cosmic-Ray Pevatrons with Multi-TeV Gamma Rays and Neutrinos. *ApJ*, 665:L131–L134, August 2007.
- [17] W. B. Atwood, A. A. Abdo, M. Ackermann, W. Althouse, B. Anderson, M. Axelsson, L. Baldini, J. Ballet, D. L. Band, G. Barbiellini, and et al. The Large Area Telescope on the Fermi Gamma-Ray Space Telescope Mission. *ApJ*, 697:1071–1102, June 2009.
- [18] P. Grieder. *Extensive Air Showers*, volume 1. Springer-Verlag, Berlin-Heidelberg, 2010.
- [19] J. Abraham, P. Abreu, M. Aglietta, E. J. Ahn, D. Allard, I. Allekotte, J. Allen, J. Alvarez-Muñiz, M. Ambrosio, L. Anchordoqui, and et al. Measurement of the Depth of Maximum of Extensive Air Showers above 10^{18} eV. *Physical Review Letters*, 104(9):091101, March 2010.
- [20] P. A. Čerenkov. Visible Radiation Produced by Electrons Moving in a Medium with Velocities Exceeding that of Light. *Physical Review*, 52:378–379, August 1937.
- [21] M. de Naurois and D. Mazin. Ground-based detectors in very-high-energy gamma-ray astronomy. *Comptes Rendus Physique*, 16:610–627, August 2015.
- [22] J. Holder. Atmospheric Cherenkov Gamma-ray Telescopes. *ArXiv e-prints*, October 2015.

-
- [23] G. Sinnis, A. Smith, and J. E. McEnery. Hawc: A next generation all-sky vhe gamma-ray telescope. *American Institute of Physics*, 745:234, 2004.
- [24] W. D. Apel, J. C. Arteaga, A. F. Badea, K. Bekk, M. Bertaina, J. Blümer, H. Bozdog, I. M. Brancus, P. Buchholz, E. Cantoni, A. Chiavassa, F. Cossavella, K. Daumiller, V. de Souza, F. Di Pierro, P. Doll, R. Engel, J. Engler, M. Finger, D. Fuhrmann, P. L. Ghia, H. J. Gils, R. Glasstetter, C. Grupen, A. Haungs, D. Heck, J. R. Hörandel, T. Huege, P. G. Isar, K.-H. Kampert, D. Kang, D. Kickelbick, H. O. Klages, K. Link, P. Luczak, M. Ludwig, H. J. Mathes, H. J. Mayer, M. Melissas, J. Milke, B. Mitrica, C. Morello, G. Navarra, S. Nehls, J. Oehlschläger, S. Ostapchenko, S. Over, N. Palmieri, M. Petcu, T. Pierog, H. Rebel, M. Roth, H. Schieler, F. Schröder, O. Sima, M. Stümpert, G. Toma, G. C. Trinchero, H. Ulrich, A. Weindl, J. Wochele, M. Wommer, and J. Zabierowski. The KASCADE-Grande experiment. *Nuclear Instruments and Methods in Physics Research A*, 620:202–216, August 2010.
- [25] D. et al. Kostunin. Tunka-Rex: Status and results of the first measurements. *Nuclear Instruments and Methods in Physics Research A*, 742:89–94, April 2014.
- [26] Pierre Auger Collaboration. The Pierre Auger Cosmic Ray Observatory. *Nuclear Instruments and Methods in Physics Research A*, 798:172–213, October 2015.
- [27] A. Karle, M. Merck, and Plaga et al. Design and performance of the angle integrating Čerenkov array AIROBICC. *Astroparticle Physics*, 3:321–347, August 1995.
- [28] S. F. Berezhnev, D. Besson, N. M. Budnev, A. Chiavassa, O. A. Chvalaev, and O. A. et al. Gress. The Tunka-133 EAS Cherenkov light array: Status of 2011. *Nuclear Instruments and Methods in Physics Research A*, 692:98–105, November 2012.
- [29] M Tluczykont et al. Towards gamma-ray astronomy with timing arrays. *Journal of Physics: Conference Series*, 632(1):012042, 2015.
- [30] A. Daum and G. et al. Hermann. First results on the performance of the HEGRA IACT array. *Astroparticle Physics*, 8:1–11, December 1997.
- [31] J. A. Hinton and the HESS Collaboration. The status of the HESS project. *New A Rev.*, 48:331–337, April 2004.

BIBLIOGRAPHY

- [32] N. Budnev et al. The TAIGA experiment: from cosmic ray to gamma-ray astronomy in the Tunka valley. *J. Phys. Conf. Ser.*, 718(5):052006, 2016.
- [33] M. Tluczykont, D. Hampf, D. Horns, D. Spitschan, L. Kuzmichev, V. Prosin, C. Spiering, and R. Wischnewski. The HiSCORE concept for gamma-ray and cosmic-ray astrophysics beyond 10 TeV. *Astroparticle Physics*, 56:42–53, April 2014.
- [34] S. Ritt, R. Dinapoli, and U. Hartmann. Application of the DRS chip for fast waveform digitizing. *Nuclear Instruments and Methods in Physics Research A*, 623:486–488, November 2010.
- [35] O. Gress, I. Astapov, N. Budnev, P. Bezyazeev, A. Bogdanov, V. Boreyko, M. Brückner, A. Chiavassa, O. Chvalaev, A. Dyachok, T. Gress, S. Epimakhov, E. Fedoseev, A. Gafarov, N. Gorbunov, V. Grebenyuk, A. Grinuk, O. Grishin, D. Horns, A. Ivanova, A. Kalinin, N. Karpov, N. Kalmykov, Y. Kazarina, N. Kirichkov, S. Kiryuhin, R. Kokoulin, K. Komponiest, E. Korosteleva, V. Kozhin, M. Kunnas, L. Kuzmichev, V. Lenok, B. Lubsandorzhev, N. Lubsandorzhev, R. Mirgazov, R. Mirzoyan, R. Monkhoev, R. Nachtigall, A. Pakhorukov, M. Panasyuk, L. Pankov, A. Petrukhin, V. Platonov, V. Poleschuk, E. Popova, A. Porelli, V. Prosin, G. Rubtsov, A. Pushnin, V. Samoliga, A. Saunkin, Y. Semeney, B. Shaibonov(ju), A. Silaev, A. Silaev(ju), A. Skurikhin, V. Slucka, C. Spiering, L. Sveshnikova, V. Tabolenko, B. Tarashchansky, A. Tkachenko, L. Tkachev, M. Tluczykont, D. Voronin, R. Wischnewski, A. Zagorodnikov, V. Zurbanov, and I. Yashin. The wide-aperture gamma-ray telescope TAIGA-HiSCORE in the Tunka Valley: Design, composition and commissioning. *Nuclear Instruments and Methods in Physics Research A*, 845:367–372, February 2017.
- [36] Maike Kunnas. Bau eines triggersystems für den hiscore-detektor, 2012. Diploma Thesis.
- [37] D. Hampf. *Study of a wide-angle Cherenkov detector for ultra high energy gamma-ray astronomy and time gradient event reconstruction for the H.E.S.S. experiment*. PhD thesis, University of Hamburg, 2012.
- [38] D. Hampf, M. Tluczykont, and D. Horns. Event reconstruction techniques for the wide-angle air Cherenkov detector HiSCORE. *Nuclear Instruments and Methods in Physics Research A*, 712:137–146, June 2013.

-
- [39] J. M. Davies and E. S. Cotton. Design of the quartermaster solar furnace. *Solar Energy*, 1:16–22, April 1957.
- [40] Xp1911 datasheet. retrieved from <https://my.et-enterprises.com/pdf/XP1911.pdf> on Dec 9th, 2016.
- [41] the ZEUS collaboration. Zeus blue book. unpublished, available at <http://www-zeus.desy.de/bluebook/bluebook.html>.
- [42] D. Heck, G. Schatz, T. Thouw, J. Knapp, and J. N. Capdevielle. CORSIKA: A Monte Carlo code to simulate extensive air showers. 1998.
- [43] N. N. Kalmykov, S. S. Ostapchenko, and A. I. Pavlov. Quark-Gluon String Model and EAS Simulation Problems at Ultra-High Energies. *Nucl. Phys. Proc. Suppl.*, 52:17–28, 1997.
- [44] H. Fesefeldt. The simulation of hadronic showers: Physics and applications (rwth, aachen). *85/02 PITHA*, 1985.
- [45] D. Heck and T. Pierog. *Extensive Air Shower Simulation with CORSIKA: A User's Guide*, 2011. retrieved from <https://is.muni.cz/el/1431/jaro2013/F9145/um/40140265/CORSIKA.GUIDE69xx.pdf>.
- [46] A. M. Hillas. Cerenkov light images of EAS produced by primary gamma. *International Cosmic Ray Conference*, 3, August 1985.
- [47] H. Kawai, S. Yoshida, H. Yoshii, K. Tanaka, F. Cohen, M. Fukushima, N. Hayashida, K. Hiyama, D. Ikeda, E. Kido, Y. Kondo, T. Nonaka, M. Ohnishi, H. Ohoka, S. Ozawa, H. Sagawa, N. Sakurai, T. Shibata, H. Shimodaira, M. Takeda, A. Taketa, M. Takita, H. Tokuno, R. Torii, S. Udo, Y. Yamakawa, H. Fujii, T. Matsuda, M. Tanaka, H. Yamaoka, K. Hibino, T. Benno, K. Doura, M. Chikawa, T. Nakamura, M. Teshima, K. Kadota, Y. Uchihori, K. Hayashi, Y. Hayashi, S. Kawakami, T. Matsuyama, M. Minamino, S. Ogió, A. Ohshima, T. Okuda, N. Shimizu, H. Tanaka, D. R. Bergman, G. Hughes, S. Stratton, G. B. Thomson, A. Endo, N. Inoue, S. Kawana, Y. Wada, K. Kasahara, R. Azuma, T. Iguchi, F. Kakimoto, S. Machida, K. Misumi, Y. Murano, Y. Tameda, Y. Tsunesada, J. Chiba, K. Miyata, T. Abu-Zayyad, J. W. Belz, R. Cady, Z. Cao, P. Huentemeyer, C. C. H. Jui, K. Martens, J. N. Matthews, M. Mostofa, J. D. Smith, P. Sokolsky, R. W. Springer, J. R. Thomas, S. B. Thomas, L. R. Wiencke, T. Doyle, M. J. Taylor, V. B. Wickwar, T. D. Wilkerson, K. Hashimoto, K. Honda, K. Ikuta,

BIBLIOGRAPHY

- T. Ishii, T. Kanbe, and T. Tomida. Telescope Array Experiment. *Nuclear Physics B Proceedings Supplements*, 175:221–226, January 2008.
- [48] T. Antoni and KASCADE Collaboration. Search for Cosmic-Ray Point Sources with KASCADE. *ApJ*, 608:865–871, June 2004.
- [49] G. Di Sciascio and on behalf of the LHAASO Collaboration. The LHAASO experiment: from Gamma-Ray Astronomy to Cosmic Rays. *ArXiv e-prints*, February 2016.
- [50] M. Actis, G. Agnetta, A. Aharonian, F. and Akhperjanian, J. Aleksić, E. Aliu, D. Allan, I. Allekotte, F. Antico, L. A. Antonelli, P. Antoranz, A. Aravantinos, T. Arlen, H. Arnaldi, S. Artmann, K. Asano, H. Asorey, A. Bähr, J. and Bais, C. Baixeras, S. Bajtlik, D. Balis, A. Bamba, C. Barbier, M. Barceló, A. Barnacka, J. Barnstedt, U. Barres de Almeida, J. A. Barrio, S. Basso, D. Bastieri, C. Bauer, J. Becerra, Y. Becherini, K. Bechtol, J. Becker, V. Beckmann, W. Bednarek, B. Behera, M. Beilicke, M. Belluso, M. Benallou, W. Benbow, J. Berdugo, K. Berger, T. Bernardino, K. Bernlöhr, A. Biland, S. Billotta, T. Bird, E. Birsin, E. Bissaldi, S. Blake, O. Blanch, A. A. Bobkov, L. Bogacz, M. Bogdan, C. Boisson, J. Boix, J. Bolmont, G. Bonanno, A. Bonardi, T. Bonev, J. Borkowski, O. Botner, A. Bottani, M. Bourgeat, A. Boutonnet, C. and Bouvier, S. Brau-Nogué, I. Braun, T. Bretz, M. S. Briggs, P. Brun, L. Brunetti, J. H. Buckley, V. Bugaev, R. Bühler, T. Bulik, G. Busetto, S. Buson, K. Byrum, M. Cailles, R. Cameron, R. Canestrari, S. Cantu, E. Carmona, A. Carosi, J. Carr, P. H. Carton, M. Casiraghi, H. Castarede, O. Catalano, S. Cavazzani, S. Cazaux, B. Cerruti, M. Cerruti, P. M. Chadwick, J. Chiang, M. Chikawa, M. Cieřlar, M. Ciesielska, A. Cillis, C. Clerc, P. Colin, J. Colomé, M. Compin, P. Conconi, V. Connaughton, J. Conrad, J. L. Contreras, P. Coppi, M. Corlier, P. Corona, O. Corpace, D. Corti, J. Cortina, H. Costantini, G. Cotter, B. Courty, S. Couturier, S. Covino, J. Croston, G. Cusumano, M. K. Daniel, F. Dazzi, A. de Angelis, E. de Cea del Pozo, E. M. de Gouveia Dal Pino, O. de Jager, I. de la Calle Pérez, G. De La Vega, B. De Lotto, M. de Nauris, E. de Oña Wilhelmi, V. de Souza, B. Decerprit, C. Deil, E. Delagnes, G. Deleglise, C. Delgado, T. Dettlaff, A. Di Paolo, F. Di Pierro, C. Díaz, J. Dick, H. Dickinson, S. W. Digel, D. Dimitrov, G. Dissert, A. Djannati-Ataï, M. Doert, W. Domainko, D. Dorner, M. Doro, J.-L. Dournaux, D. Dravins, L. Drury, F. Dubois, R. Dubois, G. Dubus, C. Dufour, D. Durand, J. Dyks, M. Dyrda, E. Edy, K. Egberts, C. Eleftheriadis, S. Elles, D. Emmanoulopoulos, R. Enomoto, J.-P. Ernenwein, M. Errando, A. Etchegoyen, A. D. Falcone, K. Farakos, C. Farnier,

- S. Federici, F. Feinstein, D. Ferenc, E. Fillin-Martino, D. Fink, C. Finley, J. P. Finley, R. Firpo, D. Florin, C. Föhr, E. Fokitis, Ll. Font, G. Fontaine, A. Fontana, A. Förster, L. Fortson, N. Fouque, C. Fransson, G. W. Fraser, L. Fresnillo, C. Fruck, Y. Fujita, Y. Fukazawa, S. Funk, W. Gäbele, S. Gabici, A. Gadola, N. Galante, Y. Gallant, B. García, R. J. García López, D. Garrido, L. Garrido, D. Gascón, C. Gasq, M. Gaug, J. Gaweda, N. Geffroy, C. Ghag, A. Ghedina, M. Ghigo, E. Gianakaki, S. Giarrusso, G. Giavitto, B. Giebels, E. Giro, P. Giubilato, T. Glanzman, J.-F. Glicenstein, M. Gochna, V. Golev, M. Gómez Berisso, A. González, F. González, F. Grañena, R. Graciani, J. Granot, R. Gredig, A. Green, T. Greenshaw, O. Grimm, J. Grube, M. Grudzińska, J. Grygorczuk, V. Guarino, L. Guglielmi, F. Guilloux, S. Gunji, G. Gyuk, D. Hadasch, D. Haefner, R. Hagiwara, J. Hahn, S. Hallgren, A. and Hara, M. J. Hardcastle, T. Hassan, T. Haubold, M. Hauser, M. Hayashida, R. Heller, G. Henri, G. Hermann, A. Herrero, J. A. Hinton, D. Hoffmann, W. Hofmann, P. Hofverberg, D. Horns, D. Hrupec, H. Huan, B. Huber, J.-M. Huet, G. Hughes, K. Hultquist, T. B. Humensky, J.-F. Huppert, A. Ibarra, J. M. Illa, J. Ingjald, Y. Inoue, S. Inoue, K. Ioka, C. Jablonski, A. Jacholkowska, M. Janiak, P. Jean, H. Jensen, T. Jogler, I. Jung, P. Kaaret, S. Kabuki, J. Kakuwa, C. Kalkuhl, R. Kankanyan, M. Kapala, A. Karastergiou, M. Karczewski, S. Karkar, N. Karlsson, J. Kasperek, H. Katagiri, K. Katarzyński, and etal. Design concepts for the cherenkov telescope array cta: an advanced facility for ground-based high-energy gamma-ray astronomy. *Experimental Astronomy*, 32(3):193–316, Dec 2011.
- [51] A. Schliesser and R. Mirzoyan. Wide-field prime-focus imaging atmospheric Cherenkov telescopes: A systematic study. *Astroparticle Physics*, 24:382–390, December 2005.
- [52] *SAOImage DS9 Software, Version 7.3.2.* retrieved from <http://ds9.si.edu/site/Download.html> on may 29th, 2015.
- [53] HEGRA Collaboration and A. Konopelko. Performance of the stereoscopic system of the HEGRA imaging air Čerenkov telescopes: Monte Carlo simulations and observations. *Astroparticle Physics*, 10:275–289, May 1999.
- [54] M. Tluczykont. *Beobachtung und Nachweis von Aktiven Galaktischen Kernen und Suche nach Galaktischen Objekten im TeV-Energiebereich mit den HEGRA-Cherenkov-Teleskopen sowie Modellierung eines Pho-*

BIBLIOGRAPHY

tonenspektrums durch den Zerfall neutraler Pionen aus schockbeschleunigten Hadronen. PhD thesis, University of Hamburg, 2003.

- [55] Myriam Wertz. Masters thesis, est. 2018. unpublished, in preparation.
- [56] M. Lemoine-Goumard, B. Degrange, and M. Tluczykont. Selection and 3D-reconstruction of gamma-ray-induced air showers with a stereoscopic system of atmospheric Cherenkov telescopes. *Astroparticle Physics*, 25:195–211, April 2006.
- [57] A. A. Al-Rubaiee, Gress. O.A., A. A. Kochanov, K. S. Lokhtin, Y. V. Parfenov, and S. I. Sinegovsky. Parametrization for Cherenkov light lateral distribution function in Extensive Air Showers. *International Cosmic Ray Conference*, 6:249, 2005.
- [58] U.s. standard atmosphere, 1976. retrieved from <https://ntrs.nasa.gov/archive/nasa/casi.ntrs.nasa.gov/19770009539.pdf>.
- [59] Rayk Nachtigall. *PhD thesis.* PhD thesis, University of Hamburg, est. 2018. unpublished, in preparation.

Eidesstattliche Erklärung

Hiermit versichere ich, diese Arbeit eigenständig und nur mit den angegebenen Hilfsmitteln angefertigt zu haben.